FLEXIBLE HOLOGRAPHIC METASURFACES

James Robert Burch

A Thesis Submitted for the Degree of PhD
at the
University of St Andrews

2019

Please use this identifier to cite or link to this item:
http://hdl.handle.net/10023/18336

Flexible Holographic Metasurfaces

James Robert Burch

University
of
St Andrews

This thesis is submitted in partial fulfilment for the degree of
Doctor of Philosophy (PhD)
at the University of St Andrews

May 2019

Abstract

Metasurface holography has attracted much attention in recent years because of its practical applications including anti-counterfeiting, sensing, and lensing. However, most metasurface holograms have been constrained to rigid substrates which limit their out-of-the-lab value. Flexible holographic metasurfaces offer increased post-fabrication tunability as they can be bent or stretched, can be conformed to real-world non-flat surfaces, and are compatible with commercially viable roll-to-roll fabrication methods.

This thesis describes how flexible holographic metasurfaces can be fabricated, their utility, and the novel phenomena that arise from them. In particular, it details a hologram retrieval algorithm for non-flat surface topologies, and how the topography determines the resultant symmetry properties of the holographic image. Furthermore, this thesis outlines a concept for replacing the bulky and complicated optics required for light sheet fluorescent microscopy with a simple holographic metasurface illuminated by a collimated beam.

Two plasmonic meta-atom designs, both operating in reflection, are presented here, one for the visible wavelength range using nanorods and Pancharatnam-Berry phase-shifting, and the other for the millimetre wavelength range using c-rings.

Extending the tools available for holography paves-the-way for advances in this field.

Candidate's declarations

I, James Burch, do hereby certify that this thesis, submitted for the degree of PhD, which is approximately 45,000 words in length, has been written by me, and that it is the record of work carried out by me, or principally by myself in collaboration with others as acknowledged, and that it has not been submitted in any previous application for any degree.

I was admitted as a research student at the University of St Andrews in September 2015.

I received funding from an organisation or institution and have acknowledged the funder(s) in the full text of my thesis.

Date Signature of candidate

Supervisor's declaration

I hereby certify that the candidate has fulfilled the conditions of the Resolution and Regulations appropriate for the degree of PhD in the University of St Andrews and that the candidate is qualified to submit this thesis in application for that degree.

Date Signature of supervisor

Permission for publication

In submitting this thesis to the University of St Andrews we understand that we are giving permission for it to be made available for use in accordance with the regulations of the University Library for the time being in force, subject to any copyright vested in the work not being affected thereby. We also understand, unless exempt by an award of an embargo as requested below, that the title and the abstract will be published, and that a copy of the work may be made and supplied to any bona fide library or research worker, that this thesis will be electronically accessible for personal or research use and that the library has the right to migrate this thesis into new electronic forms as required to ensure continued access to the thesis.

I, James Burch, confirm that my thesis does not contain any third-party material that requires copyright clearance.

The following is an agreed request by candidate and supervisor regarding the publication of this thesis:

Printed copy

No embargo on print copy.

Electronic copy

No embargo on electronic copy.

Date Signature of candidate

Signature of supervisor

Underpinning Research Data or Digital Outputs Candidate's declaration

I, James Burch, understand that by declaring that I have original research data or digital outputs, I should make every effort in meeting the University's and research funders' requirements on the deposit and sharing of research data or research digital outputs.

Date Signature of candidate

Permission for publication of underpinning research data or digital outputs

We understand that for any original research data or digital outputs which are deposited, we are giving permission for them to be made available for use in accordance with the requirements of the University and research funders, for the time being in force.

We also understand that the title and the description will be published, and that the underpinning research data or digital outputs will be electronically accessible for use in accordance with the license specified at the point of deposit, unless exempt by award of an embargo as requested below.

The following is an agreed request by candidate and supervisor regarding the publication of underpinning research data or digital outputs:

No embargo on underpinning research data or digital outputs.

Date Signature of candidate

Signature of supervisor

Acknowledgements

General acknowledgements

During my time as a PhD student, I have been helped and influenced by a great number of people. First, my thanks go to my supervisor Dr Andrea Di Falco, who honed my skills in all areas of research and kept me focussed throughout my PhD. Second, my thanks go to Xianzhong Chen and Dandan Wen from the Experimental Nanophotonics group at Heriot-Watt University because our collaboration guided me towards holography. My thanks also go to the past and present members of the Synthetic Optics group, in particular, to Alasdair Fikouras, Adam Fleming, and Xin Li. We started our PhDs at the same time and will hopefully finish them at the same time too! Next, my thanks go to the cleanroom technicians, in particular to Callum Smith, and the store manager Scott Johnston. Finally, I would like to thank Kris, my parents, and my brothers Andrew and Stuart.

Funding

This work was supported by EPSRC grant number EP/M508214/1; and DASA grant number ACC6004053.

Research Data/Digital Outputs access statement

Research data underpinning this thesis are available at:

https://doi.org/10.17630/a4c273ab-aade-4c7e-a9bf-8c2fdccd2aef,

https://doi.org/10.17630/583a258e-32cb-4a6b-826c-ab7d3b4429e2,

https://doi.org/10.17630/f06f61ab-b0ec-4aae-ba97-5ec49771a578,

https://doi.org/10.17630/162a371-10c7-4512-b678-558951c76e55,

https://doi.org/10.17630/5959f528-af12-427e-b788-b335f8e42fa3

Collaboration Statement

I collaborated on the Conformable Holographic Metasurfaces paper, which is detailed in chapter 4, with Xianzhong Chen and Dandan Wen from the Experimental Nanophotonics group at Heriot-Watt University. In our collaboration, they designed the meta-atom and provided a ’.GDS’ file for writing the holographic metasurface in our electron beam lithography system. They also contributed to writing the paper.

I collaborated on the Flexible Patches for Millimeter Wavelength Holography paper, which is detailed in chapter 6, with Robert Hunter, Duncan Robertson, and Graham Smith of the Millimetre Wave group at the University of St Andrews. This collaboration also included Sebastian Schulz of the Nanophotonics group at the University of St Andrews and Jing Ma from the Jiangnan University in China. Robert Hunter, Duncan Robertson, and Graham Smith designed and verified the characterisation equipment. Sebastian Schulz aided in designing the experiments and project direction. Jing Ma designed the meta-atoms and conducted the experiments. Jing Ma’s supervisor was Jicheng Wang. Everyone contributed to writing the paper.

I collaborated on the Patterning Multicolor Hybrid Perovskite Films via Top-Down Lithography paper with Jonathon Harwell and Ifor Samuel from the Organic Semiconductor Optoelectronics group at the University of St Andrews. This collaboration also included Alasdair Fikouras and Malte

Gather from the Soft Matter Photonics group at the University of St Andrews. Here, I acted as a consultant for Jonathon Harwell about lithography techniques and fabricated the electron beam lithography samples. Everyone contributed to writing the paper.

Stand down,

I have the high ground.

Publications and Awards

Publications Resulting from this Work

- **Burch James**, Ma Jing, Hunter Robert, Schulz Sebastian, Robertson Duncan, Smith Graham, Wang Jicheng, and Di Falco Andrea ’Flexible patches for millimeter wavelength holography’ Applied Physics Letters, 115 (2019).
- **Burch James**, and Di Falco Andrea ’Holography Using Curved Metasurfaces’ MDPI Photonics, 6(1), 1-8 (2019).
- **Burch James**, and Di Falco Andrea ’Surface Topology Specific Metasurface Holograms’ ACS Photonics, 5(5), 1762-1766 (2018).
- **Burch James**, and Di Falco Andrea ’Holographic Device Patent’ UK patent number GB1719588.4 (2018).
- **Burch James**, Wen Dandan, Chen Xianzhong, and Di Falco Andrea ’Conformable Holographic Metasurfaces’ Scientific Reports, 7, 4520 (2017).

Other Publications

- Harwell Jonathon R., **Burch James**, Fikouras Alasdair, Gather Malte, Di Falco Andrea, and Samuel Ifor ’Patterning Multicolor Hybrid Perovskite Films via Top-Down Lithography’ ACS Nano, 13(4), 3823–3829 (2019).

Conferences

- **Burch James**, and Di Falco Andrea ’Surface Topology Specific Metasurface Holograms’ Metamaterials, Espoo Finland. Presentation, presented by **Burch James** (2019).
- **Burch James**, Wen Dandan, Chen Xianzhong, and Di Falco Andrea ’Conformable Holographic Metasurfaces’ Rank Prize Symposium, Grasmere UK. Presentation, presented by **Burch James** (2017).
- **Burch James**, Wen Dandan, Chen Xianzhong, and Di Falco Andrea ’Conformable Holographic Metasurfaces’ Nanometa, Tirol Austria. Presentation, presented by **Burch James** (2017).
- **Burch James**, Wen Dandan, Chen Xianzhong, and Di Falco Andrea ’Flexible Broadband Holographic Metasurfaces’ PECS XII, York UK. Poster, presented by **Burch James** (2016).

Awards and miscellaneous

- St Andrews PhD Poster Prize 1st place, awarded by the University of St Andrews (2018).
- Cover issue of the special Issue of ACS Photonics titled ’Ultra-capacity Metasurfaces with Low Dimension and High Efficiency’ (2018).
- Runner up to the Arthur Maitland Prize, awarded by the University of St Andrews (2017).
- Runner up poster prize, awarded by the Nature Group, at PECS XII York UK (2016).

Contents

Chapter 1

Introduction

This chapter introduces the main topics of this thesis and provides context for the work. Following this, it concludes with an outline of this thesis.

1.1 Basic holography concepts

The term hologram is frequently misused in popular media and has taken to mean any object with iridescent colours or a three-dimensional effect. In particular, the Pepper's ghost technique, which uses a partially reflective surface to mix an image with the background, is not a hologram, e.g. the Tupac 'hologram' [1, 2].

Instead, a hologram encodes a whole light field by capturing both the intensity and direction of each light ray and encoding it using phase information [3]. A standard image, in contrast, encodes only the intensity information from a light field. Accordingly, holograms exhibit depth-of-field and parallax effects within a limited field of view (which practically, can be large [4, 5]) and standard images do not. Holograms can be further categorised as reflection or transmission. Reflection holograms create a holographic image on the same side as the illumination source and transmission holograms on the opposite side of the hologram [6, 7].

To avoid imprecise terminology, this thesis refers to the holographic medium as the hologram and the resultant image from illuminating the hologram is referred to as the holographic image.

The ability to perfectly recreate an object in three-dimensions is of considerable interest for optical components [8, 9], displays [10], anti-counterfeiting applications [11], and the manipulation and storage of information [12, 13].

Holograms encode the direction of light by exploiting interference effects. A wave of light, where the time component has been ignored for simplicity, can be described by the wavefunction,

$$U_i(\mathbf{r}) = A_i(\mathbf{r}) \exp(i\phi_i(\mathbf{r})), \tag{1.1}$$

where $A_i(\mathbf{r})$ is the amplitude, and $\phi_i(\mathbf{r})$ is the phase at the position $\mathbf{r}$ [6, 7].

When two such waves linearly combine (with equal frequencies and polarisations) the overall intensity can be described as

$$\begin{aligned} I(\mathbf{r}) &= |U_1(\mathbf{r}) + U_2(\mathbf{r})|^2 \\ &= U_1(\mathbf{r})U_1^*(\mathbf{r}) + U_2(\mathbf{r})U_2^*(\mathbf{r}) + U_1(\mathbf{r})U_2^*(\mathbf{r}) + U_2(\mathbf{r})U_1^*(\mathbf{r}) \\ &= I_1(\mathbf{r}) + I_2(\mathbf{r}) + U_1(\mathbf{r})U_2^*(\mathbf{r}) + U_2(\mathbf{r})U_1^*(\mathbf{r}), \end{aligned} \tag{1.2}$$

where $I_i(\mathbf{r})$ is the intensity of the complex wave $U_i(\mathbf{r})$. The term $U_1(\mathbf{r})U_2^*(\mathbf{r}) + U_2^*(\mathbf{r})U_1(\mathbf{r})$ describes the interference of the two waves, where positive and negative terms represent the constructive and destructive interference [14].

1.2 Photosensitive plate realisation

The first holograms were recorded using photosensitive holographic chemical plates adopting a scheme similar to figure 1.1(a) [7, 15, 16].

Here, light is emitted from a single laser source with high spatial and temporal coherency. The high spatial and temporal coherence is a requirement because the intensity of the interference pattern must be stationary on the photosensitive plate to encode the holographic image [3]. Spatial coherence describes the ability for the waves in two spatially separated points, r_1 and r_2, to interfere

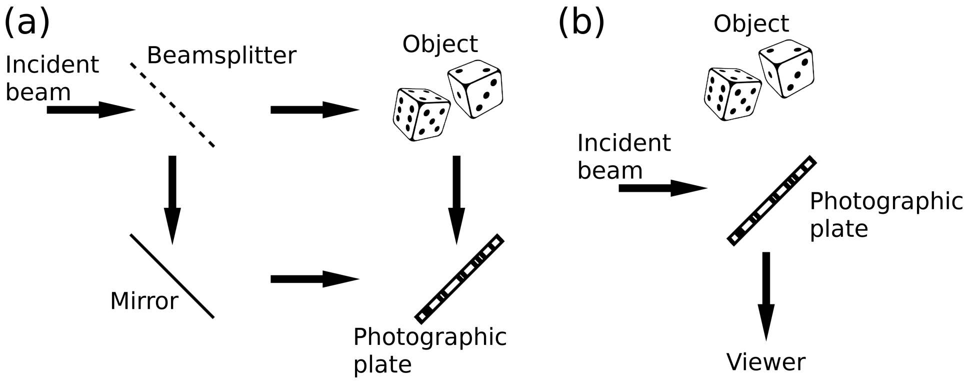

Figure 1.1: Illustration of holographic image (a) recording and (b) reconstruction creating a virtual holographic image.

as measured by the average correlation. Temporal coherence describes the ability for the waves at different points in time, t_1 and t_2, to interfere, and is measured the same way [14].

As shown in figure 1.1, the laser light is separated along the two paths by a beam splitter. The beam along the reference path is reflected by a planar mirror onto the holographic plate. The beam along the object path scatters off the object before interfering with the reference path on the photosensitive plate. The complex waves interfering on the photosensitive plate can be denoted as $U_r(\mathbf{r})$ and $U_o(\mathbf{r})$ for the reference beam and the object respectively [3]. The resulting complex wave can be written as

$$U(\mathbf{r}) = U_r(\mathbf{r}) + U_o(\mathbf{r}), \tag{1.3}$$

which describes the interference pattern that is written into the photosensitive plate.

The intensity of equation 1.3, similar to equation 1.2, can then be given as

$$\begin{aligned} I(\mathbf{r}) &= U_r(\mathbf{r})U_r^*(\mathbf{r}) + U_o(\mathbf{r})U_o^*(\mathbf{r}) + U_r(\mathbf{r})U_o^*(\mathbf{r}) + U_o(\mathbf{r})U_r^*(\mathbf{r}) \\ &= I_r(\mathbf{r}) + I_o(\mathbf{r}) + U_r(\mathbf{r})U_o^*(\mathbf{r}) + U_o(\mathbf{r})U_r^*(\mathbf{r}). \end{aligned} \tag{1.4}$$

1.2.1 Amplitude holograms

Hologram recording

The simplest method to record interference fringes involves a holographic plate with absorption that varies with the intensity of the recorded light. This type of hologram is called an amplitude hologram [3].

The photosensitive plate exhibits an approximately linear response within the expected range of operating intensities. After the photosensitive plate is developed, the amplitude profile of the photosensitive plate can be found using equation 1.4 as

$$\begin{aligned} h(\mathbf{r}) &= h_0 + \beta\tau I(\mathbf{r}) \\ &= h_0 + \beta\tau \left[U_r(\mathbf{r})U_r^*(\mathbf{r}) + U_o(\mathbf{r})U_o^*(\mathbf{r}) + U_r(\mathbf{r})U_o^*(\mathbf{r}) + U_o(\mathbf{r})U_r^*(\mathbf{r})\right]. \end{aligned} \tag{1.5}$$

Here, h_0 is the offset, β is the slope of the transmittance curve constant, and τ is the exposure time. β is positive for positive photoresists and negative for negative photoresists.

Hologram reconstruction

Information about the object is perfectly encoded into the holographic plate by these amplitude variations. To reconstruct the hologram, the holographic plate is illuminated with a reconstruction beam [3, 6, 7], as shown in figure 1.1(b). This reconstructed complex wavefront can be written mathematically as

$$\begin{aligned} U_I(\mathbf{r}) &= h(\mathbf{r})U_r(\mathbf{r}) \\ &= h_0U_r(\mathbf{r}) + \beta\tau \left[U_r(\mathbf{r})U_r^*(\mathbf{r}) + U_o(\mathbf{r})U_o^*(\mathbf{r}) + U_r(\mathbf{r})U_o^*(\mathbf{r}) + U_o(\mathbf{r})U_r^*(\mathbf{r})\right] U_r(\mathbf{r}) \\ &= h_0U_r(\mathbf{r}) + \beta\tau \left[|U_r(\mathbf{r})|^2U_r(\mathbf{r}) + |U_o(\mathbf{r})|^2U_r(\mathbf{r}) + |U_r(\mathbf{r})|^2U_o^*(\mathbf{r}) + |U_r(\mathbf{r})|^2U_o(\mathbf{r})\right]. \end{aligned} \tag{1.6}$$

This reconstructed complex wavefront comprises multipled terms. The first terms, $h_0U_r(\mathbf{r}) + \beta\tau\left[|U_r(\mathbf{r})|^2U_r(\mathbf{r}) + |U_o(\mathbf{r})|^2U_r(\mathbf{r})\right]$, are undiffracted and are typically called the zeroth order as they are relate to a modified reference beam. The fourth term, $|U_r(\mathbf{r})|^2 U_o^*(\mathbf{r})$, is proportional to the complex conjugate of the object beam, $U_o^*(\mathbf{r})$, and represents the real holographic image of the object but appears distorted. The final term, $|U_r(\mathbf{r})|^2 U_o(\mathbf{r})$, is proportional to the object beam, $U_o(\mathbf{r})$, and represents the virtual holographic image of the object. This term appears identical to the object but because the hologram was created by illuminating the object at one angle, the holographic image only shows the object within a limited field-of-view.

For the fourth and final terms, the proportional factor, $\beta\tau|U_r(\mathbf{r})|^2$, dictates the brightness of the final holographic image. Also, for off-axis holography, the virtual holographic image (representing the object) is spatially separated from the zeroth order and the real holographic image terms.

1.2.2 Phase holograms

Hologram recording

Another approach is to choose a holographic plate where its refractive index varies with the intensity of the interfering light. This type of hologram is called a phase hologram because it redirects light instead of absorbing it. This leads to phase holograms having higher efficiencies than amplitude holograms. The operating principle of phase holograms is detailed below.

Equation 1.1 can be substituted for the reference and object beams in 1.4 to find an equation for the intensity on the photographic plate in terms of phase

$$\begin{aligned} I(\mathbf{r}) &= I_r(\mathbf{r}) + I_o(\mathbf{r}) + A_o(\mathbf{r})A_r(\mathbf{r})\left[\exp(-i\phi_o(\mathbf{r}))\exp(i\phi_r(\mathbf{r})) + \exp(i\phi_o(\mathbf{r}))\exp(-i\phi_r(\mathbf{r}))\right] \\ &= I_r(\mathbf{r}) + I_o(\mathbf{r}) + A_o(\mathbf{r})A_r(\mathbf{r})\left[\exp(i\phi_T(\mathbf{r})) + \exp(-i\phi_T(\mathbf{r}))\right] \\ &= I_r(\mathbf{r}) + I_o(\mathbf{r}) + 2A_o(\mathbf{r})A_r(\mathbf{r})\cos(i\phi_T(\mathbf{r})). \end{aligned} \tag{1.7}$$

Here, $\phi_T(\mathbf{r}) = \phi_o(\mathbf{r}) - \phi_r(\mathbf{r})$ and represents the difference in phase between the object and reference beams.

The photosensitive plate exhibits an approximately linear response within the expected range of operating intensities. The $I_r(\mathbf{r}) + I_o(\mathbf{r})$ terms can be neglected as only the local variations in the phase cause the interference fringes. As such, after the photosensitive plate is developed, the effective thickness of the plate can be written as

$$\Delta T(\mathbf{r}) = \gamma\tau \times 2A_r(\mathbf{r})A_o(\mathbf{r})\cos(\phi_T(\mathbf{r})), \tag{1.8}$$

where γ is the photosensitivity constant for the photosensitive plate.

After exposure, the phase-shift written into the photosensitive plate can then be found by multiplying the effective thickness, $T(\mathbf{r})$, by the wavevector, $k = \frac{2\pi}{\lambda}$, as

$$\psi(\mathbf{r}) = k\gamma\tau \times 2A_r(\mathbf{r})A_o(\mathbf{r})\cos(\phi_T(\mathbf{r})). \tag{1.9}$$

If the hologram exposure has been tailored correctly, $\psi(\mathbf{r}) = \phi_T(\mathbf{r})$ and so the resultant hologram can be written as

$$h(\mathbf{r}) = A_h \exp(i\phi_T(\mathbf{r})), \tag{1.10}$$

where A_h is constant describing the amplitude of the hologram.

Hologram reconstruction

To reconstruct the hologram, again the holographic plate is illuminated with a reconstruction beam [3, 6, 7], as shown in figure 1.1(b). This reconstructed complex wavefront can be written mathematically as

$$\begin{aligned} U_I(\mathbf{r}) &= h(\mathbf{r})U_r(\mathbf{r}) \\ &= A_h \exp(i\phi_T(\mathbf{r}))U_r(\mathbf{r}) \\ &= A_h \exp(i\phi_o(\mathbf{r}))\exp(-i\phi_r(\mathbf{r}))U_r(\mathbf{r}) \\ &= A_{hi}U_o(\mathbf{r})U_r^*(\mathbf{r})U_r(\mathbf{r}) \\ &= A_{hi}|U_r(\mathbf{r})|^2U_o(\mathbf{r}), \end{aligned} \tag{1.11}$$

where $A_{hi} = \frac{A_h}{A_r(\mathbf{r})A_o(\mathbf{r})}$ and is a constant describing amplitude. $A_{hi}|U_r(\mathbf{r})|^2$ then describes the brightness of the final holographic image.

Equation 1.11 is proportional to the object beam, $U_o(\mathbf{r})$, and represents the virtual holographic image of the object. It appears identical to the object but, similar to amplitude holograms, because the hologram was created by illuminating the object at one angle, the holographic image only shows the object within a limited field-of-view.

1.3 Digital holography

1.3.1 Basic concepts

A significant step forward for holography was the invention of digital holography (DH). DH allows for aspects of conventional photosensitive plate holography to be replaced with digital components. This decreases the cost of holography and greatly simplifies hologram creation. Furthermore, digital holograms can be easily modified and copied in software, and thus are more convenient.

Recording with digital holography

The hologram capture setup, as shown in figure 1.1(a), can be improved by replacing the photosensitive plates with a charge coupled device (CCD). Practically, to effectively capture a discretised copy of the interference fringes, the pitch of the CCD must be sufficiently small compared to the wavelength of the light. An additional benefit of digital recording is that the amplitude transmission offset term, h_0, in equation 1.5 can be ignored [6, 7].

An alternate approach is to use computer generated holography (CGH) to create a digital hologram without needing any real-world setup. The main advantage of this approach is that the object does not need to be created. This simplifies capturing holograms of moving/weakly-reflective objects and allows for holograms that possess unphysical characteristics.

Reconstruction with digital holography

The hologram reconstruction setup, as shown in figure 1.1(b), can also be improved if one has a digital copy of the hologram.

The hologram can be encoded onto a spatial light modulator (SLM), which when illuminated by a reference beam reconstructs the holographic image. A SLM modulates the amplitude-shift, phase-shift, or both of incident light point-by point by adjusting the orientation of birefringent liquid crystals, similar to a liquid crystal display (LCD). This can be used to create holographic videos instead of static holographic images [7]. Alternatively, the digital hologram can be encoded into physical material. Such an object could overcome some of the shortcomings of SLMs by exhibiting a sub-wavelength pitch. This improves the diffraction efficiency and holographic image quality, and is expanded upon in the following sections of this thesis.

In the all-digital approach, a reconstruction of the hologram can be performed using equation 1.6, removing the need for any physical reconstruction apparatus.

1.4 Metamaterials and metasurfaces

By defining individual structured building blocks called meta-atoms, a metamaterial (MM) can be created with scattering properties that are determined point-by-point. This structuring allows for MMs to exhibit different properties to their natural constituent material for novel optical, mechanical, or acoustic effects [17, 18]. This thesis, however, only refers to optical MMs.

Standard MMs suffer from drawbacks in their fabrication and optical losses. As a result, much recent MM activity has focused on a two-dimensional form called a metasurface (MS). These MSs are of sub-wavelength thickness, typically 40-100 nm, and can be fabricated in one lithography step [19, 20]. Furthermore, because MSs present less material for the incident light to interact with, the losses are typically lower than for MMs [19, 20].

The benefits of MSs have been applied in a wide variety of applications including polarisation manipulation [21], tunable absorption [22, 23], laser steering [24, 25], and signal modulation [26]. A selection of these MS designs are displayed in figure 1.2.

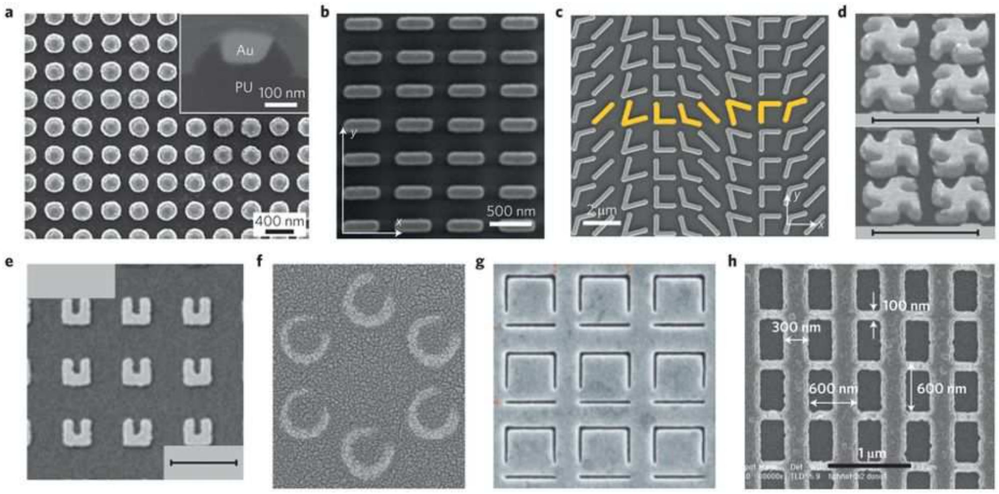

Figure 1.2: Common meta-atom designs as found in the literature [20]. Each meta-atom has been designed to interact with light through its plasmonic resonances.

Furthermore, the essentially two-dimensional form factor of MSs is ideally exploited in flexible implementations. To date, this has enabled lab-on-fibre, cloaking, filtering, and optically active three-dimensional applications [27, 28, 29, 30, 31, 32].

1.4.1 Metasurface holograms

Holographic metasurface (HMS) designs are also the ideal platform for encoding CGH, as both the phase and amplitude can be modulated on a sub-wavelength scale with high efficiency [24, 33, 34, 35, 36, 37]. Furthermore, the wide variety of HMS designs allows for novel effects such as encoding information in the polarisation [11, 38, 39, 40, 41], wavelength [42, 43], angle [44], and image dimensionality [45].

Because of these advantages, HMSs have found applications in the areas of displays [10], security [11], and the manipulation and storage of information [12, 13].

1.4.2 Flexible metasurface holograms

Flexible holographic metasurfaces (FHMSs) promise to expand the applications of state-of-the-art rigid HMSs in three main ways.

First, FHMSs conform to real-world, non-planar substrates. This allows for advanced photonic devices on clothing, packaging, and contact lenses. To date, this has been explored (in theory) to compensate for the spherical aberration of cylindrical lenses, and for carpet cloaking [9]. Further work has decoupled the function of FHMSs from their shape to enable both convex and concave lenses to converge light [46].

Second, FHMSs can be produced with roll-to-roll fabrication methods, which are in principle faster and more economical than rigid HMS fabrication methods. For this reason, roll-to-roll compatibility is the preferred path for HMS commercialisation [47, 48].

Third, FHMSs can be tuned through stretching or bending to alter the properties of the resultant holographic image. This technique has been explored to create FHMS devices that encode holographic information in their degree of elastic stretching, e.g. to vary the focus of a lens [49], and to switch between multiple images in the near-field [50].

1.5 Huygens' sources

An additional concept for holography is that of Huygens' sources, which are used extensively in chapter 2. The Huygens' principle states that every point on a wavefront acts as a new light source, and that the sum of these light sources forms the wavefront [51, 52, 53]. This principle is valid when scalar diffraction theory is used and polarisation is neglected. A plane wave can then be considered as an infinite array of Huygens' sources. Each Huygens' source emits secondary spherical wavefronts, and the interference of these adjacent sources creates the plane wave. When an obstacle partly occludes the secondary Huygens' sources, e.g. a narrow slit, the interference of adjacent sources is altered, and the spherical nature of the wave is revealed. This effect is displayed in figure 1.3.

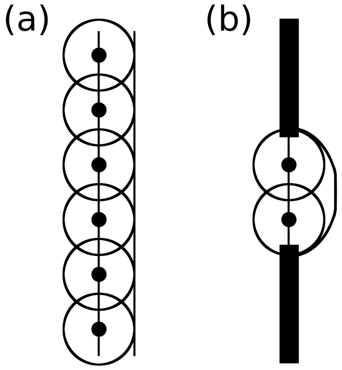

Figure 1.3: Illustration of Huygens' source propagation in (a) a plane wave (a) and (b) through a small gap. (b) shows that curved wavefronts can occur when a planar wavefront is partially occluded.

1.5.1 Resolution limit for holography

The interference of the Huygens' sources sets the ultimate Abbe resolution, R, of the hologram (for both digital and photochemical plates) and depends on the wavelength of the illumination, λ, and the numerical aperture (NA) of the hologram [54, 55]. This Abbe resolution can be described by

$$R = \frac{\lambda}{2NA}, \tag{1.12}$$

where the NA can be defined by

$$NA = n \times \sin(\theta), \tag{1.13}$$

and figure 1.4.

Here, n defines the refractive index of the medium, where $n = 1$ for air.

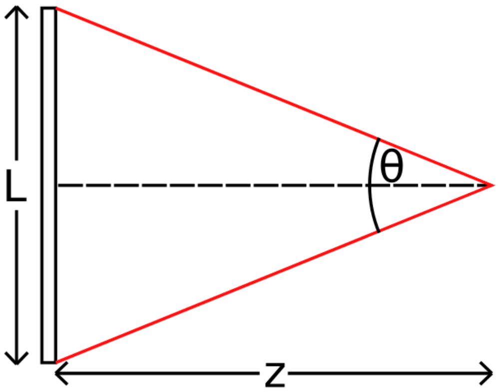

Figure 1.4: Illustration of the NA where L and z are the physical size of the hologram and the distance from the hologram respectively.

In equation 1.13, $\sin(\theta)$ increases with L. Consequently, equation 1.12 dictates that for a set wavelength, larger holograms create more resolved features. Therefore, holograms are typically designed so that $L > 100 \times \lambda$.

1.6 Comparing metals and dielectrics for metasurface holography

Controlling light using sub-wavelength features requires an understanding of how light interacts with the features. There are two types of material used in HMSs, metals and dielectrics, which are compared below.

1.6.1 Metals

For this thesis, the relevant interactions between the metal and the light are either through localised plasmons or geometrical resonances. Which interaction is relevant depends on the frequency of the incident light compared to the plasma frequency of the metal, and is further described in this section.

Plasmonic resonances

When the incident light has a frequency close to the plasma frequency of the material, localised plasmons are generated in the metal. This plasma frequency can be described as

$$\omega_{pe} = \sqrt{\frac{n_e e^2}{m^* \epsilon_o}}, \tag{1.14}$$

where n_e is the number density of the electrons, e is the charge of the electron, m^* is the effective mass of the electron, and ϵ_o is the permittivity of free space.

A plasmon is an oscillation of free electrons within a material, typically a metal, with respect to the stationary electrons and ions. When an electric field operates on a material, electrons within the material attempt to move to cancel this electric field. In the case of a static applied electric field, plasmons are not created because there is no oscillatory behaviour. Once the field is removed, electrons flow towards the positive ions and away from the neighbouring electrons. The electrons are then set in oscillation at the plasmon frequency of the material until dampening (the result of electron-electron or electron-proton collisions) removes all of the plasmons' energy. Localised plasmons, as generated when an oscillating electric field illuminates a sub-wavelength structure, do not propagate, unlike other types of plasmons [56].

If light incident on a material is below the plasmon frequency, electrons in the material can quickly oscillate to cancel the incident electric field within the material. This has the effect of imposing a rigid boundary condition on the incident electric field and forcing it to be predominantly reflected. This effect is further detailed below. In the case that the incident light has a frequency above the plasmon frequency, the electrons in the material cannot oscillate quickly enough to cancel the incident electric field within the material. As a result, the incident electric field can propagate through the material, often with some attenuation. In a metal, the plasmon frequency is typically in the ultraviolet (UV) range; however, in dielectrics this frequency can be even higher into the deep UV region [57]. Due to this, metals appear shiny as the visible frequencies are reflected. Some metals (e.g. copper and gold), have interband transitions, which absorb the light at particular frequencies. In the case of gold, there is an interband transition at blue frequencies ($\approx$ 400 nm). Because blue is thus more strongly absorbed than red or yellow light, white light incident on gold surfaces is typically reflected with a golden colour [58].

By tailoring materials at the nanoscale, the coupling and resonation of particular plasmons can be controlled. This is a broad technique with applications in wide-ranging fields from imposing structural colour [59, 60], to surface enhanced Raman spectroscopy [61, 62].

This method can also be used for holography [11, 33], where the length and width of nanostructures are tailored to impart a phase-shift. Furthermore, because these meta-atoms have broad resonances, they are both relatively broadband and dispersionless [11, 33]. This broadband half-waveplate is the building block throughout much of this thesis.

Geometric resonances

When the incident light has a much lower frequency than the plasma frequency, described with equation 1.14, the electrons are able to respond effectively instantaneously to the incident electric field. As a result, plasmons are not generated, however, geometrical resonances can still be supported. The relevant geometry for this thesis is the c-ring resonator, as shown in figure 1.5, which exhibits: capacitance, inductance, and resistance. This c-ring thus behaves as an LCR circuit.

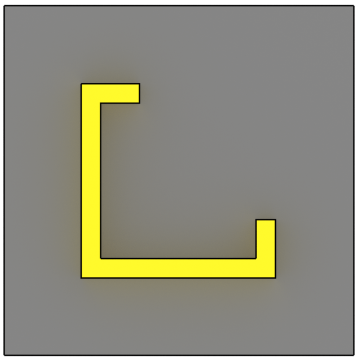

Figure 1.5: A standard metallic c-ring antenna (in yellow) on a dielectric substrate (in grey).

The c-ring is resonant because, when the capacitance discharges an electric current is created which increases the magnetic inductance and, when the inductance collapses an electric current is created which charges the capacitance. Consequently, without further input from a source, this process repeats continually until the resistance dissipates the energy in the c-ring resonator.

The geometric resonant frequency of the c-ring resonator can be described as

$$\omega_g = \frac{1}{LC}, \tag{1.15}$$

where L is the inductance and C is the capacitance of the resonator.

By tailoring the exact geometry of the c-ring, L and C can be ajusted and thus ω_g. Furthermore, the phase-shift introduced by the c-ring to incident electromagnetic (EM) radiation can also be tailored.

1.6.2 Dielectrics

Dielectrics do not have free electrons, as metals do, to oscillate as a plasmon. They do, however, allow the incident light to resonate inside them.

There are advantages in using dielectrics over plasmonics for holography. First, dielectrics can support lower losses, in particular, for higher frequencies where plasmonics become extremely lossy [35, 57]. As such, dielectric holograms can be highly efficient and operate at UV wavelengths. Second, dielectrics are compatible with complementary metal-oxide-semiconductor (CMOS) fabrication techniques, which are well-optimised and commonplace. Third, dielectrics are often cheaper than their plasmonic counterparts. Common dielectrics include titanium dioxide and silicon, whereas common plasmonic metals include gold, silver, and aluminium.

The main disadvantage of dielectrics is that their fabrication is more complicated and typically slower. Much of this originates from dielectrics having a less dramatic effect on incident light. For an example, tall nanofins could be required, whereas conventional plasmonic designs could use short nanorods. An example of a nanofin HMS is shown in figure 1.6. Creating tall nanofins requires vertical sidewalls with almost no leaning, which is challenging to fabricate. Furthermore, even highly sub-wavelength surface defects on the nanofins can significantly decrease their efficiency [8, 63].

The refractive index and the shape of the dielectric control which resonances are supported [9],

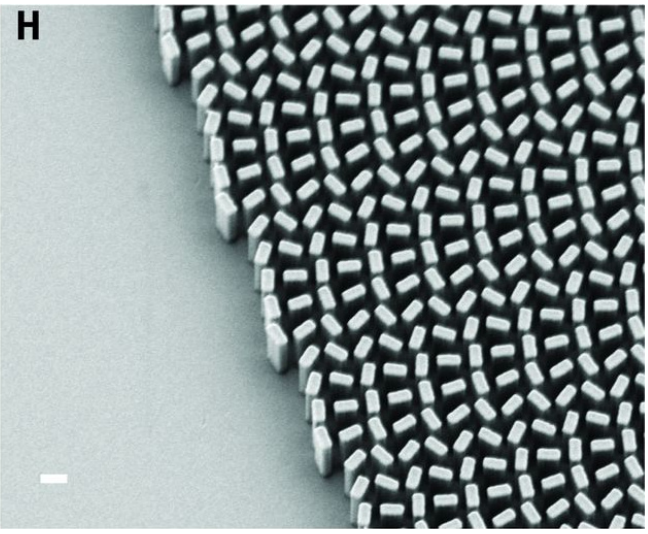

Figure 1.6: A SEM image of dielectric (TiO_2) nanofins [64].

where a higher refractive index 'slows' the light enabling more wavelengths to fit into the same physical space.

Here, similar to the plasmonic case, the length and width of the nanostructures can be tailored to support different resonances along their axes, which is often called shape birefringence. As in the plasmonic case, this can be applied to create half-waveplates [8, 63].

1.6.3 Holographic metasurface material for reflection vs transmission

Designs based on metals can produce high efficiency holograms across the visible wavelength range (up to 80%) [33] when used with a reflective metal backplate. However, ohmic losses and the fundamental constraints of their thin form factor limit their practical application in transmissive designs [65, 66]. Dielectric designs do not have these ohmic losses, and so can be made in a thicker form factor. As a result, dielectric designs can reach higher efficiencies in transmission (above 86%) [8, 67]. Reflecting light with dielectrics is more challenging though, thus standard reflection designs use metals.

1.7 Thesis structure

This introductory chapter has set-out the fundamental principles that underpin this work.

Chapter 2 details the design of a hologram recovery algorithm, and the particular implementation of a visible light meta-atom used in this thesis. It also provides a study on how the hologram parameters affect the holographic image.

Chapter 3 describes the fabrication procedures for the visible and the millimetre wavelength HMSs used in this thesis.

Chapter 4 outlines work to create visible light FHMSs, including the hologram design and the characterisation in an experiment. It also reports on a novel symmetry property, which relates the helicity of the incident polarisation to the surface topography of the hologram.

Chapter 5 communicates the concept, hologram design, and initial experiments for creating a greatly simplified light sheet fluorescent microscopy (LSFM) design compared to the state-of-the-art. This LSFM design embeds all of the complexity of the incident/collection optics into the HMS.

Chapter 6 conveys work on HMSs operating in the millimetre wave range. In particular, it outlines the meta-atom design process, hologram design, and the characterisation in an experiment.

Chapter 7 disseminates some of my unpublished work and the context for it. It focusses on holography using partially incoherent light, near-field holographic image multiplexing with the surface topography of the hologram, and a multi-layer HMS design for tunable applications.

Finally, chapter 8 summarises the work of this thesis and describes the outlook.

CHAPTER 2

Theory and simulation

This chapter outlines the DH methods which were instrumental to the work of this thesis. In particular, it focuses on the Gerchberg-Saxton algorithm (GSA) and a numerical integration light propagation algorithm. The validity of the numerical integration technique is also discussed here. These algorithms were essential to enable the design of holograms for non-flat surfaces, which greatly expands the number of applications of HMSs. Finally, this chapter describes the physics behind the visible light meta-atoms that were adopted throughout the majority of this thesis.

2.1 Iterative phase retrieval using the Gerchberg-Saxton algorithm

A method was needed to generate holograms from the target image, source intensity distribution, and the key parameters (e.g. hologram pitch and source wavelength). In traditional non-DH, this target is a physical object, however for the DH in this thesis, the target is an image, e.g. a ′.jpg′ or ′.png′ file.

The standard algorithm to generate a hologram is called the GSA [68]. This algorithm is illustrated in figure 2.1, with a Gaussian source intensity distribution and a target of a hummingbird. The GSA considers two spatially separated planes (the hologram plane and the holographic image plane) and converges to the proper solution for the hologram over many iterations, hence being named iterative phase retrieval. The operation of the GSA is described in algorithm 1 with example code in appendix A.

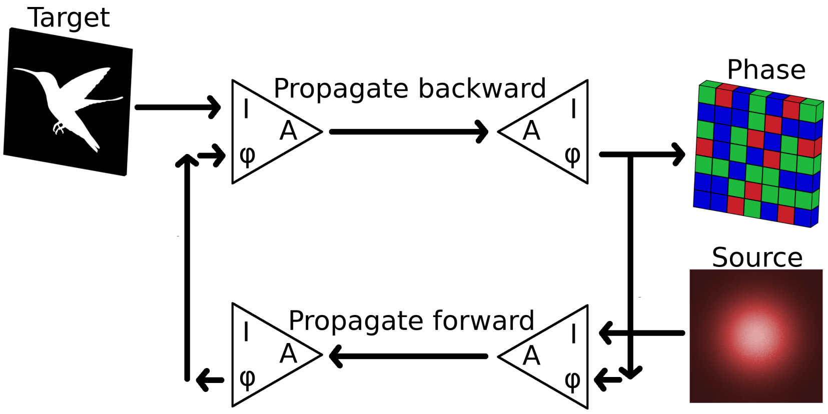

Figure 2.1: Illustration of the GSA. The propagation can be performed with a FFT or the RS numerical integral.

Algorithm 1 Gerchberg-Saxton algorithm

```
1: Set the holographic image to the target image.
2: Propagate the holographic image to the hologram plane.
3: Discard the intensity information and substitute it for the intensity information of the illumination source.
4: Propagate this hologram forward to the holographic image plane.
5: Discard the intensity information and substitute it for the intensity information of the target image.
6: Calculate the least squares differences between the absolute values of the holographic image the target image, $\epsilon$. Repeat steps 2-6 if $\epsilon$ is greater than a predetermined value.
7: Return the hologram phase
```

The GSA requires propagating light between the hologram and holographic image planes [68], which is described fully later in this chapter.

After the GSA has output a hologram, it can be converted to a phase-only hologram by removing the amplitude information. Alternatively, an amplitude-only hologram can be output by removing the phase information, or, both parts can be kept [7, 69]. Examples of a 100×100 phase-only and amplitude-only hologram are shown in figure 2.2.

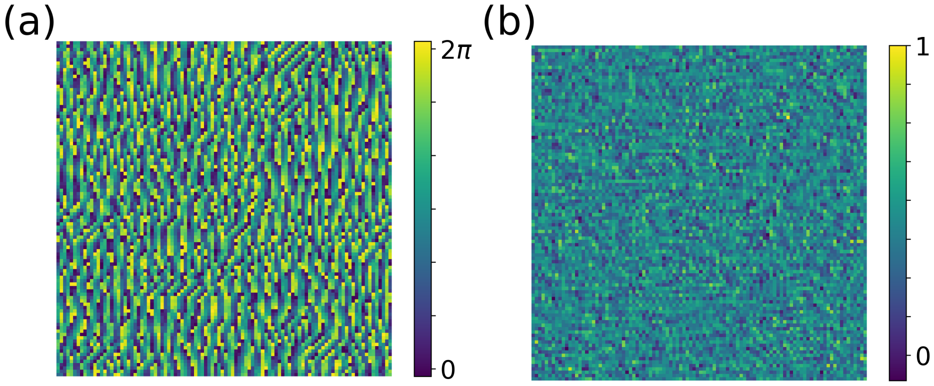

Figure 2.2: (a) Phase-only and (b) amplitude-only holograms. Each hologram is 100 × 100 pixels and is provided purely for illustrative purposes.

2.1.1 Refinements to the Gerchberg-Saxton algorithm

Over the years a few improvements to the GSA have been made. One problem with the GSA is that it gives rise to uneven brightness in the holographic image, in particular, when using a large field-of-view. This occurs because in the standard GSA there is no requirement for even brightness of the holographic image [70, 71]. This condition can be enforced, however, by replacing the brightness of the target, $target$, with $target - \alpha \times U_I$, where α is a tunable constant with a typical value of 0.05. U_I is the holographic image intensity distribution, as recovered by that iteration of the GSA.

The earlier work in this thesis does not use this correction as the uniformity of the holographic image illumination was not relevant to the underlying physics. However, this change was implemented in the work following 'Holograms for non-flat surfaces' in chapter 4, as it was simple to do.

2.2 Numerical light propagation methods

As discussed, the GSA requires propagating light between the hologram and the holographic image planes. Light propagation can be achieved using a FFT, or with the RS numerical integral. The advantage of the RS integral is that it models fuller dynamics of the propagating light. This was essential for the work in this thesis allowing, amongst other things, the use of arbitrarily shaped hologram and holographic image planes, and the design of holographic images that operate in the near-field. FFTs are simple to implement and highly optimised, and thus are the ideal method to generate simple holograms, e.g. two flat planes facing in the same direction with one in the far-field. In this thesis, FFTs are used in chapter 4 before the 'Holograms for non-flat surfaces' section, where RS integrals are used instead. The differences between FFTs and the RS numerical integral are discussed later in this chapter.

An important note for the reader, referrals to the RS propagation method in this thesis mean a numerical integration method, e.g. equation 2.9, and not directly related to Fourier transforms.

2.2.1 Derivation of the Rayleigh-Sommerfeld numerical integral

The Rayleigh-Sommerfeld integral requires making approximations. To understand the validity of these assumptions, a partial derivation is provided in this subsection.

First, the light is modelled with scalar diffraction theory and neglecting the polarisation with the Helmholtz equation as

$$\left(\nabla^2 + k^2\right) U = 0. \tag{2.1}$$

Here, k is the wavevector of the light and U represents the complex light field.

U at any observation point can be calculated using Green's theorem as

$$\int_V \left(U\nabla^2 G - G\nabla^2 U\right) dv = \int_S \left(U\frac{\partial G}{\partial n} - G\frac{\partial U}{\partial n}\right) ds, \tag{2.2}$$

where G represents a Green's function (in the form of an impulse response) and $\frac{\partial}{\partial n}$ is a partial derivative along the outwards normal direction at any point on S. This information is described by figure 2.3

The Green's function, G, at any arbitrary point P_1 is given by

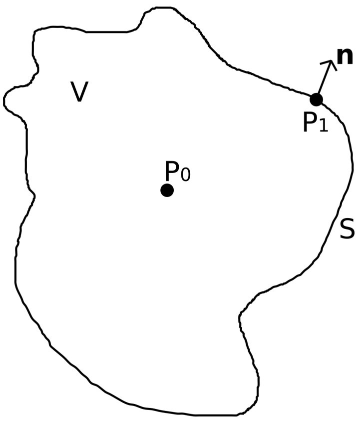

Figure 2.3: Integration on an arbitrary surface enclosing an volume for equation 2.2.

$$G(P_1) = \frac{\exp(ik|\mathbf{r}_{01}|)}{|\mathbf{r}_{01}|}, \tag{2.3}$$

where $\mathbf{r}_{01}$ is the vector between P_0 and P_1.

Remembering that $k = \frac{2\pi}{\lambda}$, and using equations 2.1, 2.3, and 2.3, the integral theorem of Helmholtz and Kirchoff can be found as

$$U(P_0) = \frac{1}{4\pi} \int_S \left[\frac{\partial U}{\partial n} G - U \frac{\partial G}{\partial n} \right] ds. \tag{2.4}$$

Under the assumptions of: the validity of the scalar theory, U and G satisfy the homogeneous scalar wave equation, and the Sommerfeld radiation condition is satisfied, the Green's function, G, can be modified while keeping equation 2.4 valid. For this, G or $\frac{\partial G}{\partial n}$ must vanish over the surface of the aperture.

In this case, Rayleigh and Sommerfeld showed that by using a smart choice for G, it can be written that

$$U(P_0) = \frac{1}{4\pi} \int_S \left[-2U \frac{\partial G}{\partial n} \right] ds. \tag{2.5}$$

The partial differential of G can be calculated from equation 2.3 as

$$\frac{\partial G(P_1)}{\partial n} = \cos(\mathbf{n}, \mathbf{r}_{01}) \left(ik - \frac{1}{|\mathbf{r}_{01}|} \right) \frac{\exp(ik|\mathbf{r}_{01}|)}{|\mathbf{r}_{01}|}, \tag{2.6}$$

where $\cos(\mathbf{n}, \mathbf{r}_{01})$ is the projection of the the normal to the aperture surface, $\mathbf{n}$, and $\mathbf{r}_{01}$.

Equation 2.6 can then be substituted into equation 2.5 to give the RS equation

$$U(P_0) = -\int_S \left[2U \cos(\mathbf{n}, \mathbf{r}_{01}) \left(ik - \frac{1}{|\mathbf{r}_{01}|} \right) \frac{\exp(ik|\mathbf{r}_{01}|)}{4\pi|\mathbf{r}_{01}|} \right] ds. \tag{2.7}$$

Equation 2.7 can be made more usable by writing it in terms of the Cartesian coordinate system. A diagram of the hologram and holographic image planes in this coordinate system is displayed in figure 2.4.

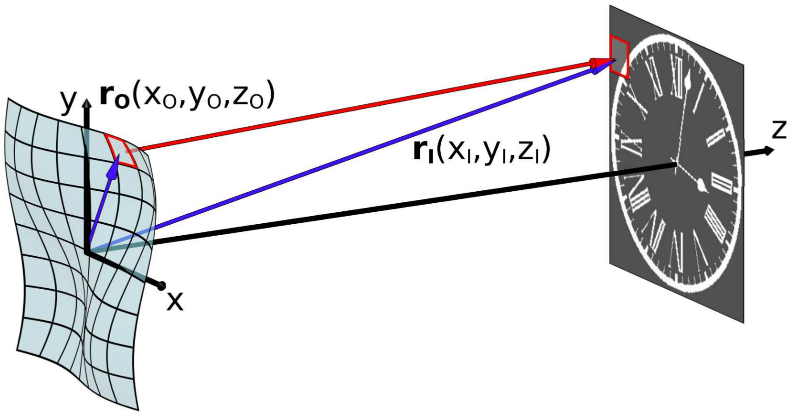

Figure 2.4: Illustration of light propagation using the RS equation from $\mathbf{r}_O(x_O, y_O, z_O)$ to $\mathbf{r}_I(x_I, y_I, z_I)$. The holographic image is projected from the HMS onto the screen [72].

In the Cartesian coordinate system, if the small angle approximation is valid for the projection of $(\mathbf{r}_I - \mathbf{r}_O)$ on $\mathbf{n}$, it can be written that

$$\cos(\mathbf{n}, (\mathbf{r}_I - \mathbf{r}_O)) = \frac{z_I - z_O}{|\mathbf{r}_I - \mathbf{r}_O|}. \tag{2.8}$$

This result can be substituted into equation 2.7 to find the Cartesian form of the RS equation [4, 73]

$$\begin{aligned} U(x_I, y_I, z_I) = &-\iint U(x_O, y_O, z_O) \frac{2(z_I - z_O)}{|\mathbf{r}_I - \mathbf{r}_O|} \\ &\times \left(ik - \frac{1}{|\mathbf{r}_I - \mathbf{r}_O|} \right) \times \frac{\exp(ik|\mathbf{r}_I - \mathbf{r}_O|)}{4\pi|\mathbf{r}_I - \mathbf{r}_O|} \, dx_O \, dy_O. \end{aligned} \tag{2.9}$$

Here, the complex light fields U are calculated at the coordinates (x_j, y_j, z_j) and are identified by the position vectors $\mathbf{r}_j$. The subscripts $j = O, I$ refer to the hologram and holographic image planes respectively. The origin of the coordinate system is the centre of a virtual, undistorted HMS as shown in figure 2.4.

2.2.2 The validity of the assumptions made to derive the Rayleigh-Sommerfeld numerical integral

The RS method models the propagating light as being composed of isotropically emitting Huygens' source [73]. This is an excellent approximation when the holographic image is formed far from a flat hologram.

When the holographic image is formed close to the hologram, however, the assumption that polarisation can be neglected is inaccurate and equation 2.4 must be used to propagate U. For the work in this thesis in the visible range, the closest distance between the hologram and the holographic image planes is $> 800\lambda$. In the millimetre wavelength range, this distance is $> 40\lambda$. Consequently, this assumption can be safely made in the visible range and with some caution in the millimetre wavelength range for the work in this thesis.

The other key assumption for the RS method is that the surface of the Huygens' sources comprising the hologram are approximately flat. This assumption is valid for small angles, where $\cos(\theta) \approx 1$, and allows equation 2.8 to be found. For the work in this thesis, the angle between the surface of the hologram and the incident light $\theta_{incident} < 10$ degrees, and thus this assumption is valid. θ_{inc} can be found for cylindrical surfaces, which are the only type of non-flat hologram surfaces used in this thesis, with $\theta_{inc} = \arctan(-x_O/z_O)$. For more dramatically curved holograms, the full equation 2.4 should be used, or the holographic image should be placed in the far-field. In the far-field, different approximations can be made to overcome this limitation [4].

2.2.3 Approximating the numerical integral

To then propagate light, the numerical integral can be evaluated point-by-point which, depending on the number of points which need to be evaluated, can be extremely computationally intensive. Because our computational resources and time were limited, it was interesting to approximate the numerical integral to speed it up and reduce the computational resources required. To describe this process, in the next section the reasonable approximations and their respective performances are evaluated.

The RS equation can be approximated in different ways depending on how far the holographic image is created from the HMS. These distances describe three regimes, as shown in figure 2.5, which are continuous with gradual transitions between them [52, 74].

Nearest to the HMS, there is the near-field region. Here, the energy is mostly confined to non-propagating evanescent modes.

Farther away there is the radiating near-field region, where the energy in a given angular distribution remains relatively constant with some local hot spots.

Farthest away there is the far-field region, where the energy emitted at a given angular distribution is constant, but the power decays according to the inverse square law with distance. The far-field is defined by the Fraunhofer condition as $distance \geq 2 \times D^2/\lambda$, where D is the maximum linear size of the antenna sources, and λ is the wavelength [75].

Because the non-radiating near-field is useless for holography [52], as the hologram cannot be projected onto a screen or CCD, throughout the rest of this thesis the near-field refers to the radiating near-field.

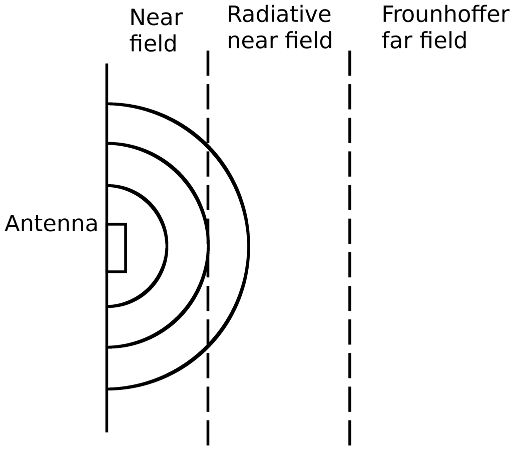

Figure 2.5: The three continuous regions created by a radiating antenna.

Far-field (Kirchoff) approximation

This method ignores the near-field component and so applies only in the far-field [73]. There are two terms in equation 2.9; however, once in the far-field, the fractional term $\frac{1}{|\mathbf{r}_I - \mathbf{r}_O|} \to 0$. Consequently, equation 2.9 can be written as

$$\begin{aligned} U(x_I, y_I, z_I) \approx -\iint U(x_O, y_O, z_O) \frac{2(z_I - z_O)}{|\mathbf{r}_I - \mathbf{r}_O|} \\ \times ik \times \frac{\exp(ik|\mathbf{r}_I - \mathbf{r}_O|)}{4\pi|\mathbf{r}_I - \mathbf{r}_O|}\, dx_O\, dy_O. \end{aligned} \tag{2.10}$$

Near-field approximation

Conversely, if in the near-field, the term ik is dominated by the larger $\frac{1}{|\mathbf{r}_I - \mathbf{r}_O|}$ term in equation 2.9 [73]. As such, one can write

$$\begin{aligned} U(x_I, y_I, z_I) \approx -\iint U(x_O, y_O, z_O) \frac{2(z_I - z_O)}{|\mathbf{r}_I - \mathbf{r}_O|} \\ \times \frac{1}{|\mathbf{r}_I - \mathbf{r}_O|} \times \frac{\exp(ik|\mathbf{r}_I - \mathbf{r}_O|)}{4\pi|\mathbf{r}_I - \mathbf{r}_O|}\, dx_O\, dy_O. \end{aligned} \tag{2.11}$$

Fourier approximation

This method makes a number of assumptions to convert equation 2.9 to a FFT under certain conditions. The most critical conditions, enforced by the assumptions, are far-field operation and a physically small holographic image compared to the distance between the hologram and the holographic image [69].

This first assumption is the Fresnel approximation, which states that if the variations in $z_I - z_O$ are small across the hologram, this value can be regarded as a constant [69]. Therefore, the Taylor expansion of 2.9 can be made as

$$\begin{aligned} |\mathbf{r}_I - \mathbf{r}_O| &= \sqrt{(x_I - x_O)^2 + (y_I - y_O)^2 + (z_I - z_O)^2} \\ &\approx (z_I - z_O) + \frac{(x_I - x_O)^2 + (y_I - y_O)^2}{2(z_I - z_O)}. \end{aligned} \tag{2.12}$$

Substituting this into equation 2.9, it can be found that

$$\begin{aligned} U(x_I, y_I) \approx -\iint U(x_O, y_O) \times \frac{2(z_I - z_O)}{|\mathbf{r}_I - \mathbf{r}_O|} \times ik \times \frac{1}{4\pi|\mathbf{r}_I - \mathbf{r}_O|} \\ \times \exp\left(ik\left[(z_I - z_O) + \frac{(x_I - x_O)^2 + (y_I - y_O)^2}{2(z_I - z_O)}\right]\right) dx_O\, dy_O. \end{aligned} \tag{2.13}$$

There are terms in equation 2.13 which do not significantly affect the local phase or amplitude. The global terms set the overall phase and amplitude for the holographic image, and the local terms set the relative variations within the global term. When a holographic image is created, the local terms set the interference, which creates patterns of bright and dark which we interpret as an image, and the global terms set the overall brightness. These global phase terms can be ignored, as only relative phase differences matter for the interference of Huygens' sources.

The global terms can be grouped as

$$\Gamma(\mathbf{r}_O, \mathbf{r}_I) = -\frac{2(z_I - z_O)}{|\mathbf{r}_I - \mathbf{r}_O|} \times \frac{ik}{4\pi|\mathbf{r}_I - \mathbf{r}_O|}. \tag{2.14}$$

Equation 2.13 can thus be rewritten as

$$\begin{aligned} U(x_I, y_I) \approx & \iint \Gamma(\mathbf{r}_O, \mathbf{r}_I) \times U(x_O, y_O) \\ & \times \exp\left(ik\left[(z_I - z_O) + \frac{(x_I - x_O)^2 + (y_I - y_O)^2}{2(z_I - z_O)}\right]\right) dx_O\, dy_O. \end{aligned} \tag{2.15}$$

This allows for the exponential term to be expanded, and through rearranging, it can be found that

$$\begin{aligned} U(x_I, y_I) \approx & \iint \Gamma(\mathbf{r}_O, \mathbf{r}_I) \times \exp(ik(z_I - z_O)) \times \exp\left(ik\left[\frac{x_I^2 + y_I^2}{2(z_I - z_O)}\right]\right) \times U(x_O, y_O) \\ & \times \exp\left(ik\left[\frac{x_O^2 + y_O^2}{2(z_I - z_O)}\right]\right) \times \exp\left(-ik\left[\frac{x_O x_I + y_O y_I}{z_I - z_O}\right]\right) dx_O\, dy_O. \end{aligned} \tag{2.16}$$

In the far-field, ignoring the constants as they only affect the global phase factor, $\Gamma(\mathbf{r}_O, \mathbf{r}_I)$ tends to $\frac{1}{z_I - z_O}$. In addition, the terms which only affect the global phase factor can be ignored by setting $\exp(ik(z_I - z_O)) \times \exp\left(ik\left[\frac{x_I^2+y_I^2}{2(z_I-z_O)}\right]\right) = 1$. Furthermore, $\exp\left(ik\left[\frac{x_O^2+y_O^2}{2(z_I-z_O)}\right]\right)$ can be ignored as this term tends to 1 because $z_I - z_O$, is large x_O and y_O are small. Accordingly, it can be written that

$$U(x_I, y_I) \approx \frac{1}{z_I - z_O} \iint U(x_O, y_O) \times \exp\left(-ik\left[\frac{x_O x_I + y_O y_I}{z_I - z_O}\right]\right) dx_O\, dy_O. \tag{2.17}$$

Remembering that $k = \frac{2\pi}{\lambda}$, and defining the scaled coordinates

$$\begin{aligned} v &= \frac{x_I}{\lambda(z_I - z_O)} \\ u &= \frac{y_I}{\lambda(z_I - z_O)} \end{aligned} \tag{2.18}$$

to help digitise equation 2.17, it can be written that

$$U(u, v) \approx \frac{1}{z_I - z_O} \iint U(x_O, y_O) \times \exp(-2\pi i(u x_O + v y_O))\, dx_O\, dy_O. \tag{2.19}$$

Equation 2.16 can now be compared to the standard two-dimensional Fourier transform,

$$F(u,v) \approx \iint f(x,y) \times \exp(-2\pi i(ux+vy))\, dx\, dy, \tag{2.20}$$

so that

$$U(u,v) \approx \frac{1}{z_I - z_O} FFT(U(x_O, y_O)). \tag{2.21}$$

Convolution Fourier transform approximation

A related method to Fourier transforms is convolution Fourier transforms, which can be described by the following equation

$$U(x_I, y_I, z_I) = \iint h(x_O, y_O) R(x_O, y_O) g(x_I, y_I, x_O, y_O)\, dx_O\, dy_O, \tag{2.22}$$

where $h(x_O, y_O)$ is the hologram function, $R(x_O, y_O)$ is the reference wave, and $g(x_I, y_I, x_O, y_O)$ is the impulse response [69]. The integral in equation 2.22 can thus be evaluated as the convolution of the individual Fourier transforms $FFT(hR)$ and $FFT(g)$. This approach shares the same limitations as a standard Fourier transform and thus was not adopted in this thesis. This information is provided solely for completeness.

2.2.4 Using the integral for holography

Regardless of the approximations made, the intensity of a given light field U_j at a given position (x_j, y_j, z_j) can be written as

$$I(x_j, y_j, z_j) = |U(x_j, y_j, z_j)|^2. \tag{2.23}$$

The corresponding phase can be written as

$$\phi(x_j, y_j, z_j) = \text{arctan}\left(\frac{Im(U(x_j, y_j, z_j))}{Re(U(x_j, y_j, z_j))}\right), \tag{2.24}$$

where Im and Re correspond to the imaginary, and real parts of $U(x_j, y_j, z_j)$ respectively [4, 7, 14].

This DH phase reconstruction allows for easy separation of the amplitude and phase of the hologram, which makes the differences between them more prominent. Amplitude-only holograms keep the overall phase constant and modulate the amplitude to encode a hologram. Typically, this is achieved by tailoring the absorption of the hologram point-by-point. The main advantage of this approach is its simplicity; However, it leads to low-efficiency holograms because a proportion of the incident light is absorbed.

Phase-only holograms keep the overall amplitude constant and instead modulate the phase. This allows for higher efficiency holograms compared to amplitude-only modulation.

Finally, there are full-holograms which encode both phase and amplitude. These full-holograms exhibit the highest efficiency, and produce the highest quality holographic images [4, 7] as they replicate the complete information of the hologram.

Throughout this thesis, phase-only holograms were used because they are easier to fabricate than the full-holograms and exhibit similar efficiencies.

2.3 Efficient light propagation algorithm design

As mentioned previously, light can be propagated with a numerical integration approach, or by using a FFT.

The numerical integration approaches include using: the full integral, equation 2.9; the far-field expression, equation 2.10; or the near-field expression, equation 2.22. The slowest approach is to calculate is the full integral because more terms need calculating and storing in memory than with the other approaches; however, it is more accurate as it does not make further approximations. Consequently, when the holographic image is firmly in the far-field or the near-field equation 2.10 or

2.22 should be used respectively. However, when the holographic image is between these regimes, the full integral 2.9 should be used. The appropriate approximation can be checked by comparing it to the result of the full integral.

Next, the FFT and numerical integration techniques are compared to evaluate their respective qualities.

Fourier transforms

FFTs are already highly optimised but lack the flexibility of numerical integration, in particular, for near-field holography and non-flat hologram/holographic image planes. FFTs are highly optimised as they are easily parallelised; thus their computation can be split into many individually calculated small pieces and recombined [76]. This allows for the computation speed to be significantly increased by using multiple central processing unit (CPU) cores, or even graphical processing unit (GPU) cores, which typically offer faster computation than CPUs for a parallelised calculation. Furthermore, Fourier transform algorithms are implemented in most high-level programming languages, e.g. MATLAB or Python, making them easy to use.

The Fourier transform method works by considering light as being composed of a superposition of planar wavefronts, which are considered to originate from the natural modes of the propagation medium, instead of originating from identifiable sources [77].

The typical implementation of a Fourier transform is a FFT. The FFT algorithm divides up each distinct frequency component into a signal including amplitude and phase by factorising the discrete Fourier transform into a product of multiple matrices which are primarily composed of zeros. These zeros do not need to be computed, which means that for the popular Radix-2 Cooley-Tukey FFT algorithm [77], the computation time scales as $N_x N_y \times (log_2(N_x) + log_2(N_y))$. Here, N_x and N_y are the resolutions in the x and y axes respectively, and the hologram and the holographic image have the same resolution. FFTs are usually computed fastest when their resolution is a power of two, e.g. 2^N [77]. When a different resolution is chosen, the hologram/holographic image should be padded with zeros to the resolution of the next power of 2. Therefore, the scaling of a FFT can be worse than detailed above if the resolution needs to be padded out into a larger matrix to compute [76, 77]. In the case of a non-flat HMS substrate topography, the planar wave assumptions made for FFTs do not hold. Instead, the HMS surface can be considered as the combination of many flat surfaces, each of which can be propagated using a FFT and then summed to create the holographic image. This method requires many FFTs, however, which reduces the computation speed. For a surface curved along one axis, where $N_x = N_y = 2000$ for example, 2000 separate FFTs may be required.

Numerical integration

Numerical integration approaches (e.g. equations 2.9, 2.10, and 2.11) are not pre-optimised thus need to be programmed. These approaches consider each coordinate in plane O as a single isotropic Huygens' source. Once these points are propagated (using numerical integration) to plane I they can be summed to find the combined complex wave in this plane [73], which is described in figure 2.6(a). Here, the resolution of the O and I planes are defined as $N_x \times N_y$, and $M_x \times M_y$ respectively.

The most straightforward implementation of this numerical integration is detailed in pseudocode in algorithm 2. First, an empty array is created for the holographic image. Next, four nested for loops propagate light from every pixel in the O plane to every pixel in the I plane. At the end of each iteration, the light calculated from the numerical integral in the I plane, $U'_I(\mathbf{r})$, is summed with the light in the holographic image plane, $U_I(\mathbf{r})$. Once all the iterations are completed, $U_I(\mathbf{r})$ can be output. In figure 2, the integer variables n_x, n_y, m_x, and m_y correspond to the indexes of sources as shown in figure 2.6. The subscripts n and m refer to the O and I planes respectively.

Algorithm 2 Single threaded numerical integration

```
$U_I(\mathbf{r}) = 0$
Iterate over $n_x$ in the $range(0, N_x)$
    Iterate over $n_y$ in the $range(0, N_y)$
        Iterate over $m_x$ in the $range(0, M_x)$
            Iterate over $m_y$ in the $range(0, M_y)$
                Calculate $U'_I(\mathbf{r})$ from the numerical integral
                $U_I(\mathbf{r}) = U_I(\mathbf{r}) + U'_I(\mathbf{r})$
Return $U_I(\mathbf{r})$
```

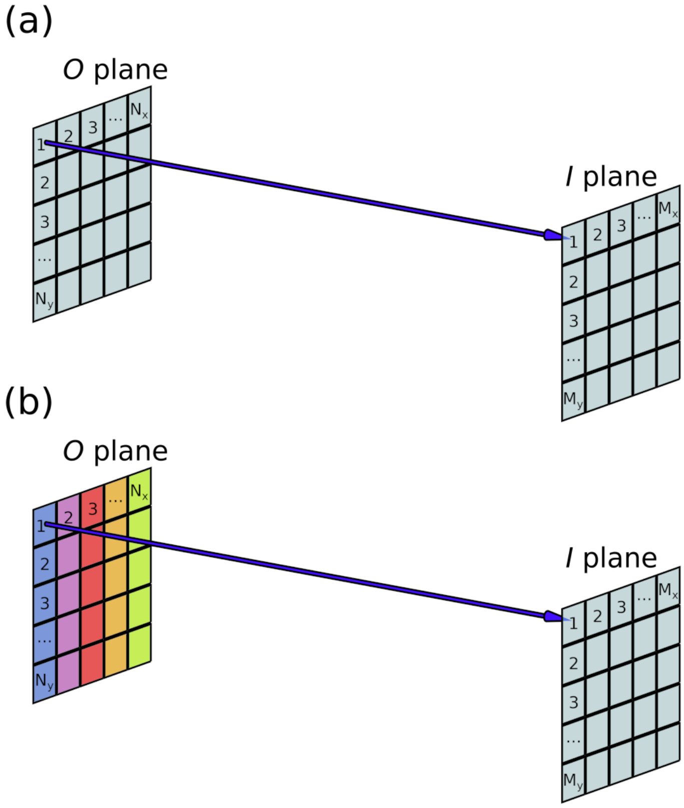

Figure 2.6: Propagation from the *O* plane to the *I* plane with a (a) single-threaded or (b) multi-threaded computation. Each chunk is shown in a different colour.

My implementation of this algorithm was programmed in Python + Numpy as it is free, well supported, and I was familiar with it. For loops in Python are slow and inefficient, and thus act as a bottleneck. To overcome this, the inner two for loops were vectorised to improve the computation speed considerably. More vectorisation was not possible as it was found that vectorising more for loops required an unfeasible amount of memory.

Next, substantial computation speed gains were found by rewriting algorithm 2 to be multi-threaded, which enabled the CPUs to use all of their cores. To do this, plane O is split into separate chunks (which are illustrated in figure 2.6(b) in different colours) with each chunk propagated to plane I by a different CPU core. Within each chunk, the complex waves in plane I are summed to create a $M_x \times M_y$ array. The resultant $M_x \times M_y$ arrays are then summed to create the final $M_x \times M_y$ array, $U_I(\mathbf{r})$.

The final result of this method is identical to the single-threaded algorithm detailed in algorithm 2. Indeed, for a single CPU core, this latter method would be no faster; however, as each chunk can be calculated on a separate CPU core, this calculation is now highly parallelisable. As such, the computation time decreases approximately linearly with increased numbers of CPU cores. Similar to the FFT algorithm, because this algorithm is parallelisable, it could also be performed on GPUs. This was not required for this work but could be investigated in the future. By setting the length of each chunk, this algorithm can also be configured to use less memory than the single-threaded algorithm.

The computation time of this algorithm scales as $M_x M_y N_x N_y$. This is considerably worse than the scaling of the FFT algorithm, which goes as $N_x N_y \times (log_2(N_x) + log_2(N_y))$. For this reason, even with the vectorisation and parallelisation methods, for large planes with many pixels the RS propagation algorithm is slower to compute.

Fortunately, there are additional avenues to improve the computation time of the RS propagation algorithm. First, holograms could be designed with a high-resolution ($N_x \times N_y$), but with a lower holographic image resolution ($M_x \times M_y$). Second, when performing a propagation, any Huygens' source in plane O with an intensity of 0 can be ignored as these sources do not contribute to the holographic image. Third, if either of the O or I planes are non-square, this algorithm allows only the relevant areas to be computed, whereas a FFT based approach requires the computation of a larger square area.

A further method to improve the speed of the GSA (which was not implemented for simplicity) is first to check if the pixel in the I plane has an intensity of 0 for the propagation back. These pixels do not contribute to the hologram and so can also be ignored.

In conclusion, numerical integration is slower than a simple FFT. Numerical integration speed, however, can be increased with smart choices for the propagation parameters. As a result, the time to recover the holograms in this thesis was generally within 10 minutes for numerical integration, and 1 minute for FFTs. Furthermore, numerical integration allows for far greater flexibility, and allows for hologram designs for particular wavelengths, hologram or holographic image pixel pitches, and surface topologies. As this thesis describes, these hologram designs enable new phenomena and out-of-the-lab applications for HMSs.

2.4 Systematic sweep of the hologram parameters

The following section presents a systematic investigation of the most critical hologram parameters for the RS light propagation algorithm.

2.4.1 Number of quantised phase angles

To fabricate the HMSs, the phase values are quantised into evenly spaced increments in the range $0 \rightarrow 2\pi$. Quantising is a necessary step to reduce the number of different meta-atom designs needed, or to reduce the coupling between adjacent nanorods [11, 78]. Quantisation also simplifies the design of the RS light propagation algorithm. To test the effect of quantisation on the resultant holographic images, the parameters in table 2.1 were used to generate a hologram with the GSA.

Table 2.1: **Phase angle quantisation hologram parameters**

Parameter	Value
Hologram pixels	300×300
Holographic image pixels	350×350
Hologram pixel pitch	300 nm
Holographic image pixel pitch	0.3 mm
Holographic image offset in x, y, z	0.0, 0.0, 0.1 m
Wavelength	630 nm

The resultant holographic images with different levels of quantisation (no quantisation, twelve levels, six levels, four levels, three levels, and two levels) are displayed in figure 2.7.

Here, one sees that increasing the quantisation increment decreases the contrast of the holographic image. However, this effect is small until the quantisation increment is greater than 60 degrees, similar to the effect of quantisation in multi-level Fresnel lenses [79, 80]. With a 180 degree quantisation, there is severe degradation in the holographic image, which is superimposed (upside down) on itself. This informs that keeping the quantisation increment below 60 degrees should limit the degradation in the holographic image quality.

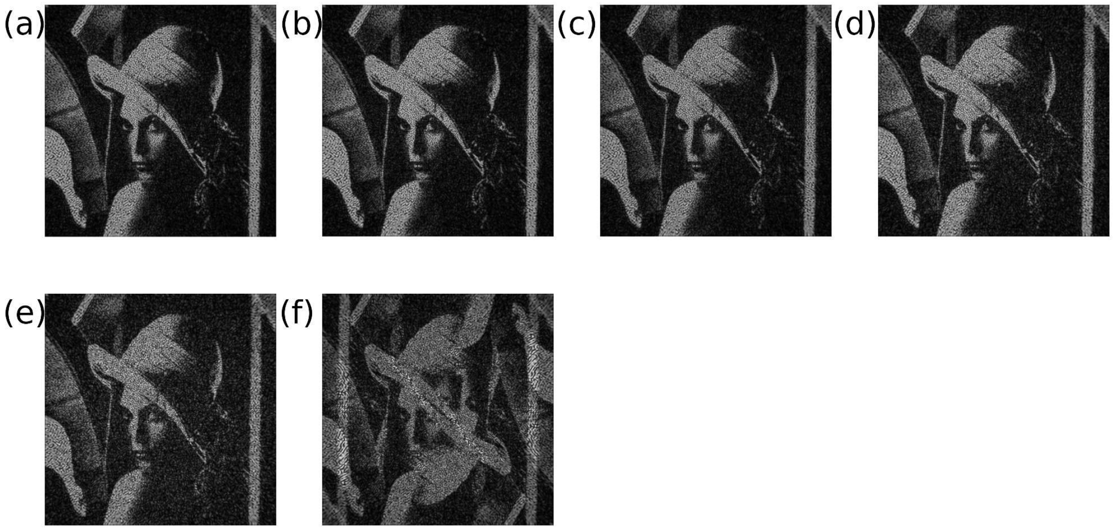

Figure 2.7: Holographic images where the phase was quantised in increments of (a) no quantisation i.e. float64 (b) 30 degrees (c) 60 degrees (d) 90 degrees (e) 120 degrees (f) 180 degrees.

2.4.2 Wavelength

To test the response to λ, two tests were run. In the first, the hologram generated by the parameters in table 2.1 was propagated to the holographic image plane, while varying the wavelength. To view the entire holographic image, the pitch of the holographic image plane was altered to 0.45 mm for these simulations, which are displayed in figure 2.8.

Here, figure 2.8 displays that increasing the wavelength, keeping the other parameters identical, increases the physical size of the holographic image.

The second test was to see how the holographic image responds to illumination by a source with a broader bandwidth. The central wavelength was set at 630 nm, and the broadband illumination was modelled as multiple plane-wave illumination sources, each 5 nm apart with identical phase and amplitude (a frequency comb with constant amplitude). Each complex wave was then propagated to the holographic image plane and summed with the results displayed in figure 2.9. As in the previous test, the pitch of the holographic image was set to 0.45 mm.

Figure 2.9 shows that increasing the wavelength range blurs out the holographic image. Fur-

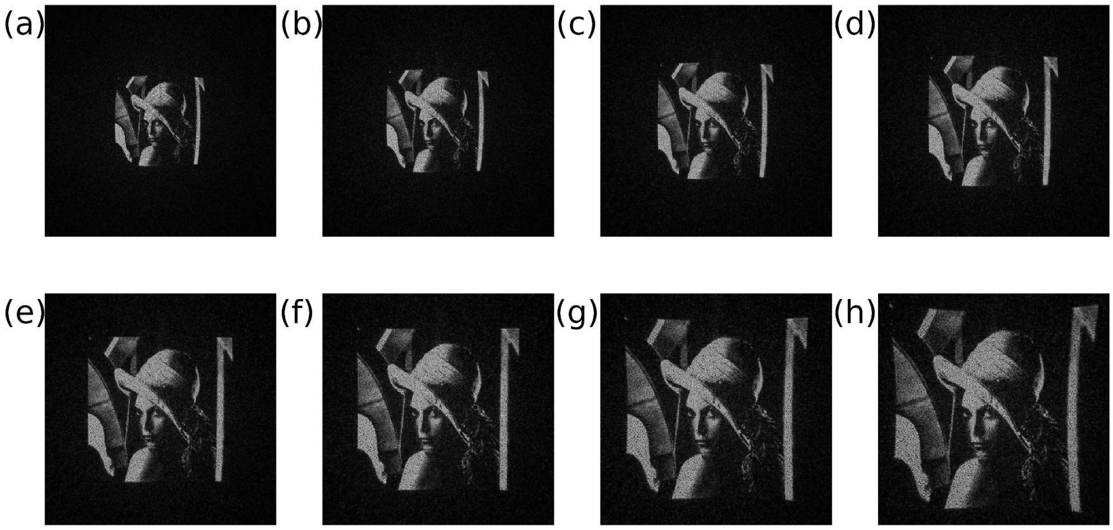

Figure 2.8: Resulting holographic images where the illumination source has a wavelength λ = (a) 400 nm (b) 450 nm (c) 500 nm (d) 550 nm (e) 600 nm (f) 650 nm (g) 700 nm (h) 750 nm.

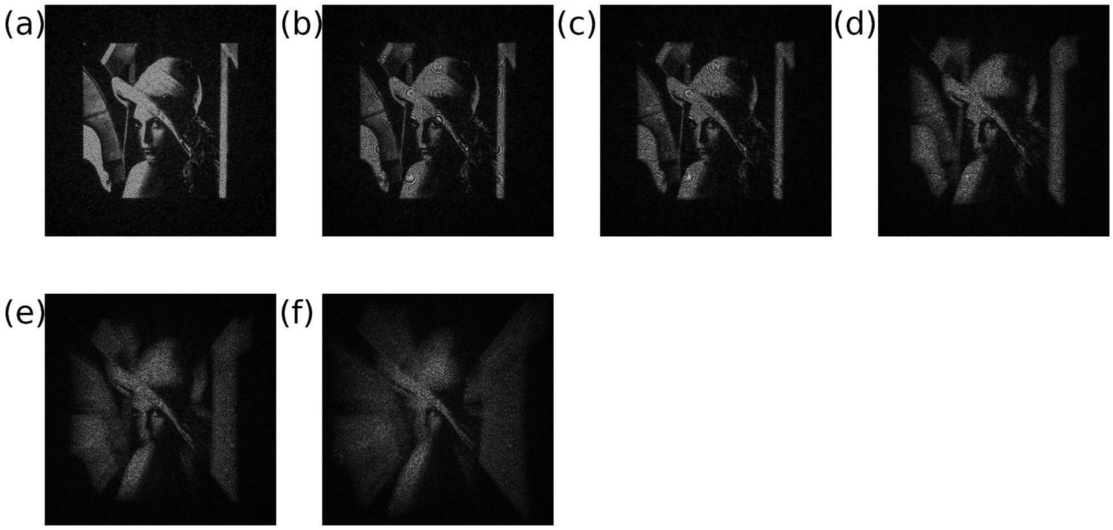

Figure 2.9: Resulting holographic images where the illumination source frequency comb has a range of (a) 0 nm (b) 10 nm (c) 20 nm (d) 80 nm (e) 160 nm (f) 320 nm.

thermore, this blur follows radial lines from the zeroth order of the illumination (the centre of the hologram). Each wavelength creates the holographic image with a different size, centred on the zeroth order, because the HMS operates as a dispersive element. This effect is seen to be small until the wavelength range is broader than ≈ 20 nm. Once the wavelength range is broader than 160 nm, the holographic image is severely degraded. Figures 2.9(a) and 2.9(b) contain larger diffraction spots, similar to Airy spots, because of the interference between the multiple wavelengths. This effect results from the limited number of discrete wavelength sources used and would not exist for a realistic continuous source.

This informs that keeping the illumination wavelength range below 20 nm should limit the degradation of the holographic image quality. Additionally, this gives insight into how incoherent light could spoil a holographic image, which is expanded on in chapter 7.

2.4.3 Hologram pixel pitch

The pixel pitch is an essential parameter for the function of holograms as it controls the coupling between adjacent meta-atoms and is one of the factors determining the HMS efficiency. To test how the pixel pitch affects the holographic image, the hologram generated by the parameters in table 2.1 was propagated to the holographic image plane, varying the hologram pixel pitch. The pitch of the holographic image plane was set as 0.3 mm for these simulations with the results displayed in figure 2.10.

Here, figure 2.10 displays that increasing the pixel pitch decreases the physical size of the holographic image. This effect is analogous to how increasing the NA of a device decreases the physical size of a diffraction pattern.

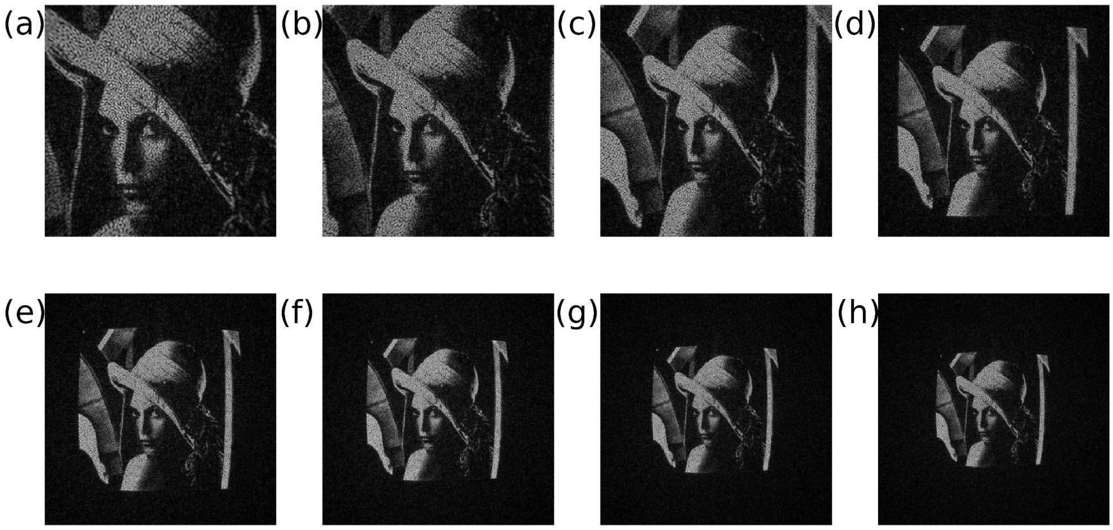

Figure 2.10: Resulting holographic images where the hologram pixel pitch is (a) 200 nm (b) 250 nm (c) 300 nm (d) 350 nm (e) 400 nm (f) 450 nm (g) 500 nm (h) 550 nm.

2.4.4 Gaussian beam size

Another parameter of interest is the uniformity of the illuminating source. Commonly, the illumination is not a plane wave and instead has a Gaussian intensity profile. To test how the uniformity of the source illumination affects the holographic image, the hologram generated by the parameters in table 2.1 was propagated the holographic image plane, while varying the full width half maxima (FWHM) of the source illumination. The pitch of the holographic image plane was kept as 0.3 mm for these simulations, and the results are displayed in figure 2.11.

Figure 2.11 shows that the holographic image is resilient to the exact FWHM of the beam until it is below the width of the hologram. This informs that the FWHM of the illumination source should excite as much of the hologram as possible, but that some dissimilarity in the source intensity can be tolerated.

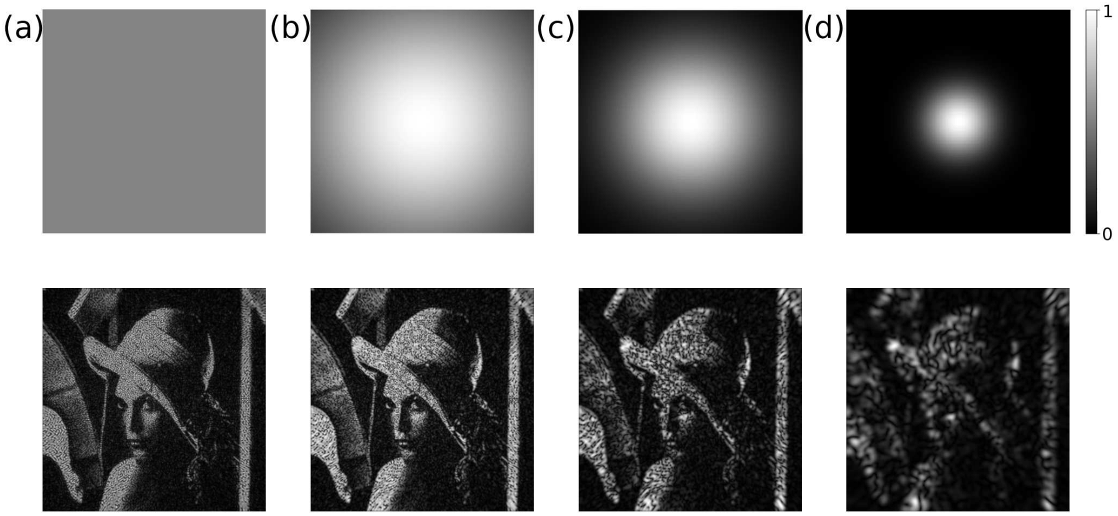

Figure 2.11: Resulting holographic images where the source illumination has an intensity of a (a) plane wavefront, or a Gaussian wavefront with FWHM = (b) 90 μm (c) 28 μm (d) 6 μm.

2.4.5 Hologram to holographic image distance

Holograms can be designed to produce a holographic image at any distance from the hologram. Here, it is explored how the resulting holographic image appears as a function of distance from the hologram. In particular, the holographic image evolution of holograms designed for the far-field and near-field was compared.

Far-field holography, where the holographic image is designed at a significant distance from the hologram, is the standard approach and has been well studied [11, 33, 78, 72].

There has also been work in expanding the uses of HMSs by exploiting phenomena in the near-field. One such example is encoding a three-dimensional image in a two-dimensional HMS [10, 43]. Another example is encoding tunability either to vary the focal length of a FHMS lens [49], or to switch between multiple images in the near-field [50].

To create a holographic image, Huygens' sources from the hologram interfere. However, once the Huygens' sources have propagated sufficiently, this holographic image wavefront does not change substantially with further propagation from the HMS [11].

The parameters used to generate the far-field hologram with the GSA are displayed in table 2.2.

Table 2.2: **Far-field hologram parameters**

Parameter	Value
Hologram pixels	1000 × 1000
Holographic image pixels	350 × 350
Hologram pixel pitch	300 nm
Holographic image pixel pitch	0.66 mm
Holographic image offset in x, y, z	0.0, 0.0, 0.1 m
Wavelength	630 nm

The recovered hologram was propagated to holographic image planes with the following distances between them: 0.1 μm, 1 μm, 10 μm, 0.1 mm, 1 mm, 10 mm, 0.1 m, and 1 m. The holographic image pixel pitches were scaled in the same ratio as: 0.6666 nm, 6.666 nm, 66.66 nm, 0.6666 μm, 6.666 μm, 66.66 μm, 0.6666 mm, and 6.666 mm respectively. The holographic image results are displayed in figure 2.12.

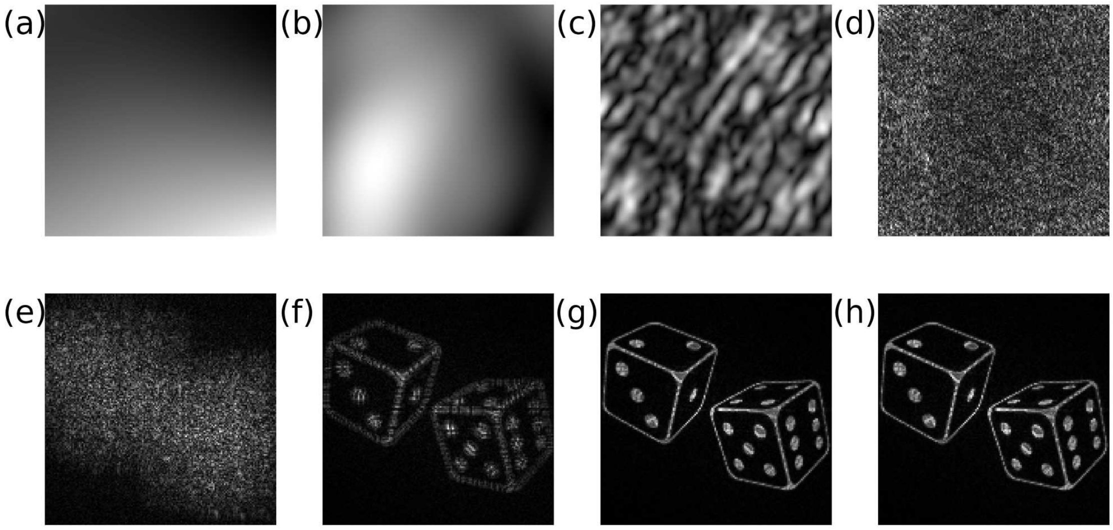

Figure 2.12: A holographic image designed to be imaged 0.1 m from the hologram, but viewed in multiple planes with different hologram to holographic image distances where $z =$ (a) 0.1 μm (b) 1 μm (c) 10 μm (d) 0.1 mm (e) 1 mm (f) 10 mm (g) 0.1 m (h) 1 m.

To compare the evolution of the holographic image wavefront for far-field and near-field holograms, a hologram designed for a 0.1 mm separation from the holographic image was recovered using the GSA and the parameters in table 2.3.

The recovered hologram was then propagated to the same holographic image planes, e.g. the

Table 2.3: **Near-field hologram parameters**

Parameter	Value
Hologram pixels	1000×1000
Holographic image pixels	350×350
Hologram pixel pitch	300 nm
Holographic image pixel pitch	0.66 μm
Holographic image offset in x, y, z	0.0, 0.0, 0.1 mm
Wavelength	630 nm

same distance from the hologram and the same pitch. The results are displayed in figure 2.13.

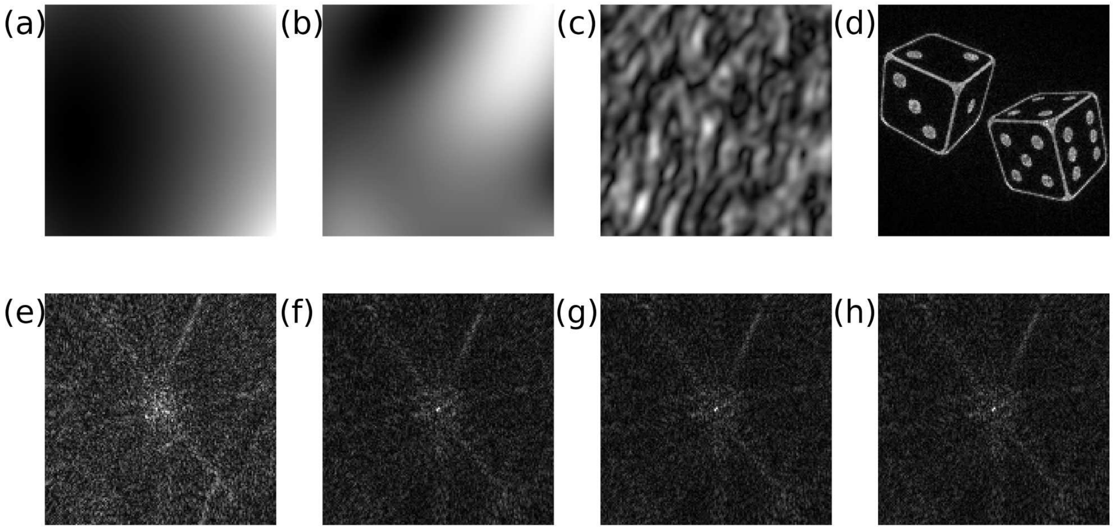

Figure 2.13: A holographic image designed to be imaged 0.1 mm from the hologram, but viewed in multiple planes with different hologram to holographic image distances where $z =$ (a) 0.1 μm (b) 1 μm (c) 10 μm (d) 0.1 mm (e) 1 mm (f) 10 mm (g) 0.1 m (h) 1 m.

As one can see from figures 2.12 and 2.13, the holographic image can be designed for arbitrary distances from the hologram. In both cases, after the wavefront has propagated more than 10 mm the wavefront stops evolving and instead enlarges with increased propagation distance. Once the hologram of figure 2.12 has propagated 10 mm, the Holographic image remains legible for increased distances.

2.5 Pancharatnam-Berry phase-shift

This section describes the theory behind realising DH in an experiment with HMSs. These HMSs require a method to point-by-point define the amplitude, phase, or both. Throughout this thesis, phase-only holograms were used as their efficiency is higher than amplitude-only holograms, and their fabrication/simulation is more straightforward than full-holograms.

With the exception of chapter 6, the holograms in this thesis were defined using Pancharatnam-Berry (PB) phase-shifting. This technique, as shown in figure 2.14, uses the geometry of a meta-atom, in this case, the orientation of a nanorod, to encode a particular PB phase-shift for incident circularly polarised light, e.g. right-handed circularly polarised (RCP) or left-handed circularly polarised (LCP). This PB phase-shift can be set point-by-point across the HMS to encode the hologram.

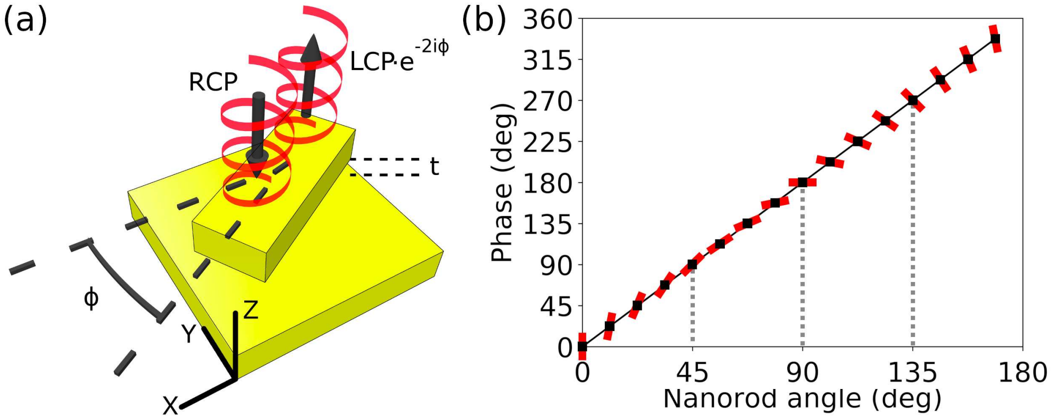

Figure 2.14: (a) A diagram of the unit cell structure of a nanorod with incident RCP light. The spacing between the nanorod and backplane is denoted as t. The angle ϕ belongs to the xy plane and is defined between the long axis of the nanorod and x axis [78]. (b) The angle of the nanorod vs the resultant phase-shift. The nanorod is shown in red.

The circularly polarised light can be represented as points on a Poincaré sphere, as shown in figure 2.15, where only the polarisation states on the surface of the sphere are valid. During a PB phase-shift, the cyclic path taken around the Poincaré sphere changes the polarisation state before returning it to its original polarisation state. This action does, however, have an associated non-zero phase-shift, which is equal to half of the enclosed area swept out by the cyclic path [81, 82]. The PB phase-shift is further described below.

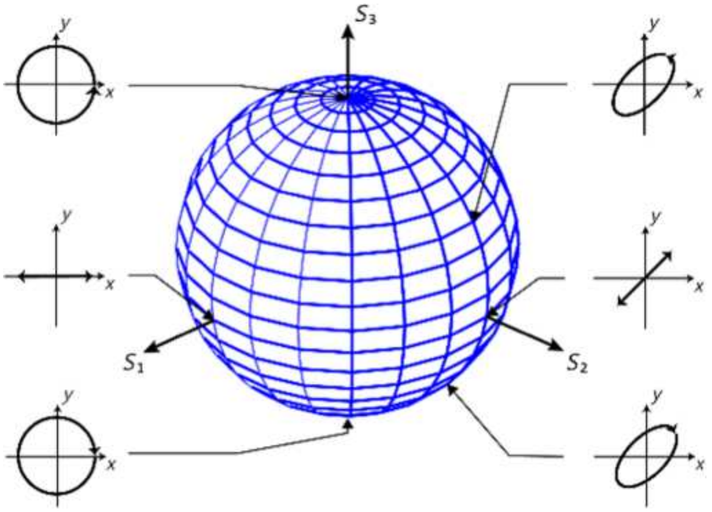

Figure 2.15: The north and south poles define LCP and RCP respectively. Points on the equator define linearly polarised light (x and y polarisations are opposite) and all other points define elliptically polarised light [83].

If a light source with a circular polarisation (e.g. RCP or LCP) is incident on the meta-atom, the incident LCP/RCP electric fields can be represented respectively as

$$\mathbf{E}_{incident} = \frac{1}{\sqrt{2}}\left(1\hat{x} \pm i\hat{y}\right). \tag{2.25}$$

This incident field creates plasmons, which are restricted to only oscillate along the long axis of the nanorod as the short axis is too confined [20, 84]. These nanorod dimensions can be tailored so that the plasmonic resonances are π out of phase with one another. Therefore, the angle of the nanorod, ϕ, as defined in figure 2.14, dictates the coupling of $\mathbf{E}_{incident}$ into the nanorod. This can be found using the projection of $\mathbf{E}_{incident}$ onto the angle of the nanorod, and can be written as

$$\begin{aligned} \frac{1}{\sqrt{2}}\left(1\hat{x} \pm i\hat{y}\right) \cdot \left(\cos(\phi)\hat{x} + \sin(\phi)\hat{y}\right) &= \frac{1}{\sqrt{2}}\left(\cos(\phi) \pm i\sin(\phi)\right) \\ &= \frac{1}{\sqrt{2}}\exp(\pm i\phi). \end{aligned} \tag{2.26}$$

Because the electric field must couple both in then out of the nanorod, the phase-shift is thus given by $\left(\frac{1}{\sqrt{2}}\exp(\pm i\phi)\right)^2$ as

$$\phi_{phase-shift} = \pm 2\phi. \tag{2.27}$$

Consequently, the nanorod acts as a half-waveplate and controls the phase-shift of incident light with the angle of its orientation. As such, changing the orientation of the nanorod imparts a phase-shift equal to twice the angle of the nanorod, and flips the polarisation, e.g. to LCP, as defined in figure 2.14 [65]. Furthermore, this phase-shift is equal and opposite for RCP and LCP incident light. This result can be derived from the Jones vector formalism and is a standard result for half-waveplates.

The specific visible light meta-atom implementation used in this thesis comprises three layers, a nanopatterned surface (a periodic array of nanorods), a dielectric spacer, and a reflective backplane. This scheme is illustrated in figure 2.14(a). This meta-atom operates in reflection and because it uses PB phase-shifting it is broadband and broad angle. Furthermore, the three-layers act as a Fabry-Perot cavity to boost the phase conversion efficiency, and reduce the dispersion typical of a single HMS layer. Using this approach, other researchers have achieved efficiencies of 60-80% [11, 33].

The nanorod array in our design is quantised into 16 discrete nanorod angles, 22.5 degrees apart, to limit cross-talk between adjacent nanorods while avoiding the under-sampling investigated in the systematic sweep of the hologram parameters (detailed above).

To choose the pitch of the nanorod spacing the following equation was used, which creates a holographic image with a projection range of 95 degrees at $\lambda = 650$ nm:

$$\Delta P = \frac{m_i \lambda}{M_i \times 2\tan\left(\frac{\alpha_i}{2}\right)}, \tag{2.28}$$

where ΔP is the nanorod spacing, m_i and M_i are the number of pixels in the holographic image plane and in the HMS respectively, α_i is the projection range of the holographic image, and $i = x, y$ as detailed in [33]. The nanorod pitch must be small enough to satisfy the Nyquist-Shannon sampling theorem for a continuous phase profile [85] while keeping the distances large enough to minimise cross-talk between the nanorods.

2.6 Conclusion

Here, the methods used to iteratively recover phase distributions using the GSA and an implementation of the RS algorithm have been detailed. These tools are used extensively throughout the following chapters. Furthermore, the PB phase-shift has been described, which is the phenomena behind most of the HMSs in this thesis.

2.7 Contribution

I developed the algorithm to propagate light between the hologram and holographic image planes and ran all of the simulations. Our collaborators at Heriot-Watt designed the nanorod meta-atom.

Chapter 3

Fabrication

This chapter outlines the fabrication procedures used in this thesis, in particular, to create both rigid and flexible HMSs in the visible and millimetre wavelength ranges. These methods enabled the creation of membranes with cm^2 sizes and thicknesses of hundreds of nanometers with a yield rate, excluding human error, approaching 100%. In the interest of readability, information on the materials and the fabrication procedures has been placed into appendix B.

3.1 Nanorod metasurfaces for visible holography

To fabricate the visible range FHMSs, the procedures sketched in figure 3.1 and outlined in detail below were followed. These procedures took around three days per sample, which was also similar to the fabrication time for the c-ring antennas. The time per sample could be decreased, however, by processing multiple samples simultaneously.

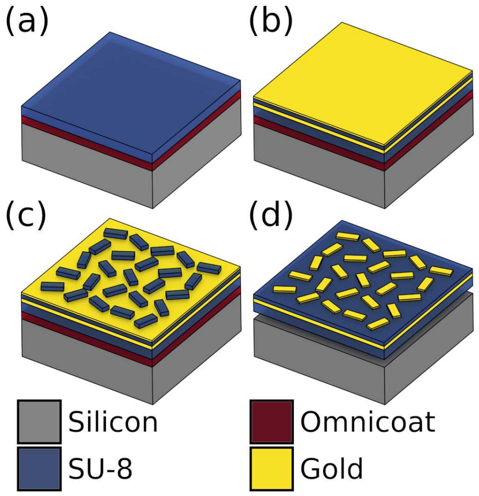

Figure 3.1: Schematic of the fabrication process for the FHMSs. (a) A silicon carrier was initially coated with an Omnicoat layer and a thick SU-8 film by spin-coating. (b) A gold film was evaporated onto the SU-8 film as a reflective backplane. After that, a spacing layer of SU-8 was spun onto the gold film followed by a second gold film that was deposited onto the SU-8. (c) A resist layer of SU-8 was spun onto the final gold layer for the standard EBL process. Nanorods were defined after the development process and then used as the etching mask. (d) Gold nanorods on the top of the sample were obtained after a RIE step. The Omnicoat layer was then dissolved to leave a free-floating flexible hologram.

Fabrication procedure

1. Cleaned the silicon carrier by submerging it in acetone and then isopropyl alcohol (IPA) under sonication. Each cleaning step was performed at room temperature for 5 minutes.
2. Spin-coated a sacrificial layer of Omnicoat (Microchem) at 1000 rpm for 1 minute.
3. Baked for 1 minute at 230 °C.
4. Spin-coated a thick layer of SU-8 (Microchem) to act as a flexible carrier, this was a blend of SU-8 2050 and SU-8 2000.5 mixed 1:1, at 5000 rpm for 1 minute. The thickness of this layer was $2.6 \pm 0.1\ \mu$m. This thickness was chosen to guarantee both high flexibility, and robustness of the FHMS.
5. Baked for 1 minute at 60 °C, then 4 minutes at 90 °C.
6. UV-exposed the SU-8 layer, to cross-link it, for 5 minutes.

7. Baked, to finalise cross-linking in the SU-8, for 5 minutes at 100 °C.

8. Evaporated 100 nm of gold onto the SU-8 to act as a reflective backplane. This layer was thick enough to efficiently reflect the light without sacrificing flexibility. The typical evaporation parameters are shown in table 3.1.

Table 3.1: **Typical evaporation parameters**

Parameter	Value
Base Pressure	1e-6 mPa
Evaporation pressure	1e-5 mPa
Evaporation rate	0.1 nm s^{-1}

9. Spin-coated a thin layer of SU-8 to act as a dielectric spacer, this was a blend of SU-8 2000.5 and Cyclopentanone mixed 1:3 (Microchem), at 5000 rpm for 1 minute. The thickness of this layer was 90 nm. This thickness was chosen as approximately $\lambda/4$. The optical dispersion properties of this film were characterised via a standard retrieval method [86], which gave a refractive index of 1.67 at $\lambda = 600$ nm. The variation in the refractive index was less than 1.5% in the wavelength range 570-850 nm.

10. Baked for 1 minute at 60 °C, then 4 minutes at 90 °C.

11. UV-exposed the SU-8 layer, to cross-link it, for 5 minutes.

12. Baked, to finalise cross-linking in the SU-8, for 5 minutes at 100 °C.

13. Evaporated 40 nm of gold onto the SU-8 to become the nanorod antennas.

14. Spin-coated a thin layer of SU-8 to act as the EBL resist, this was a blend of SU-8 2000.5 and Cyclopentanone mixed 1:2, at 5000 rpm for 1 minute. The thickness of this layer was 100 nm. This thickness was chosen to be enough to act as an effective mask but with the minimal limiting of the EBL resolution.

15. Baked for 1 minute at 60 °C, then 4 minutes at 90 °C.

16. EBL step using a RAITH eLine Plus and the parameters in table 3.2.

Table 3.2: **Typical electron beam parameters for nanorod meta-atoms**

Parameter	Value
Extra high tension (EHT)	30 V
Base Dose	5 μC cm^{-2}
Dose factor	2
Working distance	10 mm
Write field size	$100 \times 100\ \mu$m^2
Aperture size	7 μm
Basic step size	2 nm
Area step size	20 nm

17. Baked for 2 minutes at 90 °C as a post-exposure bake to cross-link the exposed nanorods.

18. Developed the SU-8 resist with EC solvent for 1 minute at room temperature.

19. Dry RIE step to remove the unwanted gold unprotected by the SU-8 nanorod masks. This step was performed with the parameters in table B.2 for 9 minutes.

20. Baked for 5 minutes at 150 °C to increase the rigidity of the supporting membrane and simplify the release step.

21. Dissolved the Omnicoat layer, to release the membrane from the silicon carrier, using MF319 (Microposit).

22. Transferred the sample into de-ionised (DI) water, and then onto the desired carrier.

An image of the finished FHMS, taken with a standard camera, is presented in figure 3.2.

Additionally, figure 3.3 displays SEM images of the FHMSs taken before and after lift-off (with a standard camera) to assess the impact of lift-off on the nano-features. The quality, in terms of damage to the surface, of the FHMSs are identical. As such, the lift-off process does not damage FHMSs.

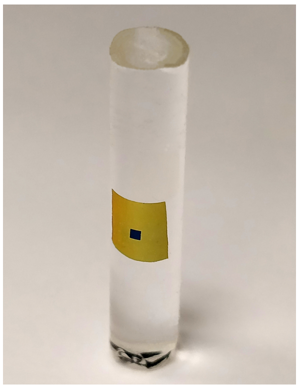

Figure 3.2: An experimental image displaying a FHMS conformed to a non-flat surface. The central patterned area appears darker due to the reduced reflectivity with respect to the surrounding region [72].

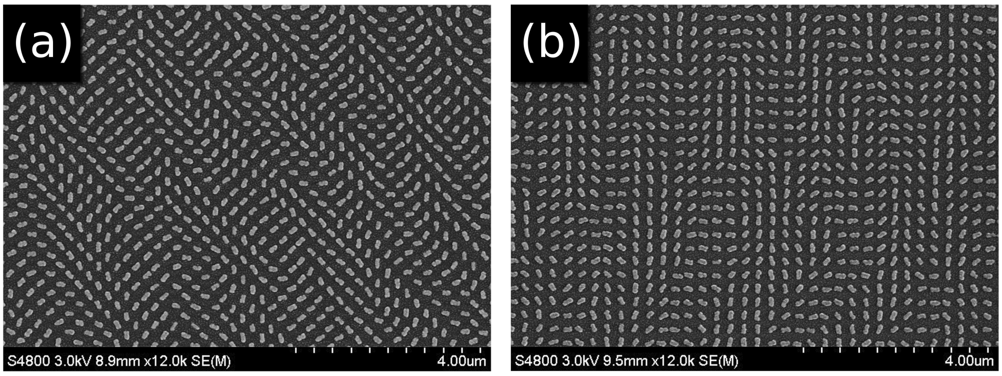

Figure 3.3: An SEM image of typical areas of the FHMS taken (a) before lift-off (b) after lift-off [78].

3.2 C-ring resonator metasurfaces for millimetre holography

3.2.1 Rigid implementation

To fabricate the millimetre wavelength range rigid HMSs, the procedures sketched in figure 3.4 and outlined in detail below were followed.

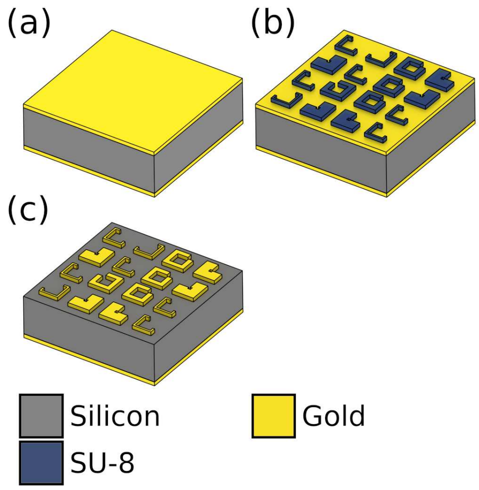

Figure 3.4: Schematic of the fabrication process for the HMSs. (a) A silicon carrier was coated with gold on both sides via evaporation. (b) A resist layer of SU-8 was spun onto the upper gold layer for the standard EBL process. The meta-atoms were defined after the development process. (c) The meta-atoms on the top of the sample were obtained after a RIE step.

Fabrication procedure

1. Cleaned the 115 μm thick low-loss silicon dielectric spacer by submerging it in acetone and then IPA under sonication. Each cleaning step was performed at room temperature for 5 minutes.
2. Evaporated 200 nm of gold onto the back of the silicon to act as a reflective backplane. This layer was thick enough to efficiently reflect the light without wasting too much gold.
3. Evaporated 200 nm of gold onto the front of the silicon to become the c-ring meta-atoms. This layer was thick enough to scatter the light without wasting too much gold.
4. Spin-coated a thin layer of SU-8 to act as the EBL resist, this was SU-8 2000.5 at 3000 rpm for 1 minute. The thickness of this layer was 500 nm. This thickness was chosen to be enough to act as an effective mask but with the minimal limiting of the EBL resolution.
5. Baked for 1 minute at 60 °C, then 4 minutes at 90 °C.
6. EBL step using a RAITH eLine Plus and the parameters in table 3.3.
7. Baked for 2 minutes at 90 °C as a post-exposure bake to cross-link the exposed c-rings.

Table 3.3: **Typical electron beam parameters for millimetre meta-atoms**

Parameter	Value
EHT	30 V
Base Dose	5 μC cm^{-2}
Dose factor	0.4
Working distance	10 mm
Write field size	100 × 100 μm^2
Aperture size	30 μm
Basic step size	2 nm
Area step size	0.5 μm

8. Developed the SU-8 resist with EC solvent for 1 minute at room temperature.

9. Dry RIE step to remove the unwanted gold unprotected by the SU-8 c-ring masks. This step was performed with the parameters in table B.2 for 42 minutes.

3.2.2 Flexible implementation

To fabricate the millimetre wavelength range FHMSs, the procedures sketched in figure 3.5 and outlined in detail below were followed.

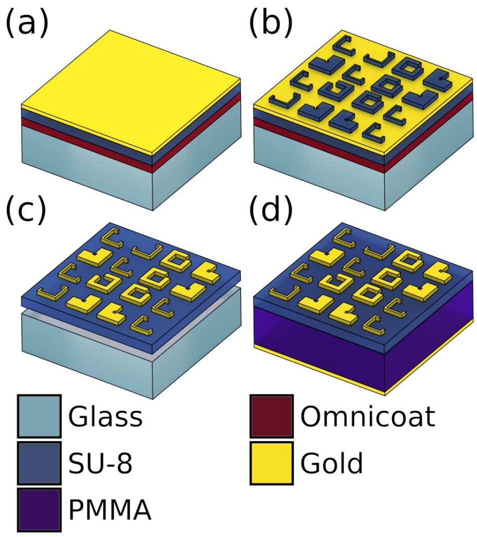

Figure 3.5: Schematic of the fabrication process for the FHMSs. (a) A glass carrier was coated with a lift-off then polymer membrane layer. This was topped with gold via evaporation. (b) A resist layer of SU-8 was spun onto the upper gold layer for the standard EBL process. The meta-atoms were defined after the development process and then used as the etching mask. (c) The meta-atoms on the top of the sample were then obtained after a RIE step. The lift-off layer was dissolved to detach the membrane from the glass carrier. (d) This part of the sample was combined with a polymer membrane, where the polymer membrane was coated in gold via evaporation.

Fabrication procedure

1. Cleaned a poly(methyl methacrylate) (PMMA) film by submerging it in IPA under sonication. This cleaning step was performed at room temperature for 5 minutes. The thickness of this layer was 400 μm. This thickness was chosen as approximately $\lambda/4$.
2. Evaporated 200 nm of gold onto the back of the PMMA to act as a reflective backplane. This layer was thick enough to efficiently reflect the light without wasting too much gold. This part of the fabrication was now complete.
3. Cleaned a glass carrier by submerging it in acetone and then IPA under sonication. Each cleaning step was performed at room temperature for 5 minutes.
4. Spin-coated a sacrificial layer of Omnicoat at 1000 rpm for 1 minute
5. Baked for 1 minute at 230 °C.

6. Spin-coated a thick layer of SU-8 to act as a flexible carrier, this was a blend of SU-8 2050 and SU-8 2000.5 mixed 1:1, at 1000 rpm for 1 minute. The thickness of this layer was 6.7 μm. This thickness was chosen to guarantee both high flexibility, and robustness of the FHMS.
7. Baked for 1 minute at 60 °C, then 4 minutes at 90 °C.
8. UV-exposed the SU-8 layer, to cross-link it, for 5 minutes.
9. Baked, to finalise cross-linking in the SU-8, for 5 minutes at 100 °C.
10. Evaporated 200 nm of gold onto the SU-8 to become the c-ring antennas.
11. Spin-coated a thin layer of SU-8 to act as the EBL resist, this was SU-8 2000.5 at 3000 rpm for 1 minute. The thickness of this layer was 500 nm. This thickness was chosen to be enough to act as an effective mask but with the minimal limiting of the EBL resolution.
12. Baked for 1 minute at 60 °C, then 4 minutes at 90 °C.
13. EBL step using a RAITH eLine Plus and the parameters in table 3.3.
14. Baked for 2 minutes at 90 °C as a post-exposure bake to cross-link the exposed c-rings.
15. Developed the SU-8 resist with EC solvent for 1 minute at room temperature.
16. Dry RIE step to remove the unwanted gold unprotected by the SU-8 c-ring masks. This step was performed with the parameters in table B.2 for 42 minutes.
17. Baked for 5 minutes at 150 °C to increase the rigidity of the supporting membrane and simplify the release step.
18. Dissolved the Omnicoat layer, to release the membrane from the silicon carrier, using MF319 (Microposit). This part of the fabrication was now complete.
19. The two structures were then combined with the SU-8 supporting membrane placed in direct contact with the PMMA layer.

3.3 Conclusion

This chapter, details the relevant fabrication procedures used in this thesis. Furthermore, because the processes use discrete modular steps, these methods could be incrementally improved, or the materials could be easily swapped if required.

The primary rate-limiting step for scaling up production was the EBL time. In theory, using nanoimprint, or deep UV with roll-to-roll printing could solve this issue. In general, automation could streamline the methods used in this thesis. The yields were already approaching 100%.

3.4 Contribution

I created all of the samples and altered most of the processes to suit my needs from similar processes used in the Synthetic Optics research group, e.g. I changed the: spin speeds, resist blends, exposure and baking times, and the EBL parameters. In total, I made approximately fifty nanorod samples and ten c-ring samples.

Chapter 4

Conformable and surface topography specific metasurface holograms

This chapter first details a platform for FHMSs, and then how it was used to create FHMSs designed for non-flat surface topologies. The motivation for this work was to extend the applications of HMSs through making them flexible, as outlined in chapter 1. The characterisation of these FHMSs, in simulation and experiment, is also described, and the novel phenomena that arise with non-flat FHMSs.

4.1 Flat hologram design

The FHMS were designed for flat surface topologies using the standard two-dimensional FFT light propagator and the GSA.

A FFT creates a spherical far-field holographic image [87, 88]. However, in the experiment, the holographic images are projected onto a flat screen which, without pre-compensation, would result in distorted images. As such, the holographic image were pre-compensated by adjusting the target image from figure 4.1(a) to figure 4.1(b) using a standard spheroid filter, similar to that used in popular photo editing software, programmed in MATLAB. The radius of curvature of this filter was chosen to equal that of the far-field at the position of the screen (in this case 100 mm). However, this pre-compensation does lower the resolution at the edges of the image of the target image.

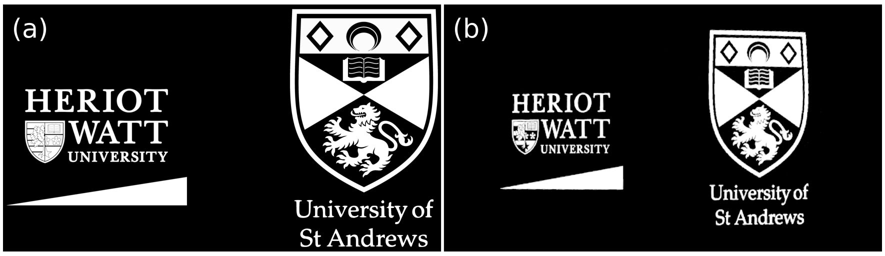

Figure 4.1: The target image (a) without pre-compensation (b) with pre-compensation. The University of St Andrews logo is © University of St Andrews and used with permission. The Heriot-Watt logo is © Heriot-Watt University and used with permission [78].

The resolution of the hologram was set as 1000 × 1000. This hologram was then realised by an array of 1000 × 1000 nanorods with a pitch of 300 nm resulting in a hologram area of 0.3×0.3 mm^2. To reduce the size of diffraction spots in the holographic image, a 2 × 2 periodic array of this retrieved phase profile was constructed. As such, the FHMS had a total area of 0.6×0.6 mm^2.

4.2 Holographic image characterisation

To quantitatively assess the viability of the FHMSs, their efficiency before, and after lift-off from the rigid silicon carrier was characterised. The FHMSs were excited with a SuperK EXTREME supercontinuum laser in the range 570-850 nm, in increments of 20 nm, with the setup sketched in figure 4.2. The bandwidth of the beam was ≈ 10 nm. By passing the laser through a linear polariser followed by a quarter waveplate, a circularly polarised beam was formed. Because the unconverted light remains in the zeroth order, and the image is centrosymmetric, additional polarisers were not needed to view the holographic image after reflection from the sample.

To calculate the optical efficiency of the device, the reflected power on one side of the holographic image was collected by focusing the image with a lens of $f = 25.4$ mm on a Thorlabs S130C Photodiode Power Sensor, as shown in figure 4.2(a). This value was normalised to the incident power, measured by placing the lens and detector directly in front of the quarter waveplate. Since the beam size was larger than the patterned area, the efficiency was scaled by the ratio of the power

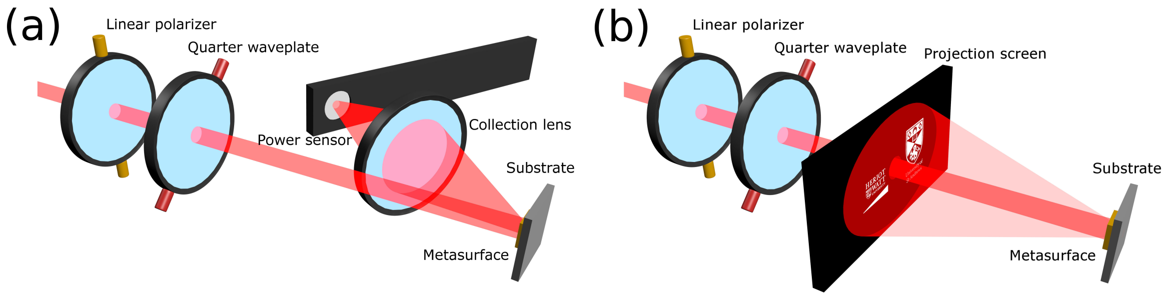

Figure 4.2: Schematics of the optical setups. The helicity of incident light on the FHMS was controlled by the relative angle between the linear polariser and the quarter waveplate. In these images RCP light is shown. (a) Efficiency measurements were made by collecting the light scattered by the FHMS with a $f = 25.4$ mm lens, which was focused onto a Thorlabs S130C Photodiode Power Sensor. (b) Photographs of the holographic images were captured by projecting the light scattered by the FHMS onto a screen [78].

incident on the FHMS and the total incident power. The beam size, as a function of wavelength, was measured using a Thorlabs BC106N-VIS/M CCD beam profiler and the correction factor is shown in figure 4.3.

The total efficiency of the FHMS was calculated considering both sides of the holographic image, which was achieved by doubling the efficiency from one side. The efficiency vs wavelength measurements were made in the range 570-850 nm at normal incidence, and the efficiency vs angle measurements were made at 650 nm.

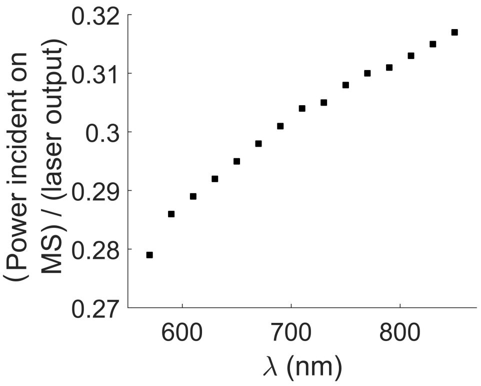

Figure 4.3: Experimental correction factor as function of the wavelength [78].

To photograph the holographic images, the light incident from the FHMS was projected onto a paper screen 100 mm from the FHMS as in figure 4.2(b). The hole in the screen had a diameter of 3 mm.

4.2.1 Wavelength dependence measurements

Figure 4.4 compares the efficiency and the angular robustness of the FHMSs before lift-off, and after lift-off when placed on either a flat silicon carrier or a curved glasses lens. The FHMS conformed to the glasses lens is displayed in figure 4.6. As can be seen in figure 4.4(a), the efficiency of the FHMS decreases roughly linearly with increasing angle. In figure 4.4(b), it is shown that for RCP light, and a 99% dark image, the device peaks in efficiency around 730 nm at 40% before lift-off, 37% after lift-off, and 35% after adhering to the glasses lens. Therefore, neither the lift-off process nor the adhesion to a glasses lens significantly impacts the holographic efficiency. At wavelengths far from 730 nm, the dimensions of the nanorods and the thickness of the spacing layer are not optimised to produce the π phase change and so the efficiency decreases. Furthermore, at shorter wavelengths the interband transitions in gold cause excessive absorption. This reduces the efficiency of the device so that the holographic images cannot be seen much below 570 nm. Despite this limitation, gold was used as the plasmonic material because, unlike silver, it can be back-etched with a RIE step. This was important as RIE defines nanoscale features better than a lift-off procedure on the SU-8 polymer spacing layer. Furthermore, gold is strongly inert which leads to better stability of nano-sized gold features than silver or aluminium. For applications requiring the whole visible range, gold could be interchanged with silver, or aluminium if chlorine is used during the etching [84]. Figure 4.4(c-e) was captured in the visible range, after lift-off, to display the efficiency at different wavelengths, and the centrosymmetric pattern used in the efficiency measurements. This image is distorted because it was not pre-compensated as it was only used for the efficiency measurements.

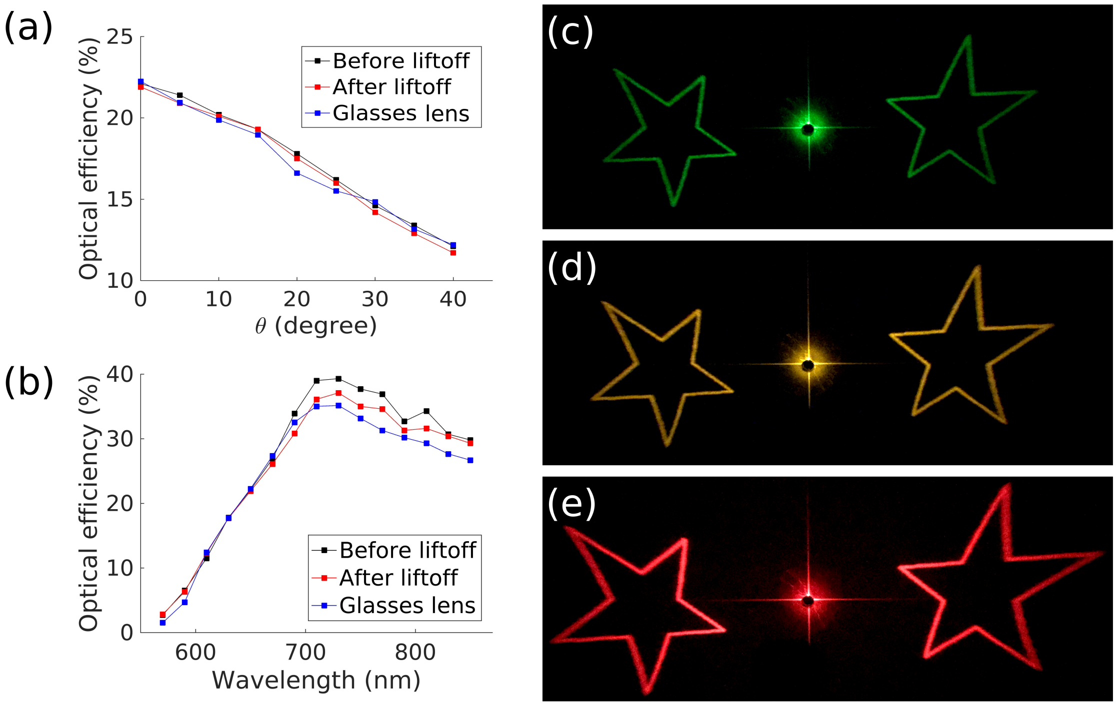

Figure 4.4: Measured efficiency for RCP incident light vs (a) the angle between the normal to the surface of the FHMS and the incident beam for $\lambda = 650$ nm and (b) the wavelength of the beam for normal incidence. Experimentally obtained images after lift-off for the light beams at (c) 570 nm (d) 590 nm, and (e) 690 nm. These images were taken with RCP light at normal incidence [78].

4.2.2 Experimental holographic images on flat surfaces

Experimental holographic image results for the fabricated devices are displayed in figure 4.5, which shows that the flexible device can form high-fidelity helicity multiplexed holograms. Figure 4.5(a)-(b) show the numerically generated target images for RCP and LCP light respectively. The rotation of the holographic image around the zeroth order occurs because changing the helicity of the incident light maps the hologram phase-shift $\phi_0(x_O, y_O, 0)$ into $-\phi_0(x_O, y_O, 0)$ [33, 84]. This phenomena is explored in greater detail later in this chapter.

The experimental images in figure 4.5(c)-(d) were acquired using the setup of figure 4.2(b). The distortion due to the spherical far-field being projected onto a flat plane has been pre-compensated for as detailed in figure 4.1. This, combined with the non-optimised camera focus, contributed to the poor-fidelity of the edges of figure 4.5(c) and 4.5(d).

In the far-field, the focus of the holographic images is robust to the exact distance to the screen, and their size scales linearly with this distance without distortion. This occurs because the image is designed to be viewed at infinity, so once the image is formed there are no further distortions as the distance from the FHMS increases. The cross in the centre of figure 4.5(c)-(d) is a simple measurements artefact due to the FHMS acting as a square aperture. Panels (e-g) of figure 4.5 show a zoomed-in view of the designed image, and the images obtained before and after lift-off, respectively. These results demonstrate that the process of lift-off does not lead to any visible degradation in the image fidelity or the signal-to-noise ratio. Furthermore, these results show that this process is compatible with holograms that are both high-fidelity, and containing high-frequency terms in the visible range.

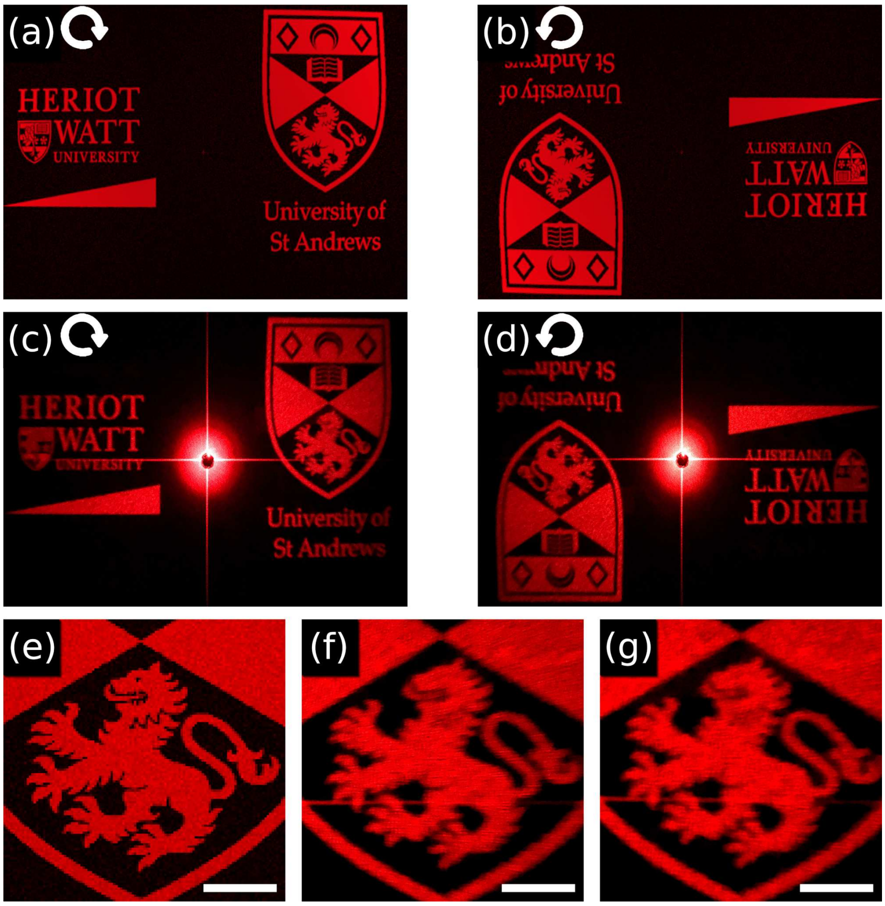

Figure 4.5: Reconstructed images for the incident light with a wavelength of 650 nm at normal incidence. The simulation results for incident light that is (a) RCP (b) LCP and the corresponding experimental results after lift-off shown in (c)-(d). (e) Simulated close up of the lion. The comparison of experimentally measured close up of the lion (f) before and (g) after lift-off from the carrier. The scale bar is 10 mm with a FHMS to screen spacing of 100 mm. The University of St Andrews logo is © University of St Andrews and used with permission. The Heriot-Watt logo is © Heriot-Watt University and used with permission [78].

4.2.3 Conformability

To demonstrate that the flexible membranes retain their functionality when transferred to different targets, as visible in figure 4.6, the FHMS was placed on a glasses lens with a radius of curvature of 140 mm. This corresponds to a phase change of 1.1π between the outside and centre of the FHMS. Qualitatively, it can be seen in figure 4.6(b) that there is some defocussing effect and a lower signal-to-noise ratio than figures 4.5(f)-(g). Clearly, the effect of curvature can be detrimental to the image quality, but this allows for the surface topography specific holograms which are detailed below.

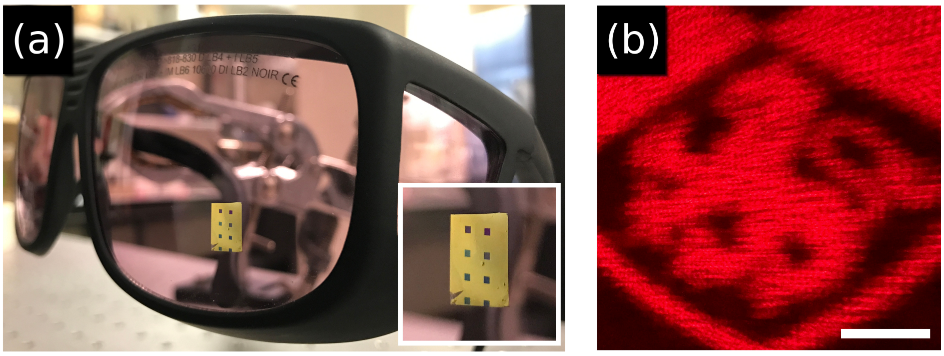

Figure 4.6: (a) The FHMS conformed to a pair of safety glasses. The inset is a close up of the FHMS. (b) An experimentally obtained image with the FHMS conformed to the glasses for the incident light with a wavelength of 650 nm at normal incidence. The scale bar is 10 mm with a FHMS to screen spacing of 100 mm. The University of St Andrews logo is © University of St Andrews and used with permission. The Heriot-Watt logo is © Heriot-Watt University and used with permission [78].

A strength of this approach is that devices can be tailored for specific use cases. Here, the FHMS conforms to the general shape of the object it rests on, in this case, a glasses lens. The impact of fine surface roughness can be negated by adjusting the thickness of the manipulation layer. A thicker manipulation layer conforms less to the surface roughness and is thus ideal for holography. However, a thinner manipulation layer should be used when a higher degree of conformability to the surface is required, as is the case for tightly curved FHMSs.

4.3 Holograms for non-flat surfaces

To design FHMSs for determined arbitrary carrier shapes, the Kirchoff propagator and the GSA, as detailed in chapter 2, was used. For the sake of simplicity, the case of cylindrical carriers is considered, without loss of generality. For more complex carrier shapes, it is essential to align the FHMS to the topography of the carrier. This can be achieved by patterning standard alignment marks on both the sample and the carrier before using simple micro-positioning tools with the aid of an optical microscope [27]. This technique allows for sub-micron resolution positioning while being robust and repeatable. The parameters detailing the design of this FHMS are in table 4.1.

Table 4.1: **Non-flat hologram parameters**

Parameter	Value
Hologram pixels	2501 × 2501
Holographic image pixels	183 × 183
Hologram pixel pitch	300 nm
Holographic image pixel pitch	0.1639 mm
Holographic image offset in x, y, z	0, 35, 80 mm
Wavelength	630 nm
Hologram radius of curvature along the x direction	6 mm

Here, the FHMS, with an area of 0.75×0.75 mm^2, was designed for RCP incident light. The holographic image, occupying an area of 30×30 mm^2, was offset from the incident beam along the y axis to avoid interference with the unconverted light.

The FHMS devices created with this process have a strong image quality dependence on the carrier shape. This property could be harnessed for sensing and anti-counterfeiting applications. To quantitatively measure the sensitivity of the FHMS to deformations from the intended topologies, different samples for different radii of curvature were fabricated. Specifically, the FHMS was designed to form clear holographic images when applied to a flat surface and to convex cylinders with radii of 4 mm and 6 mm. The rest of the holographic design parameters are displayed in table 4.1.

The numerical and experimental results are in excellent agreement, as visible in figure 4.7. A high-fidelity image is only seen when the radius of curvature of the object matches that of the design. Furthermore, the more significant the difference between the designed and the actual radius of curvature of the FHMS the more significant the distortion in the holographic image.

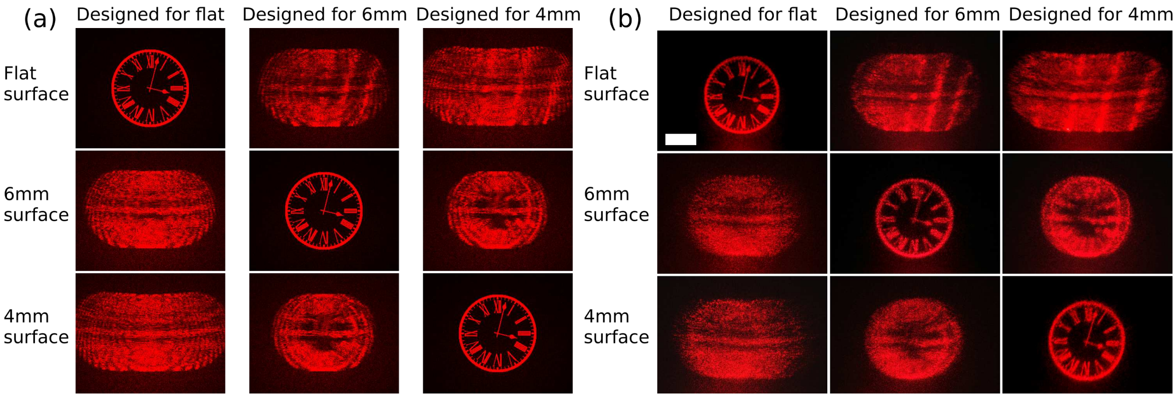

Figure 4.7: (a) Simulated results displaying holograms designed for three different convex cylindrical radii of curvature. (b) Experimental results displaying the holograms conformed to three glass cylinders with different radii of curvature. The scale bar is 10 mm [72].

The distortion of two images, A and B, can be quantified by a correlation coefficient, which is defined by equation 4.1 as

$$r = \frac{\Sigma_m \Sigma_n \left(A_{mn} - \bar{A}\right)\left(B_{mn} - \bar{B}\right)}{\sqrt{\left(\Sigma_m \Sigma_n \left(A_{mn} - \bar{A}\right)^2\right)\left(\Sigma_m \Sigma_n \left(B_{mn} - \bar{B}\right)^2\right)}}, \tag{4.1}$$

where $\bar{A}$ and $\bar{B}$ are the mean values of the two images. This value is normalised to a value of 1 for identical images and -1 for perfectly complementary images. The correlation values, comparing the images of figure 4.7(a) and the target image, are displayed in table 4.2.

Table 4.2: Simulated correlation coefficients for designed FHMSs applied to different carrier topologies

	Design		
Applied	R=∞	R=6 mm	R=4 mm
R=∞	0.9635	0.3439	0.2975
R=6 mm	0.3570	0.9640	0.4518
R=4 mm	0.3003	0.4458	0.9652

4.4 Tuning the holographic image sensitivity to the surface topography

It is vital for applications of holograms which are sensitive to the surface topography, e.g. for anti-counterfeiting or sensing, that the sensitivity of the holographic image to the surface topography can be tuned. As such, this section describes a method to tailor this sensitivity.

The selectivity depends on the difference between the designed topography and the actual shape of the surface topography. This effect can be enhanced if the information is encoded in the regions of the FHMS that have the highest gradient relative to the designed topography. Clearly, reducing the active area of the phase pattern has the detrimental effects of decreasing both the intensity of the holographic image and the width of its spectral content. The sensitivity also depends on the size of the holographic image, since smaller features are affected more by the same amount of deformation.

For the cylindrical case, FHMSs with an increasingly large gap in the central section of the phase pattern η (expressed as a fraction of the side of the FHMS), were designed, with the results summarised in figure 4.8. The areas of the smallest gradient, relatively to the designed topography, are within these η regions. In panel (a) of figure 4.8, an example of phase patterns with varying gap width are illustrated, each designed to create the same target image of figure 4.7 for a cylinder with radius of curvature of 6 mm. Panel (b) of figure 4.8 shows the correlation coefficient between the resulting projected images, and the target image (figure 4.9 shows a collection of the projected images). As expected, wider phase gaps lead to an enhanced selectivity at the cost of a slight reduction in intensity and spectral resolution.

Here, some of the images used to calculate the correlation coefficient are displayed. The higher η, the steeper the fall-off in simulated holographic image quality. In all cases, the holographic image was designed for a radius of curvature of 6 mm. The holographic image quality with this radius of curvature is qualitatively unaffected.

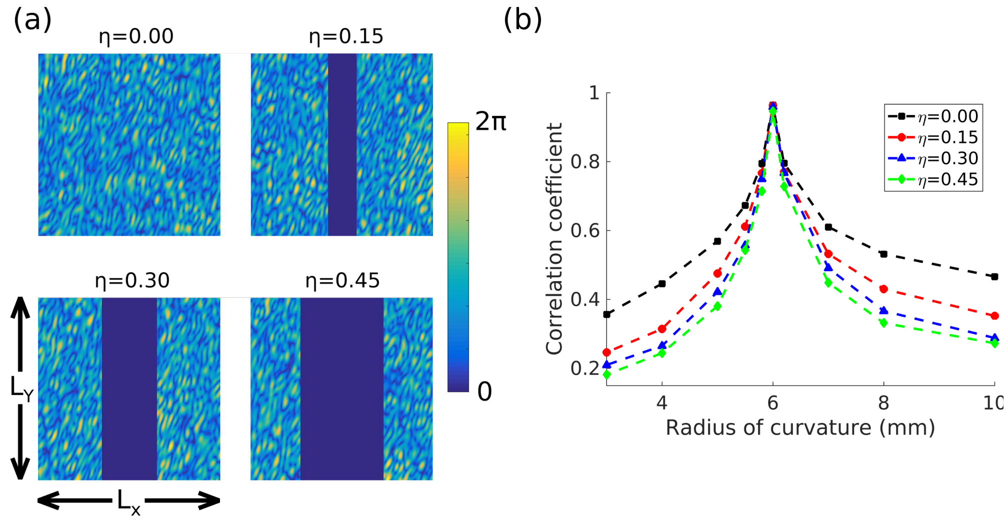

Figure 4.8: (a) Sketch of the spatial phase distributions encoded onto the FHMS for different η values. (b) Correlation coefficient vs radius of curvature for the phase profile with different η values [72].

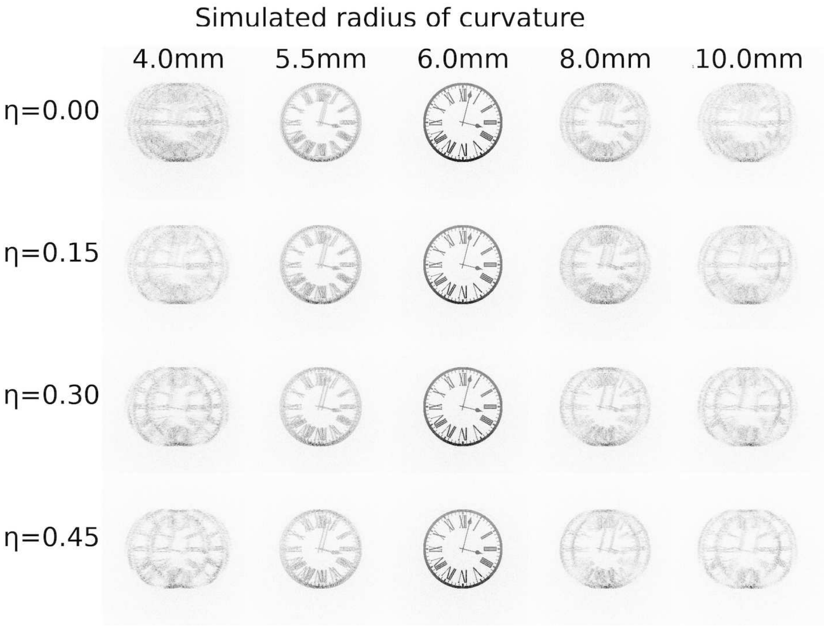

Figure 4.9: A selection of the images used to calculate the correlation coefficient for different values of η. The images are inverted for clarity [72].

4.5 Holographic image dependence on the surface topography and the incident light helicity

The relationship between helicity and surface profile becomes more complex when the FHMS is non-flat. In particular, a symmetry-type-effect occurs where a clear image is formed for both LCP light incident on a concave FHMS, and for RCP light incident on a convex FHMS. Other combinations of the handedness of the polarisation and the shape of the FHMS give distorted images.

4.5.1 Theoretical explanation for the symmetry between the surface topography and the helicity of incident light

This effect is described mathematically below. Equations 2.15 and 2.23 from chapter 2 can be combined to find the intensity of the hologram wavefront in the holographic image plane as

$$\begin{aligned} I(x_I, y_I, z_I) \approx \Bigg| \Gamma(\mathbf{r}_O, \mathbf{r}_I) \iint U(x_O, y_O) \\ \times \exp(ik(z_I - z_O)) \times \exp\left(ik \frac{(x_I - x_O)^2 + (y_I - y_O)^2}{2(z_I - z_O)} \right) dx_O \, dy_O \Bigg|^2 . \end{aligned} \tag{4.2}$$

By then substituting $U(x_O, y_O, z_O) = A_0 \times \exp(i[\phi_0(x_O, y_O, z_O) + \phi_c(x_O, y_O, z_O)])$, it can be written that

$$\begin{aligned} I(x_I, y_I, z_I) \approx \Bigg| \Gamma(\mathbf{r}_O, \mathbf{r}_I) \iint A_0 \times \exp(i[\phi_0(x_O, y_O, z_O) + \phi_c(x_O, y_O, z_O)]) \\ \times \exp(ik(z_I - z_O)) \times \exp\left(ik \frac{(x_I - x_O)^2 + (y_I - y_O)^2}{2(z_I - z_O)} \right) dx_O \, dy_O \Bigg|^2 , \end{aligned} \tag{4.3}$$

where A_0 is the amplitude of the wave propagating from each meta-atom, and the total phase is given by the sum of the PB phase in the flat FHMS, $\phi_0(x_O, y_O, z_O)$, and the phase contribution from the non-flat topography $\phi_c(x_O, y_O, z_O)$.

If the angle between r_O and r_I is small, for which $r_j \simeq z_j$, this term can be approximated to a constant amplitude value. When this approximation does not hold, the relative intensity at the centre of the holographic image is higher than expected.

For flat FHMSs, $\phi_c = 0$ and ϕ_0 does not depend on the z coordinate. In this case, changing the helicity of light maps $\phi_0(x_O, y_O, 0)$ into $-\phi_0(x_O, y_O, 0)$ [33, 84].

It is then possible to write equation 4.3 as

$$\begin{aligned} I'(x_I, y_I, z_I) \approx & \left| \Gamma(\mathbf{r}_O, \mathbf{r}_I) \iint A_0 \times \exp(-i[\phi_0(x_O, y_O, 0) + 0]) \right. \\ & \left. \times \exp(ik(z_I + 0)) \times \exp\left(\frac{(x_I - x_O)^2 + (y_I - y_O)^2}{2(z_I + 0)} \right) dx_O \, dy_O \right|^2 \\ = & \left| \Gamma(\mathbf{r}_O, \mathbf{r}_I) \iint A_0 \times \exp(i[\phi_0(x_O, y_O, 0)]) \right. \\ & \left. \times \exp(-ikz_I) \times \exp\left(ik \frac{-(x_I - x_O)^2 - (y_I - y_O)^2}{2z_I} \right) dx_O \, dy_O \right|^2 , \end{aligned} \tag{4.4}$$

which, by comparison with equation 4.3, can be simplified to

$$I'(x_I, y_I, z_I) \approx I(-x_I, -y_I, z_I). \tag{4.5}$$

Thus, the holographic image is formed rotated 180 degrees around the z axis, as expected [11, 78]. For a non-flat surface $\phi_c(x_O, y_O, z_O) \neq 0$ and equation 4.5 is invalid. However, if the FHMS is deformed so that $z_O \to -z_O$, $\phi_c(x_O, y_O, z_O)$ maps into $-\phi_c(x_O, y_O, z_O)$, so it is possible to write equation 4.4 as

$$\begin{aligned} I'(x_I, y_I, z_I) \approx & \left| \Gamma(\mathbf{r}_O, \mathbf{r}_I) \iint A_0 \times \exp(-i[\phi_0(x_O, y_O, z_O) + \phi_c(x_O, y_O, z_O)]) \right. \\ & \left. \times \exp(ik(z_I + z_O)) \times \exp\left(\frac{(x_I - x_O)^2 + (y_I - y_O)^2}{2(z_I + z_O)} \right) dx_O \, dy_O \right|^2 \\ = & \left| \Gamma(\mathbf{r}_O, \mathbf{r}_I) \iint A_0 \times \exp(i[\phi_0(x_O, y_O, z_O) + \phi_c(x_O, y_O, z_O)]) \right. \\ & \left. \times \exp(-ik(z_I + z_O)) \times \exp\left(ik \frac{-(x_I - x_O)^2 - (y_I - y_O)^2}{2(z_I + z_O)} \right) dx_O \, dy_O \right|^2 . \end{aligned} \tag{4.6}$$

In this case, equation 4.5 holds approximately true. The relative phase-shift causes residual image distortion, however, at z_I for the two different configurations $z_I - z_O$ and $z_I + z_O$. This can be ignored for large z_I. The relationship between the incident helicity of light and the surface topography to the holographic image is detailed in figure 4.10.

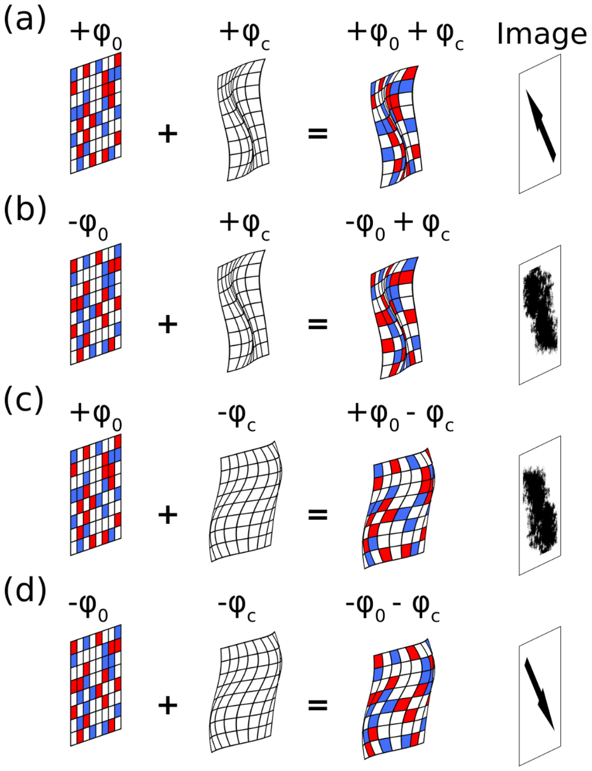

Figure 4.10: Simulated combinations of phases for a hologram with an arbitrary topography. Here, a three-level phase hologram is shown for illustrative purposes. Pixels coloured in red, blue, and white correspond to positive, negative, and no phase-shift respectively. $\phi_0(x_O, y_O, z_O)$ originates from the PB phase required on a flat topography. $\phi_c(x_O, y_O, z_O)$ originates from the difference in the designed topography and the actual surface topography. (a)-(b) show the ϕ_c phase from an arbitrary topography. (c)-(d) show the ϕ_c phase from the same surface topography, but reflected in the xy plane at $z = 0$. (a) and (c) show RCP incident light. (b) and (d) show LCP incident light [72].

4.5.2 Experimental holographic images relating surface topography to the incident light helicity

Experimental images are shown in figure 4.11. A slightly distorted holographic image, rotated 180 degrees around the z axis, can be seen for RCP light on a convex cylindrical surface, again with a radius of curvature of 6 mm. As expected, in the cases of RCP light on a concave cylindrical surface and LCP light on a convex cylindrical surface, the holographic image is severely distorted.

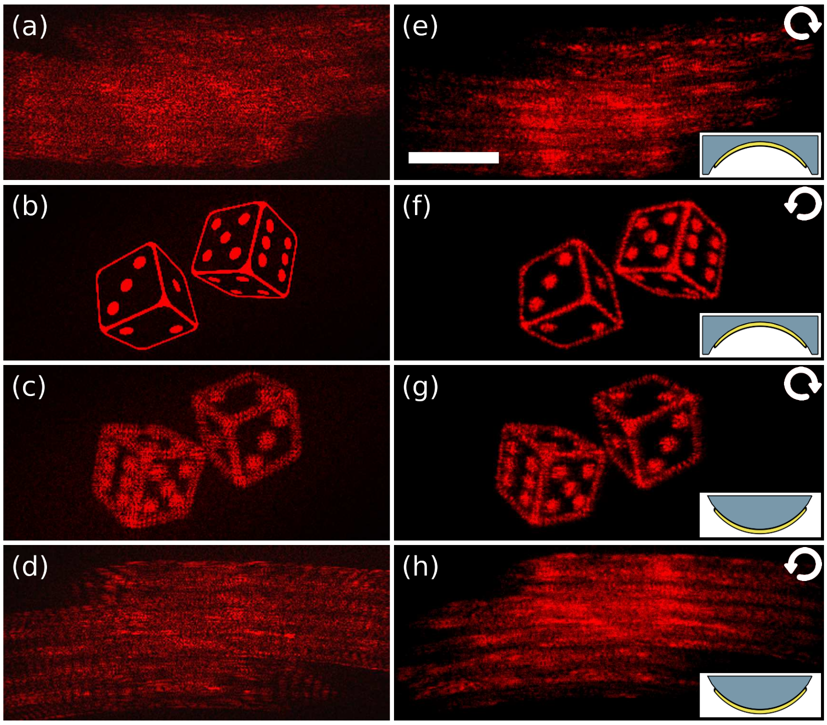

Figure 4.11: (a-d) display simulated holographic images (e-h) display experimental holographic images. (a,e) and (b,f) were taken on a concave cylinder with a radius of curvature of 6 mm. (c,g) and (d,h) were taken on a convex cylinder with the same radius of curvature. (a,e) and (c,g) were taken with RCP incident light. (b,f) and (d,h) were taken with LCP incident light. The LCP images are rotated 180 degrees about the z axis in the xy plane. The scale bar is equivalent to 10 mm [72].

4.6 Coupling the carrier shape to the hologram function

Traditionally, FHMSs have a shape decoupled from their function [11, 46]. However, FHMSs have been used to compensate for aberrations in conventional optics using non-flat surfaces [8, 9]. In the following, it is demonstrated (in simulation) that coupling the shape and function of a FHMS device can improve the proportion of light confined within the focal spot of a FHMS lens. Although this is provided as a specific example, this technique is general and could be realised in different implementations.

For these simulations three FHMS shapes were compared, a concave hemisphere, a convex hemisphere, and a flat surface. The radii of curvature for the hemispheres were ±0.5 mm, and the flat surface has an effective radius of curvature of ∞. The parameters used to generate the hologram with the GSA are displayed in table 4.3. $x = y = z = 0$ is defined as the centre of the hologram at the closest z position to the holographic image plane.

Table 4.3: **Non-flat holographic lens parameters generation**

Parameter	Value
Hologram pixels	2000×2000
Holographic image pixels	3×3
Hologram pixel pitch	300 nm
Holographic image pixel pitch	0.3 mm
Holographic image offset in x, y, z	0.0, 0.0, 0.5 mm
Wavelength	630 nm

To then simulate the resultant spot from each hologram,the parameters in tables 4.4 and 4.5 were used for the xy and xz planes respectively.

Table 4.4: **Non-flat holographic lens parameters analysis in** xy

Parameter	Value
Hologram pixels	2000×2000
Holographic image pixels	160×160
Hologram pixel pitch	300 nm
Holographic image pixel pitch	100 nm
Holographic image offset in x, y, z	0.0, 0.0, 0.5 mm
Wavelength	630 nm

Table 4.5: **Non-flat holographic lens parameters analysis in** xz

Parameter	Value
Hologram pixels	2000×2000
Holographic image pixels	160×320
Hologram pixel pitch	300 nm
Holographic image pixel pitch	100 nm
Holographic image offset in x, y, z	0.0, 0.0, 0.5 mm
Wavelength	630 nm

These simulated results are displayed in figure 4.12

Here, it is demonstrated that the concave lens has the highest central spot efficiency, and contrast between the spot and the surroundings. To quantify this, the holographic image spot size resulting from the three FHMS shapes in the x, y, and z planes was calculated (with the assumption that the spot ends once the intensity had fallen to $1/e$ of the peak spot intensity).

The spot sizes in the xy planes were all found as 8×8 pixels. Similarly, the spot sizes in the xz

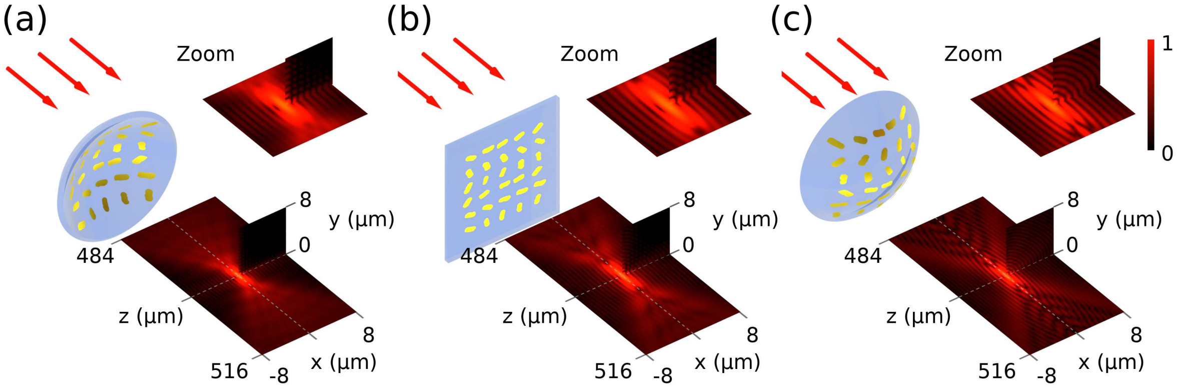

Figure 4.12: Simulated images of focused spots from (a) concave (b) flat (c) convex FHMSs. The xy plane data only shows $\frac{1}{4}$ of the xy holographic image plane so that it can be seen with the xz plane. The incident light is reflected from the FHMSs.

planes were 8×41, 8×50, and 8×34 for the concave, flat, and convex FHMS shapes respectively.

Next, the proportion of the light confined within the central spot compared to the area outside it in the holographic image plane was calculated. In the xy plane, these ratios were 0.26, 0.16, and 0.066 for the concave, flat, and convex FHMS shapes respectively. In the xz plane, these ratios were 0.075, 0.096, and 0.083 for the concave, flat, and convex FHMS shapes respectively.

This demonstrates that by coupling the shape of the FHMS to the function (e.g. a concave FHMS as a converging lens) the spot efficiency in the xy plane can be significantly improved compared to a flat FHMS. This platform also allows control over the size of the spot in the xz plane, which acts as one input for the efficiency of the spot in this plane. Because the concave FHMS creates a smaller spot than the flat case in the xz plane, it is unsurprising that it also has a lower efficiency in this plane.

4.7 Conclusion

We have designed and fabricated a conformable FHMS capable of supporting helicity multiplexed holograms in the visible range. The FHMSs are realised with gold nanorods positioned point-by-point to define a PB phase profile, and uses a three-layer reflective design. Importantly, this device is conformable to planar and curved surfaces, and by controlling the helicity of the incident light, the two high-fidelity, broad-angle, broadband, images can be interchanged at will. Furthermore, it has been demonstrated that these FHMSs can be designed to form a holographic image that depend on the specific surface topography. We have also theoretically and experimentally demonstrated that the symmetry properties of the formed images depend on both the helicity of the polarisation and the phase contribution of the surface topography. Furthermore, the specificity of the FHMSs can be enhanced by engineering the phase distribution, at the cost of a small loss in holographic image quality. Finally, the shape of the FHMS can be coupled to the function to improve its performance, in particular, to create a more tightly focused spot with higher contrast to the background for lensing applications.

4.8 Contribution

I designed the holograms, ran the simulations, fabricated all of the samples, and performed all of the experiments.

CHAPTER 5

Holograms for light-sheet fluorescent microscopy

This chapter details a HMS platform where the hologram creates a light-sheet for LSFM. LSFM is the state-of-the-art technique for capturing three-dimensional fluorescence images of small objects [89, 90, 91].

5.1 Concept

LSFM allows for high-quality imaging of thick cells and dramatically suppresses the background fluorescence from out-of-focus fluorescent objects compared to other single-molecule super-resolution microscopy techniques [90]. This makes LSFM an invaluable tool for researchers, in particular, for probing transparent tissues and small organisms within a microfluidic cell.

Typically, to create the light-sheet a complicated set of cylindrical lenses, mirrors, prisms, and multiple objectives are required. These optical setups are overly complex to create and maintain [89, 90, 91], which limits their real-world applications.

Our solution is to create a microfluidic chip with a HMS embedded within it, which is illustrated in figure 5.1. This HMS is illuminated at normal incidence through an objective with a simple collimated laser beam and is designed to generate an off-normal light-sheet so that the object-of-interest is not directly excited by the incident laser. The light-sheet excites the object-of-interest, which generates fluorescence that is captured by the objective. This HMS replicates the function of both the incident and the collection optics, and thus allow for simpler, cheaper, and more reliable LSFM setups.

Furthermore, this platform could be extended by using multiple HMS patterns, each creating a separate light-sheet in a different plane and at a different angle. The incident beam could then be quickly scanned over the HMSs, to create many cross-sections of the object, and thus observe it from multiple directions almost simultaneously.

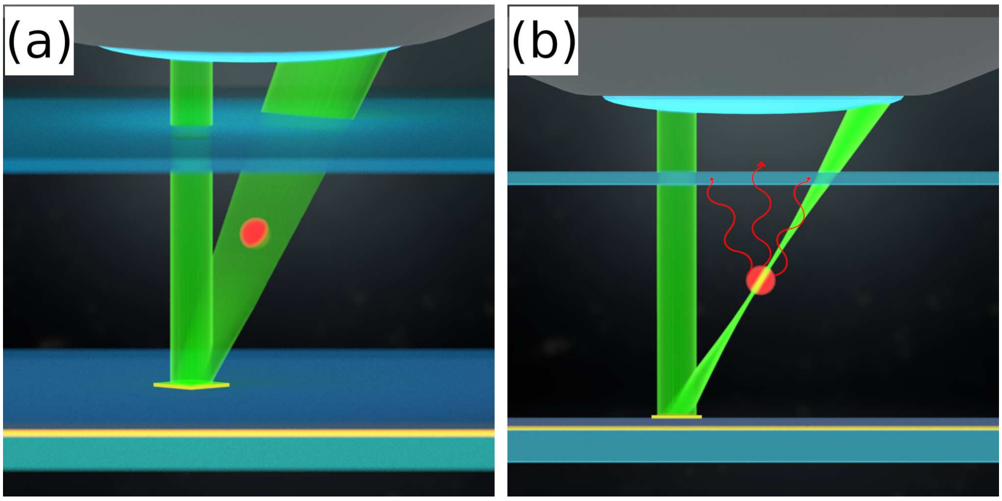

Figure 5.1: A sketch of the working principle of the HMS light-sheet. A collimated beam passes into the microfluidic cell and illuminates the HMS. The HMS generates a light-sheet which illuminates the target object. This target object then fluoresces, which can be detected through the objective lens. This is shown from an (a) isometric and (b) side-on perspective.

5.2 Hologram design

For an effective LSFM scheme, the light-sheet created by the HMS should have a waist of approximately 5 μm in x', a length of 100 μm in y', and a depth of around 20 μm in z' [89, 90]. These planes are defined in figure 5.2.

The angle of the light-sheet was designed around the practical constraints of a standard Mitutoyo 50× objective with a field-of-view of 900 μm. Following this constraint, the incident beam and HMS were designed to have an area of 300 × 300 μm^2. The light-sheet angle was then chosen to place the beam-waist around the centre of the field-of-view (spaced 150 μm from the edge of the HMS and incident laser).

To find the best method of generating light-sheets via holography, three different methods (which are detailed below) were attempted.

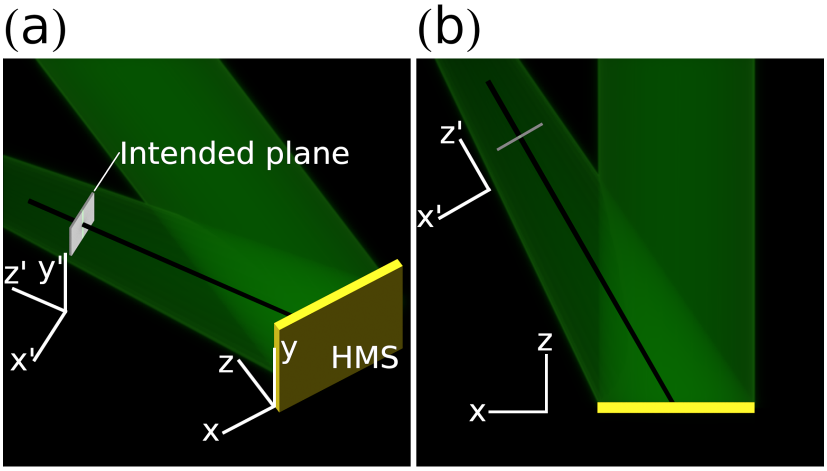

Figure 5.2: A schematic of the HMS under illumination and creating a holographic image from two different perspectives where (a) is isometric and (b) is top-down. The holographic image plane is labelled as the 'Intended plane'.

For the application of LSFM, the incident laser will have a wavelength of $\lambda = 532$ nm, and thus once it passes through water, which has a refractive index of $n = 1.33$, the wavelength is $\lambda = 400$ nm. As such, $\lambda = 400$ nm was used for most of the simulations below.

5.2.1 A holographic image approach

For this method, a standard GSA approach, as detailed in chapter 2, was used to create an image of a light-sheet in the region-of-interest. The target image is displayed in figure 5.3 and the parameters to create this hologram are given in table 5.1.

To simulate the holographic images, the RS propagator, as described in chapter 2, was used with the parameters displayed in tables 5.2 and 5.3 for the $x'y$ and xz plane simulations respectively.

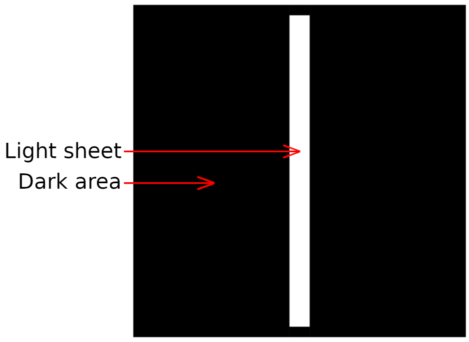

Figure 5.3: Target image to create the required light-sheet.

Table 5.1: **Generation - Light-sheet by holographic image parameters**

Parameter	Value
Hologram pixels	1000×1000
Holographic image pixels	250×250
Hologram pixel pitch	300 nm
Holographic image pixel pitch	400 nm
Holographic image orientation	The $x'y$ plane
Holographic image offset in x, y, z	-0.30, 0.00, 0.52 mm
Wavelength	400 nm

Table 5.2: **Analysis - Holographic image parameters in x′y**

Parameter	Value
Hologram pixels	1000×1000
Holographic image pixels	250×625
Hologram pixel pitch	300 nm
Holographic image pixel pitch	400 nm
Holographic image orientation	The $x'y$ plane
Holographic image offset in x, y, z	-0.30, 0.00, 0.52 mm
Wavelength	400 nm

Table 5.3: **Analysis - Holographic image parameters in xz**

Parameter	Value
Hologram pixels	1000×1000
Holographic image pixels	250×250
Hologram pixel pitch	300 nm
Holographic image pixel pitch	400 nm
Holographic image orientation	The xz plane
Holographic image offset in x, y, z	-0.30, 0.00, 0.52 mm
Wavelength	400 nm

The resultant hologram and holographic image are displayed in figure 5.4. Panel 5.4(a) displays the hologram phase profile, panel 5.4(b) and 5.4(c) display the holographic image when propagated using the parameters in tables 5.2 and 5.3 respectively.

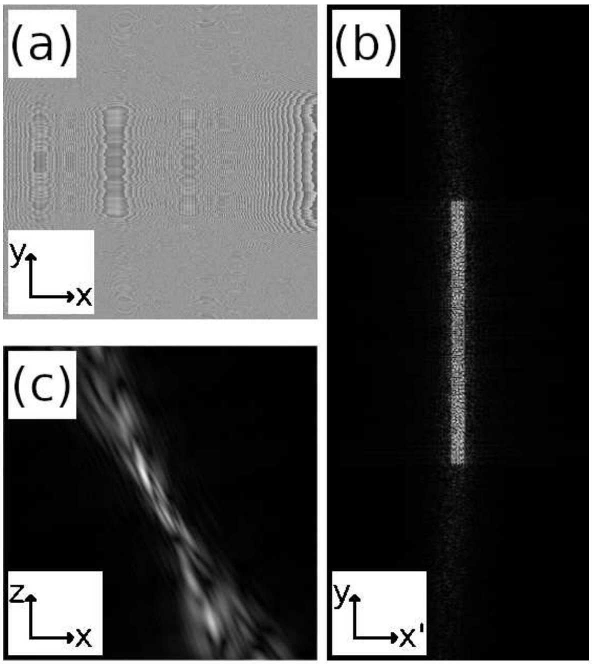

Figure 5.4: (a) The hologram phase profile. (b) Holographic image along $x'y$. (c) Holographic image along xz.

Figure 5.4, displays good agreement between the target image and panel 5.4(b). Panel 5.4(c), however, shows that the resultant beam does not have a uniform intensity profile. This is likely not a problem as the features in the resultant light-sheet are on the order of 250 nm, which is too small to resolve with LSFM. The central region of this beam propagates for approximately 20 μm, with a beam width (FWHM) that is 5 ± 1 μm. This beam is likely suitable for LSFM but a thinner, more uniform, beam would likely give better results.

5.2.2 A Bessel beam approach

For this method, conical phase gradients were created, which are well known to generate Bessel beams [8]. An example of a conical phase gradient is displayed in figure 5.5.

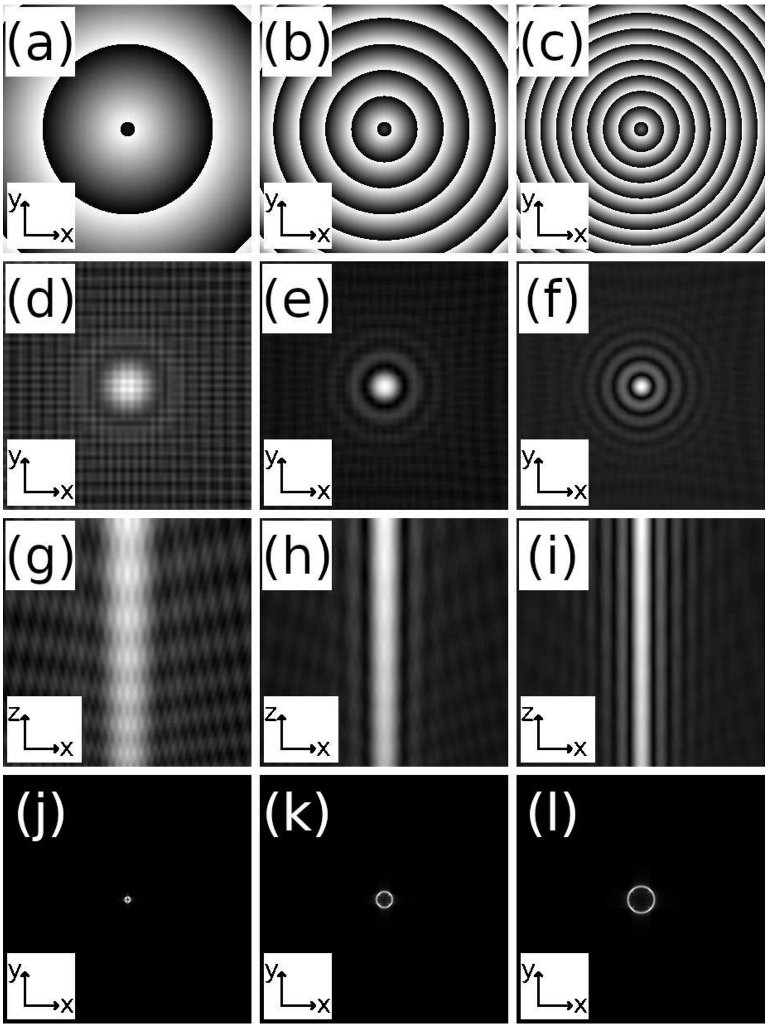

Figure 5.5: The hologram phase profile where the phase had a peak value of (a) 10 radians (b) 30 radians and (c) 50 radians. This peak phase value sets the steepness of the phase gradient and thus, the confinement of light in the holographic image. The holographic images along xy for (a),(b), and (c) are shown in (d),(e), and (f). The holographic images along xz for (a),(b), and (c) are shown in (g),(h), and (i). The FFT of (a),(b), and (c) are shown in (j),(k), and (l).

These Bessel beam phase gradients were then propagated into the xy, xz, and the far-field xy planes, to investigate the effect of the key parameters.

One key parameter was the steepness of the phase gradient cone. Using a steeper phase gradient creates a more confined spot but increases the amount of light present in the side lobes as can be seen in figure 5.5(d-f).

Using this information, Bessel beam phase gradients were created with different steepness along their x and y axes. This thesis labels this difference in gradient along the two axes of the Bessel phase cone the 'Bessel aspect ratio', where 1:1 gave the standard conical shape shown in figure 5.5. Altering the Bessel aspect ratio allows for confining the light tightly along one axis but not the other, as shown in figure 5.6.

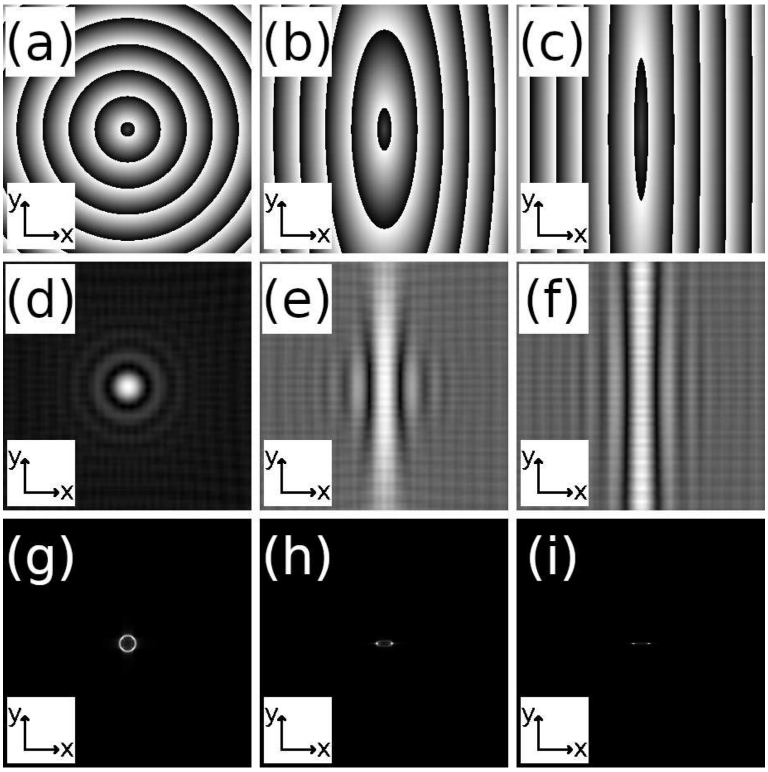

Figure 5.6: Resulting holograms and holographic images for three different Bessel aspect ratios of (a,d,g) 1:1 (b,e,h) 3:1 and (c,f,i) 10:1. The hologram phase profiles are displayed in (a-c). The holographic images along xy are displayed in (d-f). The FFT holographic images along xy are displayed in (g-i).

To create the Bessel beam hologram, the parameters shown in table 5.4 were used. The resultant hologram and holographic image are displayed in figure 5.7. Panel 5.7(a) displays the hologram phase profile, panel 5.7(b) and 5.7(c) display the holographic image when propagated using the parameters in tables 5.2 and 5.3 respectively.

Table 5.4: **Generation - Light-sheet by Bessel parameters**

Parameter	Value
Hologram pixels	1000 × 1000
Hologram pixel pitch	300 nm
Holographic image orientation	The $x'y$ plane
Bessel phase peak	40 rad
Bessel aspect ratio	10:1
Holographic image offset in x, y, z	-0.30, 0.00, 0.52 mm
Wavelength	400 nm

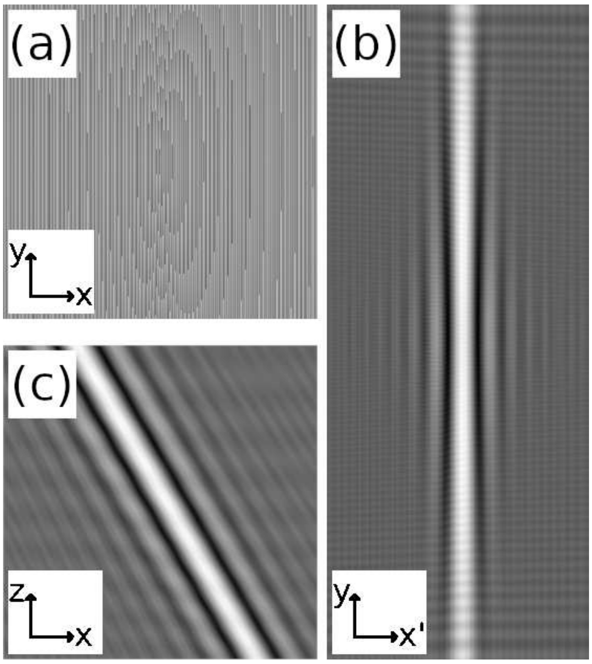

Figure 5.7: (a) The hologram phase profile. (b) Holographic image along $x'y$. (c) Holographic image along xz.

Figure 5.7 shows that the Bessel approach creates a cleaner beam than the holographic image approach. The depth of focus of this beam is substantially higher than 100 μm, but the beam width (FWHM) is more extensive than desired at approximately 9 μm. Another disadvantage of this approach is that a higher percentage of the light is unconfined within the central beam. Therefore, the characteristics of this beam are marginal for use in LSFM.

5.2.3 A Gaussian beam approach

In the previous sections, it was shown that the holographic image approach to creating a light-sheet gave non-uniform beams but good confinement. The Bessel approach, however, gave a high-quality beam but weak confinement, meaning that much of the light in the Bessel beam was created outside of the light-sheet.

In this Gaussian-based method, an attempt to create a high-quality well-confined Gaussian beam was made using the equation [50]

$$\phi(x_O, y_O, z_O) = \frac{\pi}{\lambda} \times \left(\sqrt{(x_I - x_O)^2 + (y_I - y_O)^2 + (z_I - z_O)^2} - (z_I - z_O) \right). \tag{5.1}$$

Here, $\phi(x_O, y_O, z_O)$ is the phase in radians, and x_j, y_j, z_j are the Cartesian coordinates identified by the position vectors r_j. The subscripts $j = O, I$ refer to the hologram and holographic image planes respectively, and k is the wavevector of light. The holographic image coordinate (x_I, y_I, z_I) is the focal point of the Gaussian beam.

The resulting phase distribution to encode as the HMS is parabolic, and similar to the Bessel beam approach gives a circularly symmetric beam. A light-sheet is required, however, and so again the ratio of the phase gradient along the x and y axes was modified. The phase gradient ratio was modified by stretching the phase to a different ratio, e.g. 1:2, and then cropping the phase gradient to the intended hologram resolution. An example hologram, and holographic images, are shown in figure 5.8.

To create the Gaussian beam hologram, the parameters shown in table 5.5 were used. The resultant hologram and holographic image are displayed in figure 5.9. Panel 5.9(a) displays the hologram phase profile, panel 5.9(b) and 5.9(c) displays the holographic image when propagated using the parameters in tables 5.2 and 5.3 respectively.

Figure 5.9, displays that the Gaussian approach creates a much cleaner beam than the holographic image approach while confining the same amount of light within the central beam. The central

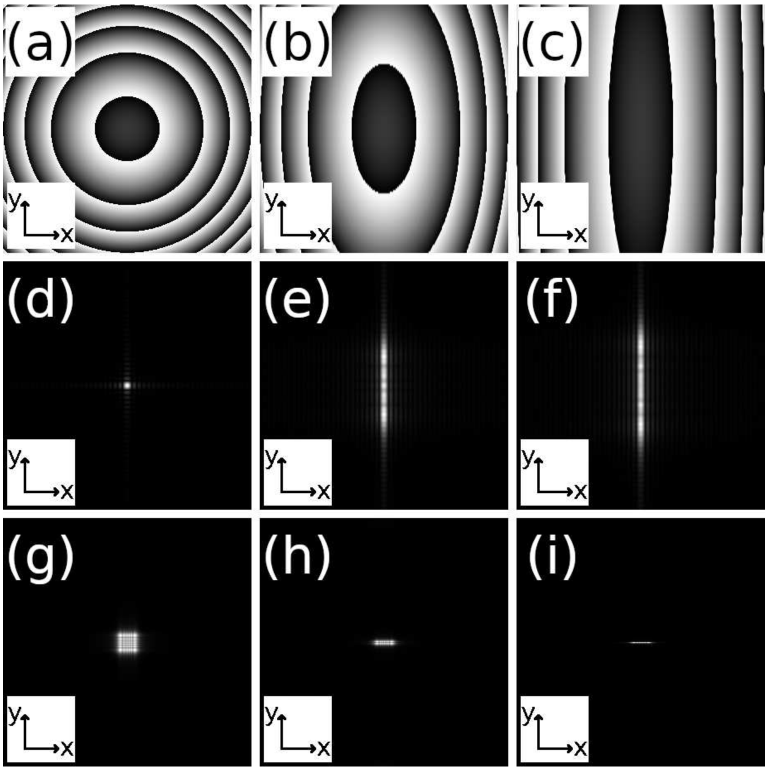

Figure 5.8: Resulting holograms and holographic images for three different Gaussian aspect ratios of (a,d,g) 1:1 (b,e,h) 3:1 and (c,f,i) 10:1. The hologram phase profiles are displayed in (a-c). The holographic images along xy are displayed in (d-f). The FFT holographic images along xy are displayed in (g-i).

Table 5.5: **Generation - Light-sheet by Gaussian parameters**

Parameter	Value
Hologram pixels	1000×1000
Hologram pixel pitch	300 nm
Holographic image orientation	The $x'y$ plane
Bessel aspect ratio	2:1
Holographic image offset in x, y, z	-0.30, 0.00, 0.52 mm
Wavelength	400 nm

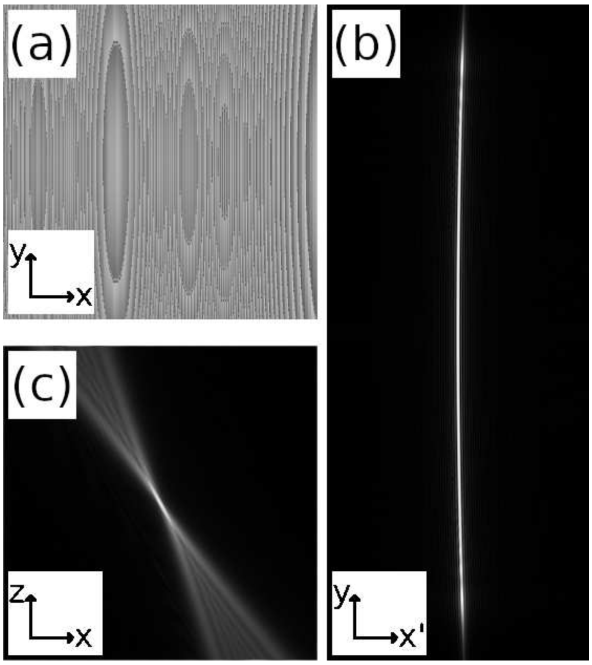

Figure 5.9: (a) The hologram phase profile. (b) Holographic image along $x'y$. (c) Holographic image along xz.

region of this beam propagates for approximately 20 μm, with a beam width (FWHM) that is below 6 μm. The central beam width (FWHM) is approximately 2 μm. Consequently, the Gaussian beam looks promising for LSFM. The main disadvantage of the Gaussian beam approach compared to the Bessel beam approach is the depth of focus, which is investigated further in the next section.

5.2.4 Combining holograms for a more extended depth of focus

To work around the shorter depth of focus of the holographic image and Gaussian light-sheet approaches (compared to the Bessel beam approach) two holograms were recovered, one creating a light-sheet farther from the intended light-sheet plane and another one closer. These planes were evenly spaced, and a schematic of this is displayed in figure 5.10. These holograms were then multiplexed by taking the mean value of every complex pixel in both recovered holograms, as is standard in the literature [50].

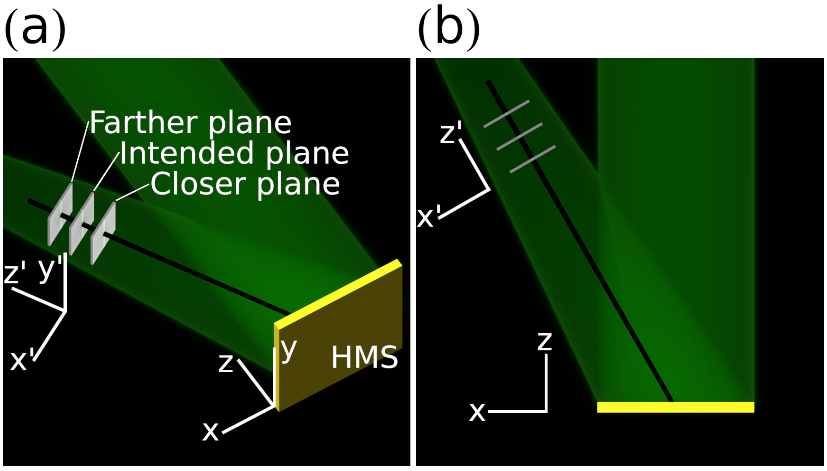

Figure 5.10: A schematic of the HMS under illumination and creating three holographic images from two different perspectives where (a) is isometric and (b) is top-down. The holographic image planes are labelled as 'Closer plane', 'Intended plane', and 'Farther plane'.

Theoretical explanation for hologram multiplexing

When two holograms, ϕ_1 and ϕ_2, are combined as $\phi_T = \frac{\phi_1+\phi_2}{2}$, the phase values of the multiplexed hologram, ϕ_T, are intermediate to ϕ_1 and ϕ_2. Consequently, ϕ_T is similar enough to ϕ_1 and ϕ_2 to reproduce both of their holographic images. An important case is that where $\phi_1 = \phi_2$. Here, the multiplexed phase $\phi_T = \phi_1 = \phi_2$ and only one (unchanged) holographic image will be seen. Furthermore, ϕ_1 and ϕ_2 are unlikely to store their most important holographic information in the same locations of ϕ_T. As a result, combining ϕ_1 and ϕ_2 causes less degradation to the holographic image than would otherwise be expected. Altering the phase of a hologram from its ideal values (by quantisation) has already been demonstrated in chapter 2 and only causes minimal degradation of the holographic image.

Implementation

For this multiplexing approach, the Gaussian beam technique, as detailed above, was used with two holograms designed to be spaced 40 μm from each other and aligned to the ideal plane $x'y'z'$, as displayed in figure 5.10. This was equivalent to a spacing of 20 μm between the adjacent planes. Figure 5.11 displays the resultant holographic images, which were simulated with the parameters displayed in table 5.3.

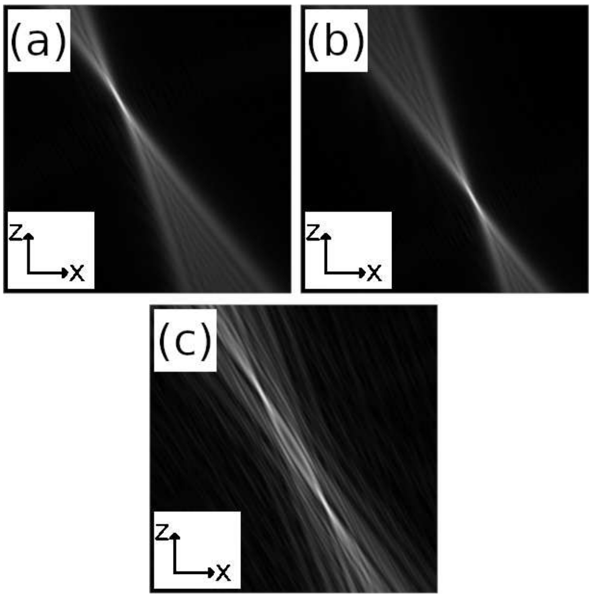

Figure 5.11: Holographic images along xz for the (a) farther (b) closer (c) multiplexed holograms.

Figure 5.11, shows that the individual holograms produce excellent light-sheets and that, when multiplexed, the resultant holographic image contains two foci. As such, the central region of this beam propagates for substantially more than 20 μm, with a beam width (FWHM) that is below 6 μm. The quality of the light-sheet, and the amount of light confined within the central focus, however, is lower. Accordingly, non-multiplexed holograms were used in the subsequent work, although, this trade-off could be worth making, were the depth-of-focus more critical than the beam quality.

5.3 Hologram design verification

To verify the code which generates and analyses holograms for the near-field (where experiments had not been made) the setup in figure 5.12 was created. Here, a beam was focused onto the back focal plane of the objective lens, which created a collimated beam close to the HMS. This beam illuminated the HMS and the same objective captured the holographic image which was then projected onto a screen for viewing. The distance between the objective and the HMS could be changed in this setup to observe how the holographic image evolved with distance from the HMS in the near-field.

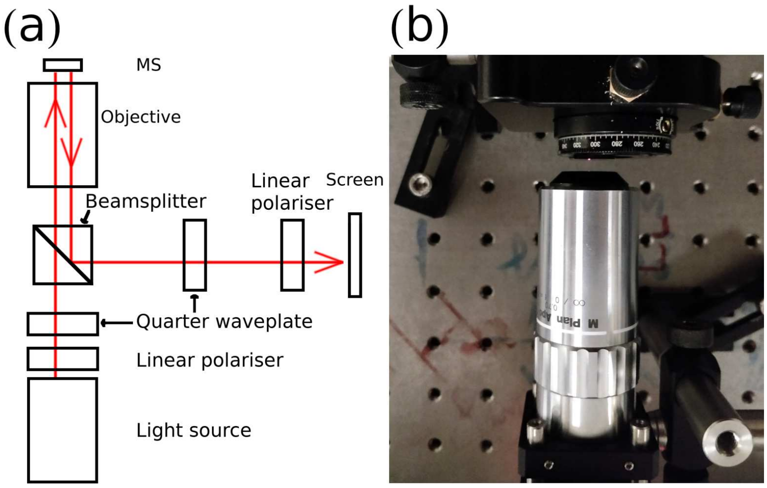

Figure 5.12: The experimental setup for the preliminary light-sheet investigation. (a) A schematic of the optical setup. (b) A photograph of the objective with a beam projected onto the HMS.

The chosen hologram design was a Bessel beam, designed with the parameters shown in table 5.6.

Table 5.6: **Generation - Verification light-sheet hologram parameters**

Parameter	Value
Hologram pixels	1501×1501
Hologram pixel pitch	300 nm
Holographic image orientation	The xy plane
Bessel phase peak	94.2 rad
Bessel aspect ratio	3:1
Holographic image offset in x, y	0.0, 0.0
Wavelength	630 nm

The resultant simulated holographic images are shown in figure 5.13, at a variety of distances and holographic image pixel pitches in the xy plane with the parameters displayed in table 5.7.

Table 5.7: **Analysis - Verification holographic image parameters in xy**

Parameter	Value
Hologram pixels	1501×1501
Holographic image pixels	100×100
Hologram pixel pitch	300 nm
Holographic image orientation	The xy plane
Holographic image offset in x, y	0.0, 0.0
Wavelength	630 nm

These simulations can be compared to the experimental images captured with the setup, which

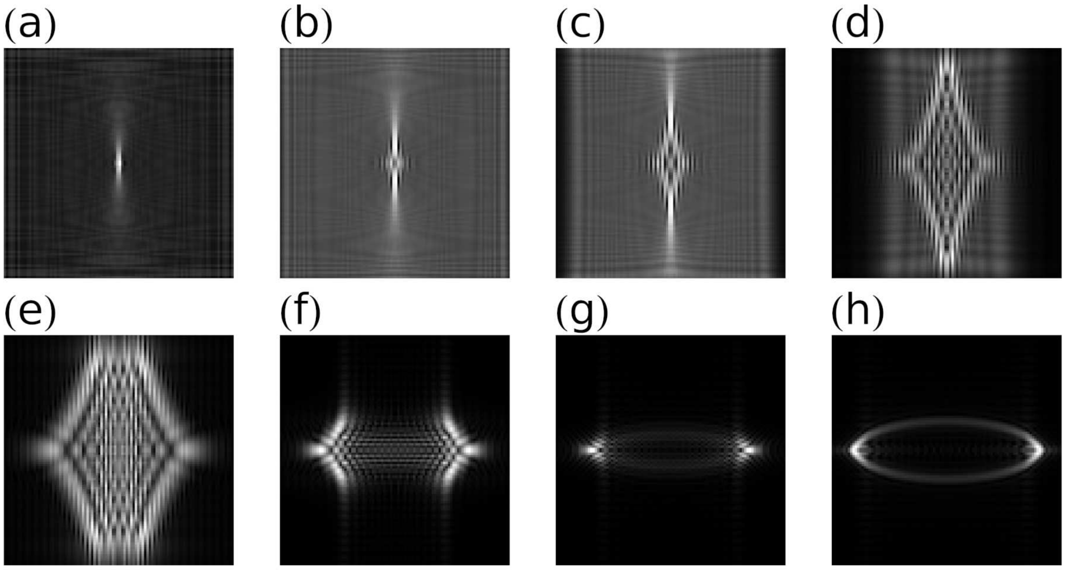

Figure 5.13: Simulated holographic images with increasing distance between the HMS and the objective lens. The distance, z, and the holographic image pixel pitch, p, are (a) $z = 0.1$ mm and $p = 4$ μm (b) $z = 0.5$ mm and $p = 4$ μm (c) $z = 1.0$ mm and $p = 4$ μm (d) $z = 2.5$ mm and $p = 4$ μm (e) $z = 4.0$ mm and $p = 4$ μm (f) $z = 10$ mm and $p = 10$ μm (g) $z = 20$ mm and $p = 20$ μm (h) $z = \infty$ from a FFT respectively.

are displayed in figure 5.14(a-g). The experimental data was not taken at the same z values as the simulations as there was no method to accurately measure this. As a result of this, there are differences between the two sets of images. Figure 5.14(h) displays the holographic image with no objective lens in the setup and projected onto a screen, which represents the far-field.

By comparing figures 5.13 and 5.14, one can be confident that the simulations are modelling the real-world propagation behaviour of the light-sheets. This agreement is particularly apparent for 5.13(h) and 5.14(h).

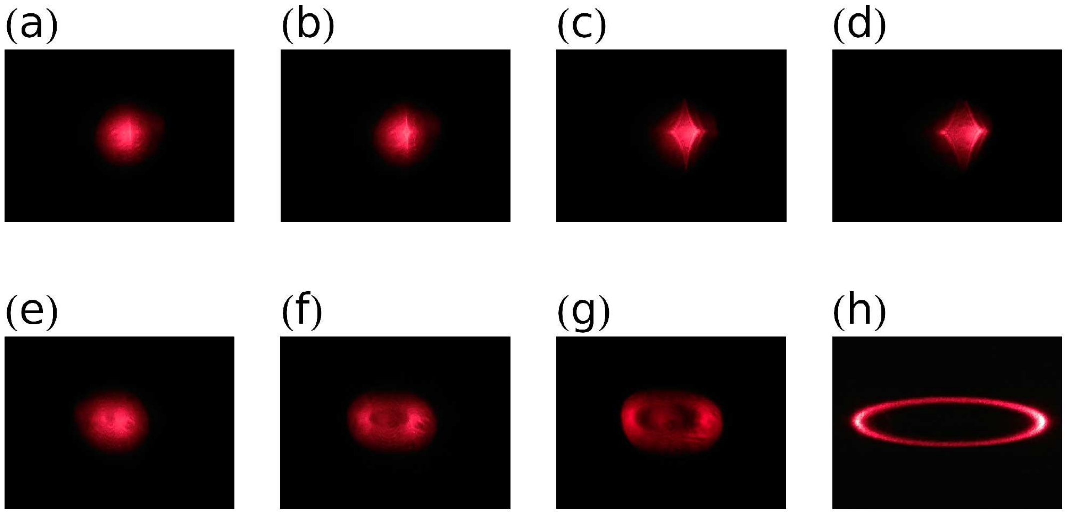

Figure 5.14: Experimental photographs with increasing distance between the HMS and the objective lens (a-g). The central spot is unconverted light reflected along the zeroth order of the beam. In the final implementation, the light-sheet will be separated from the zeroth order, and so this is unproblematic. (h) Displays a far-field holographic image which was taken without an objective and projected onto a screen.

5.4 Further research direction

To realise the technologies that have been developed here, there is a post-doc working full-time on developing the optics necessary to view objects with the light-sheet HMSs.

5.5 Conclusion

We have created a platform to create light-sheets for LSFM from HMSs. This platform solves multiple problems with the traditional LSFM design, most notably reducing the objective lenses needed to one and simplifying the optical setup and alignment.

5.6 Contribution

I designed the holograms, ran the simulations, fabricated all of the samples, and performed all of the experiments.

Chapter 6

Millimetre wavelength range holograms

This chapter details a HMS platform for the millimetre wavelength range. Here, we planned to take the successful visible range FHMS platform and translate it to the millimetre wavelength range.

6.1 Concept

The millimetre wavelength range is vital for applications in broadband telecommunications (e.g. 5G) [92, 93, 94], radar (e.g. weapons systems, terrain monitoring, cloud radar and security screening) [95, 96, 97, 98, 99, 100], radiometry (e.g. earth resource studies, cosmic background) [101, 102, 103, 104, 105], and magnetic resonance (e.g. fusion heating and diagnostics, electron spin resonance and dynamic nuclear polarisation) [106, 107, 108, 109, 110, 111, 112]. It offers a compromise between the microwave and the visible/infrared wavelength ranges, exhibiting comparatively low atmospheric attenuation (relative to microwave systems) but maintaining a higher imaging resolution and offering higher bandwidths [96, 112]. Traditionally, when the functionality of millimetre wavelength range equipment requires enhancing or extending, e.g. to modify a 4G base station antenna, it must be replaced, which is expensive and wasteful. Because of this, the ability to modify, or enhance, the EM properties of a device by retrofitting it with a patch is an extremely attractive idea.

As such, researchers have conducted MS research in the gigahertz and terahertz wavelength ranges, creating both significant proposals and experimental results with applications in lensing

[113, 114, 115], sensing [116, 117], tunable response [118, 119, 120, 121, 122], cloaking [123, 124, 125], controlling phase and amplitude [126, 127], absorbers [128], and polarisation conversion devices [129]. Progress has also already been made on rigid HMS designs with the creation of a frequency multiplexed transmission HMS [130], and a broadband transmission vortex generation HMS [131] devices.

A diagram displaying the use case of a flexible HMS patch is shown in figure 6.1. Here, a small section of the FHMS has been applied to a tow attachment to alter its radar response.

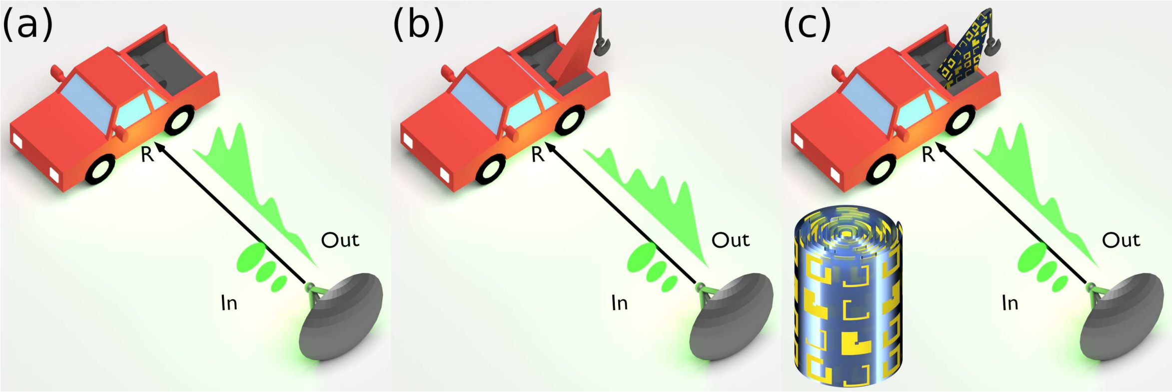

Figure 6.1: An illustration to demonstrate the use of a millimetre wavelength FHMSs. Here, the incident millimetre wavelength radiation from the antenna is directed at the vehicle. The same antenna then collects this reflected signal and plots it against time. (a) The antenna detects the truck without a tow attachment. (b) The truck with tow attachment changes the reflected signal detected by the antenna. (c) A MS is conformed to the tow attachment of the truck and makes it appear to the detector like the truck does not have a tow attachment. A roll of the flexible HMS is shown in the bottom of (c).

6.2 Meta-atom design

The meta-atoms were designed to operate at 94 GHz in reflection and comprise three layers, similar to the visible light range design, which improves the conversion efficiency over a single layer. The upper layer is patterned with metallic c-ring structures, the middle layer is a dielectric spacer, and the lower layer is a reflective backplane. The resonances in the c-ring occur because of their geometry and not because of plasmons. This effect is described further in chapter 1. This meta-atom is shown in figure 6.2.

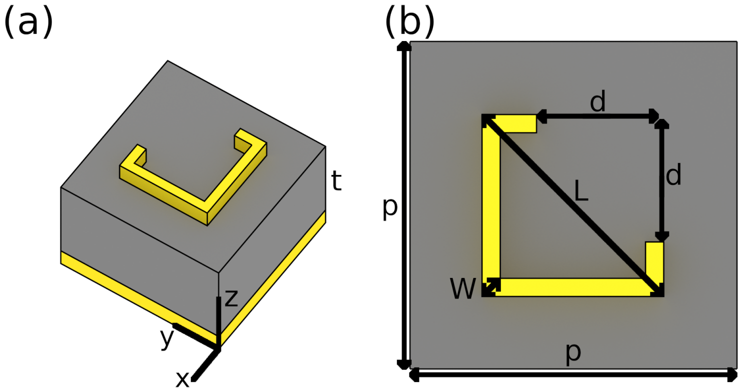

Figure 6.2: (a) A diagram of the unit cell structure of a c-ring. The spacing between the c-ring and backplane is denoted as t. (b) The same unit cell as seen from the top. The pitch is defined as p, the c-ring is centred, the parameters L, d, and W are defined as in the diagram. The incident light is polarised along the x axis and converted to the y axis by the c-ring.

The unique meta-atoms were designed to be excited by incident horizontally linearly polarised (HLP) and emit vertically linearly polarised (VLP) light with a phase-shift in the range $0 \rightarrow 360$ degrees, which was tailored by adjusting the exact dimensions (L, d, and W) of the c-ring rather than rotating them.

We designed the unique meta-atoms with the CST Microwave Studio simulation package by sweeping through the relevant parameters for a standard c-ring design [113, 132, 133, 134], which are shown in figure 6.2. From these simulations, a parameter lookup table was created, which maps a specific shape to the desired phase-shift. From this, the meta-atom which emits VLP light with the highest efficiency can be selected.

To reduce the computational and design effort of these simulations, we quantised the phase into 30 degree increments. Consequently, only twelve unique meta-atoms were required to cover the $0 \rightarrow 360$ degree range, which is a standard quantisation level for HMSs [11, 33, 72, 78, 135]. However, this requirement can be reduced further to a six meta-atom library through a symmetry argument, as the corresponding meta-atom parameters for the phase range of $180 \rightarrow 360$ degrees are identical to those for $0 \rightarrow 180$ degrees but flipped through the x axis (as defined in figure 6.2). The meta-atom pitch, p, further limited the bounds of the parameter space. p needs to be kept sub-wavelength to avoid exciting high diffraction orders, which limit the efficiency [11]. Furthermore, if p is too small, the meta-atoms strongly couple, which in turn requires modelling the entire HMS and is extremely computationally expensive.

For the CST simulations, we used unit cell boundary conditions (periodic not Floquet) for the x and y axes and open boundary conditions for the z axis. Perfectly matched layers (PMLs) and scattering boundary conditions were not used. The simulation area along z was determined by the near-field imaging distance. The mesh was automatically generated according to the structure size and the boundary conditions, this is displayed in figure 6.3 for a representative meta-atom. The input electric field was HLP (along the x axis) and travelling in the $-z$ direction. The output electric field was VLP (along the y axis) and travelling in the z direction. The electrical conductivity of the gold was taken as 45.61 MSm^{-1} and the permeability was taken as $\mu = 1$ from the standard CST material properties library. With this in mind, we designed suitable meta-atoms for two implementations, a rigid design with a silicon spacing layer and a flexible design with PMMA as a spacing layer. The fabrication is discussed in chapter 3. In both cases, the thickness of both the metallic c-rings and of the reflecting backplanes was set at 200 nm. Ideally, the thickness of the dielectric spacer should be chosen with an optical thickness approaching $\lambda/4$. However, due to experimental constraints, we designed the meta-atoms for a low-loss silicon sample of thickness, $t = 115$ μm and a commercially available sheet of PMMA with thickness $t = 400$ μm. For the silicon we used $\epsilon = 11.670 + 0.004j$ (from the CST material properties library). The permittivity for the PMMA was taken as $\epsilon = 2.200$ [136].

The phase-shift and amplitude for each unique meta-atom is shown in figure 6.4, and the parameters for these are displayed in tables 6.1, 6.2, 6.3, and 6.4. Here, the cut-out side dictates the orientation of the empty corner. An empty corner on the left-hand side, an example is shown in figure 6.2, is labelled with a left. Only the first six meta-atoms are shown as the subsequent six are identical to the first, but with the cut-out side flipped (labelled with a right).

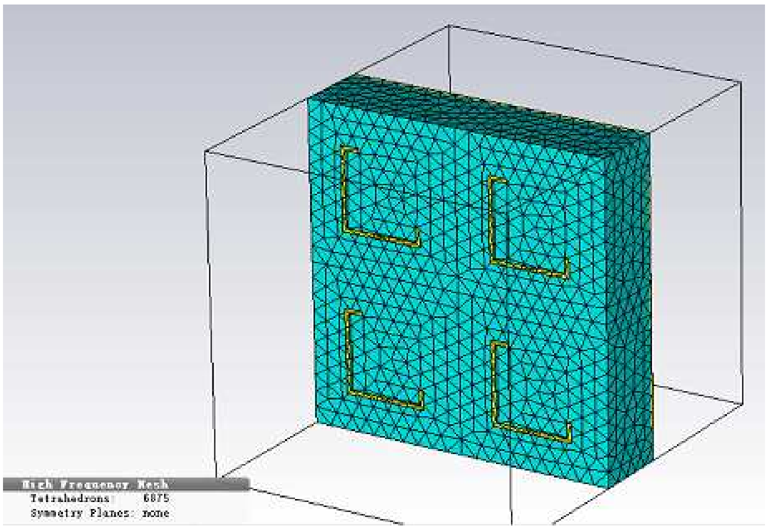

Figure 6.3: An illustration of the mesh used to simulate the meta-atoms in CST.

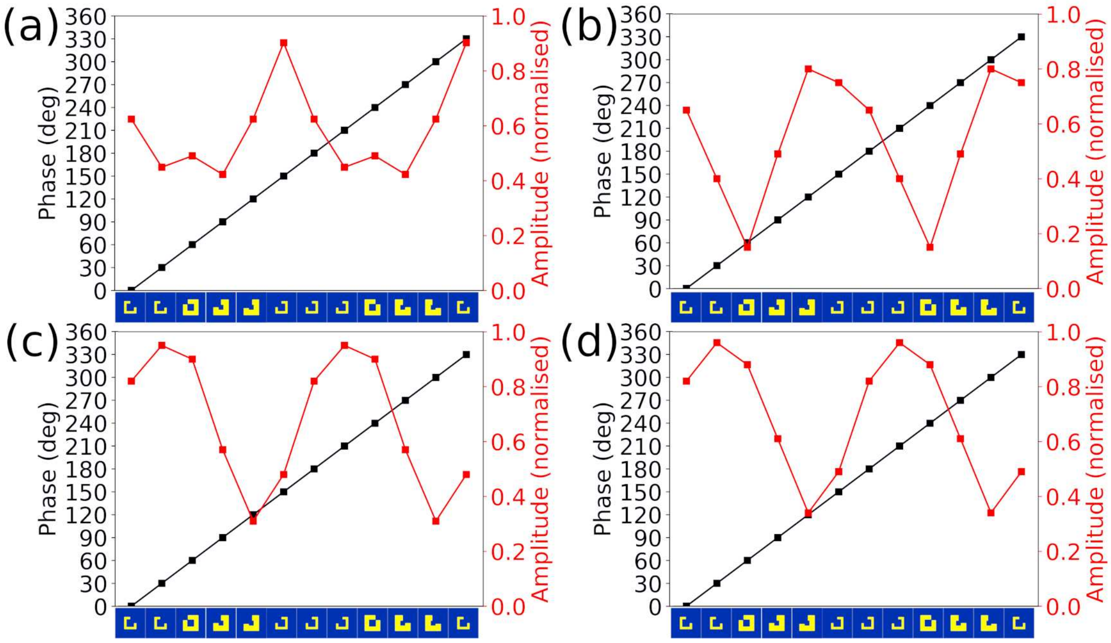

Figure 6.4: Simulated phase-shift and normalised amplitude for each meta-atom at $\lambda = 94$ Ghz where the meta-atom designs are gold on silicon with (a) p =450 μm and (b) p =650 μm, (c) gold on PMMA with p =800 μm, and (d) copper on PMMA with p =800 μm. The illustrated meta-atom are quantised into 30 degree increments. The meta-atom pictures are just for illustration and do not necessarily represent the actual meta-atoms. They represent a typical set of meta-atoms as generated with the same method but with different L, d, W, and cut-out sides.

The amplitude values of the meta-atoms are mostly above 50%. The low amplitude values of some meta-atoms derive mostly from the requirement to avoid a strong coupling between meta-atoms and from the non-ideal thickness of the dielectric layers. Both these limitations can be removed by simulating in-full the coupling of differently shaped meta-atoms, and using different dielectric spacers.

Table 6.1: **Meta-atom parameters for gold c-rings with a pitch of 450 μm on silicon**

Phase-shift	L	d	W	Cut-out side
0.0	400.0	215.0	80.0	right
30.0	500.0	155.0	95.0	left
60.0	500.0	150.0	200.0	left
90.0	470.0	36.0	50.0	right
120.0	500.0	102.0	80.0	right
150.0	500.0	122.0	80.0	right

Table 6.2: **Meta-atom parameters for gold c-rings with a pitch of 650 μm on silicon**

Phase-shift	L	d	W	Cut-out side
0.0	350.0	128.3	60.0	right
30.0	350.0	134.6	60.0	right
60.0	450.0	102.0	120.0	left
90.0	450.0	159.9	150.0	left
120.0	450.0	177.2	150.0	left
150.0	350.0	124.9	60.0	left

Table 6.3: **Meta-atom parameters for gold c-rings with a pitch of 800 μm on PMMA**

Phase-shift	L	d	W	Cut-out side
0.0	550.0	60.0	60.0	left
30.0	550.0	60.5	60.0	left
60.0	550.0	79.0	80.0	left
90.0	550.0	83.5	100.0	left
120.0	550.0	94.2	100.0	left
150.0	550.0	206.2	40.0	right

Table 6.4: **Meta-atom parameters for copper c-rings with a pitch of 800 μm on PMMA**

Phase-shift	L	d	W	Cut-out side
0.0	550.0	60.0	60.0	left
30.0	550.0	79.0	60.0	left
60.0	550.0	82.5	80.0	left
90.0	550.0	116.8	80.0	left
120.0	550.0	217.0	80.0	left
150.0	550.0	30.5	40.0	right

We were concerned that the adjacent meta-atoms would still couple in these designs. Were the meta-atoms coupling, a meta-atom supposed to give a particular phase-shift (e.g. 30 degrees) adjacent to a meta-atom supposed to give a different phase-shift (e.g. 120 degrees) may give an entirely different phase-shift (e.g. 15 degrees). As such, the meta-atoms could not be considered independent and the whole HMS would need to be simulated. Furthermore, this expensive simulation would have to be performed every time a different holographic image was required. As a result, we chose to study the interaction between meta-atoms. The simplest method to do this was to take each unique meta-atom (as given in tables 6.1, 6.2, 6.3, 6.4) and simulate the phase-shift value resultant when the pitch is varied. If changing the pitch alters the phase-shift value, then the meta-atoms must be coupling in the HMS. If the phase-shift value remains constant, then the meta-atoms are likely not coupling. The results for these simulated tests are displayed in figure 6.5.

In figure 6.5, it can be seen that the meta-atoms are significantly coupling in the 450 μm pitch case but not so much in the other cases. As a result, this thesis drops the 450 μm pitch case and concentrates on the larger pitch cases. Furthermore, it now solely concentrates on the gold design until later in this chapter where it reintroduces the copper design.

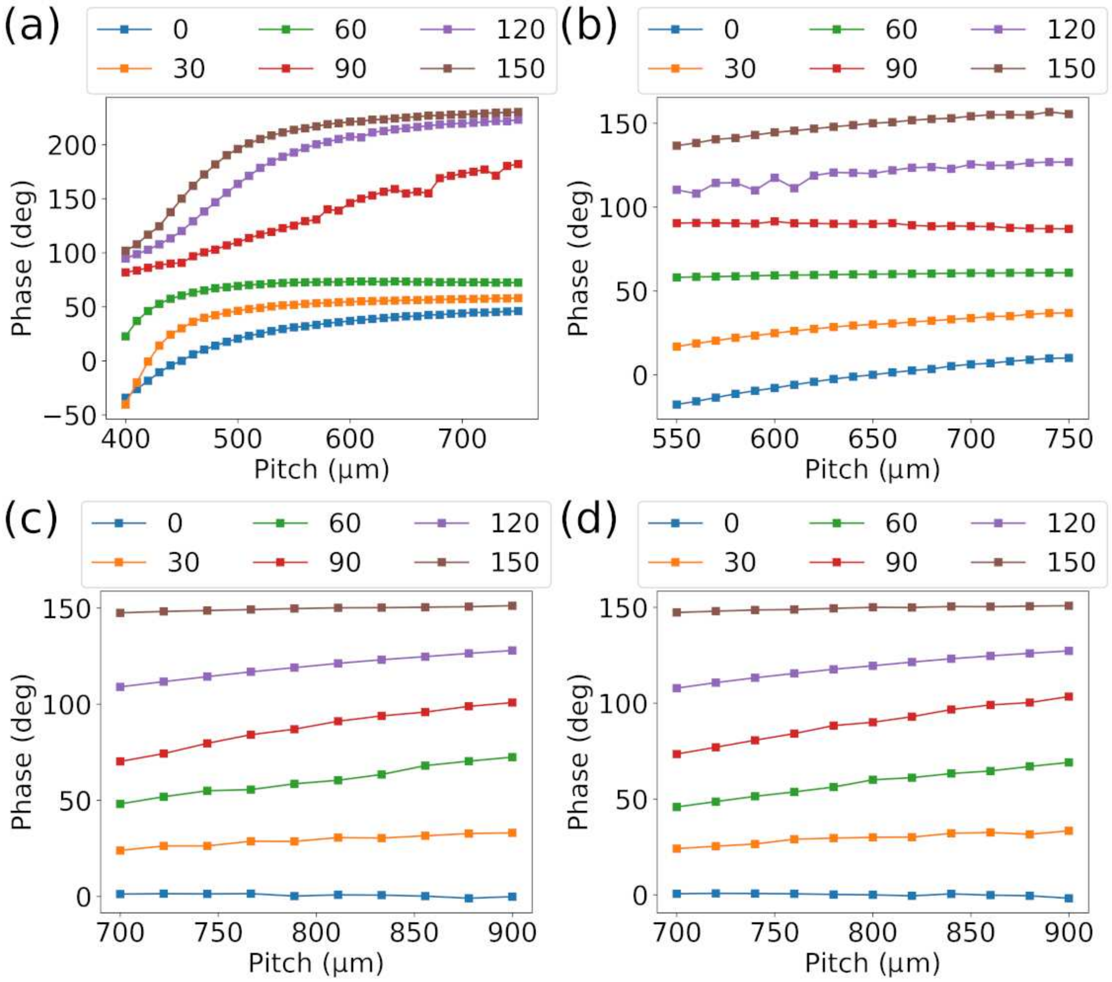

Figure 6.5: Simulated phase-shift of each unique meta-atom vs the pitch of the meta-atom at $\lambda = 94$ Ghz. The meta-atom designs were for (a) gold on silicon with an intended pitch of p =450 μm, (b) gold on silicon with an intended pitch of p =650 μm, (c) gold on PMMA with an intended pitch of p =800 μm, (d) copper on PMMA with an intended pitch of p =800 μm.

6.3 Hologram design

For the hologram retrieval, the full RS propagator and the GSA, as detailed in chapter 2, was used.

A constraint for the HMSs was the largest size of HMS that could be fabricated. This constraint existed because the EBL time to define meta-atoms increases as a function of the area. A further constraint came from the RIE procedure used to transfer the c-rings into the metal layer, as the sample area was limited. As a result of these constraints, the upper limit on the sample size was around 25 × 25 mm^2, which is $\approx 10\lambda$ across. For context, the visible light nanorod HMSs found elsewhere in this thesis were typically 1000λ across. With such a small sample area the spatial resolution of the HMS was limited, and thus only broad low-resolution features could be created with it. With this in mind, a hologram to create a focused spot reflected at a predetermined angle when illuminated at normal incidence was designed. In the hologram design, a Gaussian intensity distribution for the incident beam (FWHM equal to 12.5 mm) with a flat phase front was used, following the experimental source. The parameters detailing the design of the HMS are in tables 6.5 and 6.6 for the rigid and flexible implementations respectively.

Table 6.5: **Hologram parameters for the rigid design**

Parameter	Value
Hologram pixels	38×38
Holographic image pixels	200×200
Hologram pixel pitch	650 μm
Holographic image pixel pitch	0.5 mm
Holographic image offset in x, y, z	0, 0, 125 mm
Wavelength	630 nm

Table 6.6: **Hologram parameters for the flexible design**

Parameter	Value
Hologram pixels	31×31
Holographic image pixels	200×200
Hologram pixel pitch	800 μm
Holographic image pixel pitch	0.5 mm
Holographic image offset in x, y, z	0, 0, 125 mm
Wavelength	630 nm

The holographic image was placed 125 mm from the hologram, which corresponds to $\approx 40\lambda$. This distance is large enough that the approximations made to find the RS propagator, equation 2.9 are valid. Were this distance shorter or λ larger, however, the polarisation could not be neglected and the full Helmholtz-Kirchoff formulation, equation 2.4, should be used.

6.4 Fabrication and experiment

To fabricate the samples, the steps in chapter 3 were followed for both the rigid and the flexible implementations. Images of the fabricated rigid and flexible samples are shown in figure 6.6.

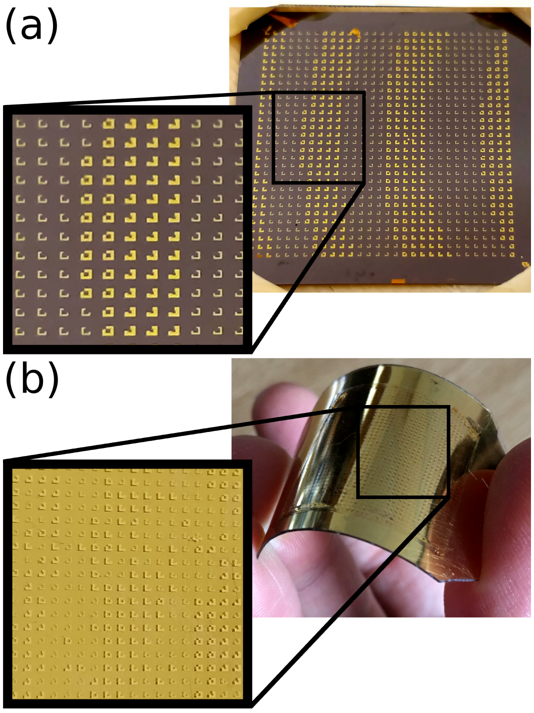

Figure 6.6: Photographs, with expanded inserts, displaying the fabricated (a) rigid and (b) flexible implementations of the millimetre wavelength range HMS.

In both cases, the quality of the fabrication is excellent. Furthermore, the flexible implementation is capable of withstanding a tight radius of curvature with no apparent ill effects.

To verify the fabricated samples in an experiment, we used the setup described in figure 6.7.

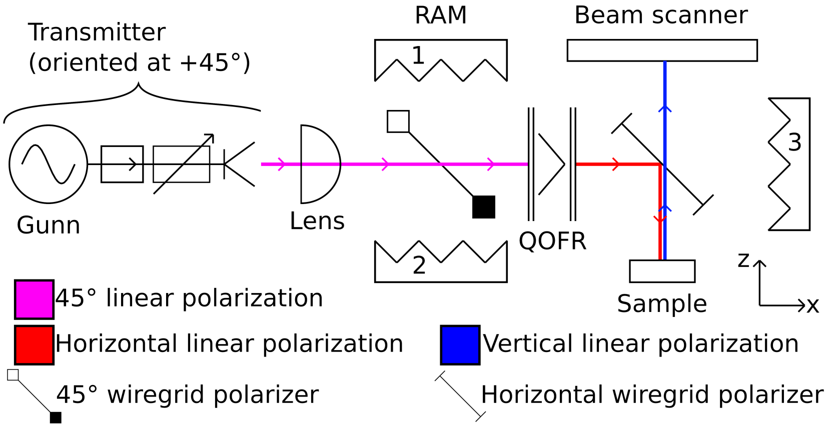

Figure 6.7: A schematic of the experimental setup used to collect the holographic images.

Radiation at a wavelength of $\lambda = 3.19$ mm (94 GHz) was emitted by a millimetre wavelength

Gunn oscillator into a waveguide isolator, followed by a variable attenuator, which was coupled to free space via a corrugated feedhorn. The beam was collimated by a suitable lens, creating a beam with a Gaussian intensity profile and an approximately planar phase front at the plane of the sample. The beam then passed through a combination of a wire grid beam splitter and a quasi-optical Faraday Rotator (QOFR) to set the beam into the HLP and remove any unwanted radiation by dumping it into two blocks of radar absorbing material (RAM) (RAM 1 and RAM 2). The beam then passed into a polarising beam-splitter, which directed HLP light onto the HMS at normal incidence, and dumped unconverted VLP radiation into RAM 3. The HMS created a holographic image with rotated VLP, which reached the detector unimpeded by the wire grid polariser. The detector was a short section of single mode waveguide mounted on a motorised stage and coupled to a heterodyne receiver. The intermediate frequency (IF) signal from the receiver was measured with a spectrum analyser. The beam scanner recorded the power as a function of the spatial position over an area of 100×100 mm^2 at a distance of 125 mm from the HMS.

The results are displayed in figure 6.8, where the image from a simple polarisation rotation mirror is shown to find the size and quality of the collimated beam. In figure 6.8(b-e), the deflected and focused holographic images, in simulation and experiment, are shown, which are in good agreement. The small differences are due to the coupling between meta-atoms, fabrication errors (e.g. variation and scratches in the PMMA spacer), and residual interference from stray reflections from the experimental setup.

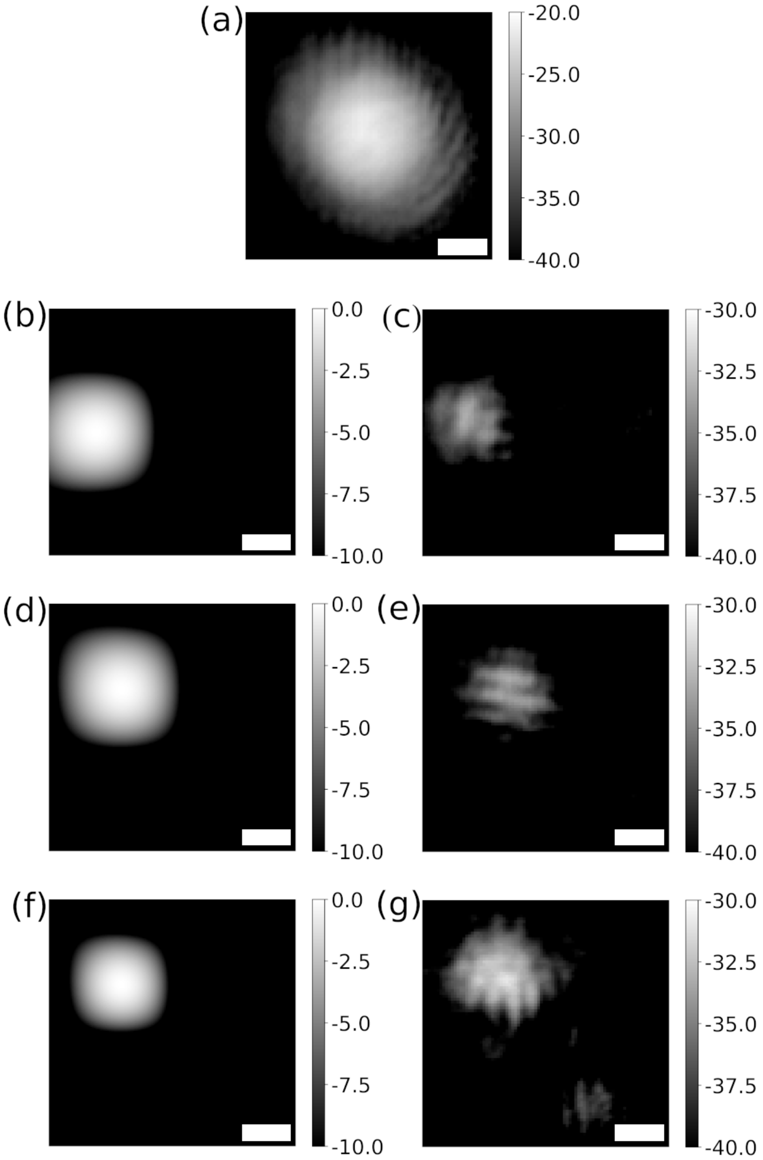

Figure 6.8: (a) Displays the experimental image given by a polarisation rotation mirror, in this case from HLP to VLP. This represents the reference beam with rotated linear polarisation. (b) Simulated and (c) experimental holographic images for the rigid HMS implementation deflected to one side. (d) Simulated and (e) experimental holographic images for the rigid HMS implementation deflected to a corner. (f) Simulated and (g) experimental holographic images for the flexible HMS implementation deflected to a corner. All units are in dBm. The scale bar is the same for each image and represents 20 mm.

6.5 Further research direction

We aim to expand the size of our fabricated FHMSs. The main benefits of this are greater control over light with higher k vectors, and the ability to control the optical response of larger areas.

The two areas of fabrication which constrain the maximum size of the FHMSs are the EBL and the RIE steps. The first fix is to move from EBL to UV lithography. Changing the RIE step, however, requires moving from a dry RIE step to a wet-etch. Gold can be removed with aqua regia; however, gold is expensive and does not exhibit significantly better plasmonic properties than copper in the millimetre wavelength range. Accordingly, this thesis investigates copper meta-atoms, where the wet-etch is performed with $FeCl_3$.

6.5.1 Fabrication

To fabricate these new devices, a similar procedure to the rigid devices outlined in chapter 3 was followed, where the silicon was substituted for PMMA and the gold for copper. This procedure is outlined in detail below.

1. Cleaned the 400 μm thick PMMA dielectric spacer by submerging it in IPA under sonication at room temperature for 5 minutes.
2. Baked for 20 minutes at 90 °C to remove most of the native scratches in the PMMA, which are typically present in commercially available sheets, by allowing it to re-flow.
3. Evaporated, via electron beam evaporation, 2 nm of nichrome then 200 nm of copper onto the front of the PMMA to become the c-ring meta-atoms. This layer was thick enough to scatter the light without wasting too much copper.
4. Spin-coated a thin layer of SU-8 to act as the EBL resist, this was SU-8 2000.5 and Cyclopentanone 1:1 at 2000 rpm for 1 minute. This recipe was chosen to be thick enough to act as an effective mask but with the minimal limiting of the UV lithography resolution.

5. Baked for 1 minute at 60 °C, then 4 minutes at 90 °C.
6. UV lithography step using an EVG for 45 seconds with a bulb power of 350 watts.
7. Baked for 2 minutes at 90 °C as a post-exposure bake to cross-link the exposed c-rings.
8. Developed the SU-8 resist with EC solvent for 1 minute at room temperature.
9. Wet-etch in a solution of DI water and $FeCl_3$ (100:1) until the unmasked copper was fully removed.
10. Evaporated, via electron beam evaporation, 2 nm of nichrome then 200 nm of copper onto the back of the PMMA to act as a reflective backplane. This layer was thick enough to efficiently reflect the light without wasting too much copper.

The fabricated large area, 100×100 mm^2, HMS is shown in figure 6.9 with an expanded cut-out. The patterning is reasonably uniform across the sample, and the individual meta-atoms contain few fabrication defects. There are visible defects at the edges of the sample underneath the meta-atoms from SU-8 that seeped underneath the HMS during the spin-coating step. However, this should not affect the performance of the device as this SU-8 layer is thin compared to the thickness of the PMMA (400 μm). There are also similar visible defects which originate from scratches in the PMMA.

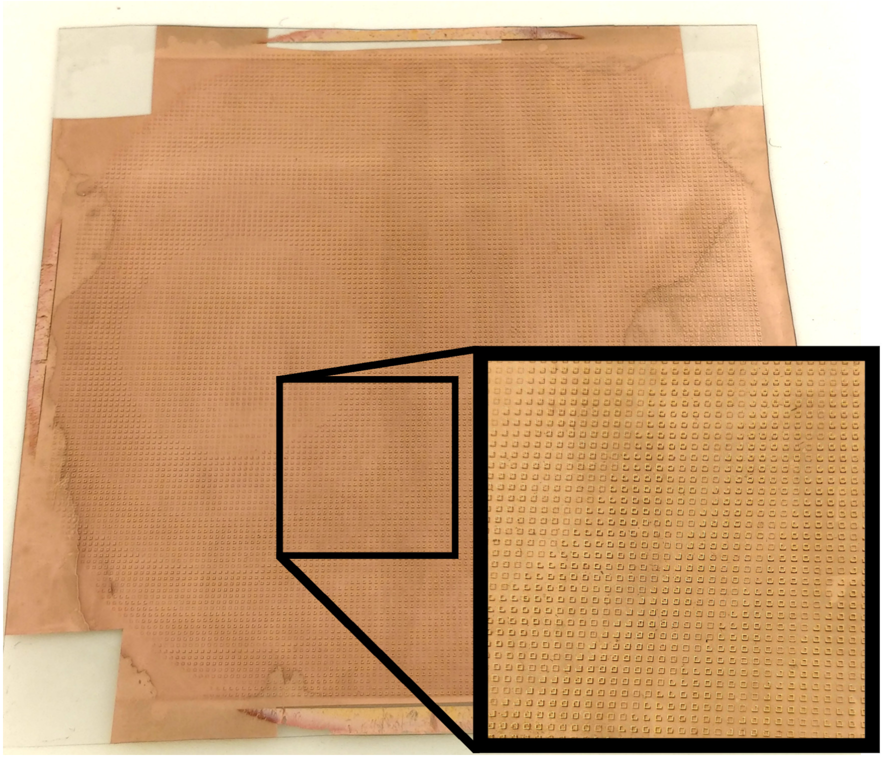

Figure 6.9: A large area, 100×100 mm^2, HMS for the millimetre wavelength range with expanded cut-out.

6.6 Conclusion

We have created a platform for HMSs at a wavelength of $\lambda = 3.19$ mm with both rigid and flexible implementations. This flexible implementation could be exploited using smart HMS patches to enhance and extend existing millimetre wavelength equipment for applications in EM shielding and antennas. Furthermore, critical steps have been made to scale-up the fabrication to large areas.

6.7 Contribution

I designed the holograms, ran the simulations, and fabricated all of the samples. Jing Ma designed the meta-atoms and helped run the experiments. Robert Hunter and Duncan Robertson created the experimental setup.

Chapter 7

Future perspective

This chapter details some incomplete work, in particular, to create a platform for holography using incoherent light, to multiplex near-field holograms in their surface topography, and to create a tunable multi-layer HMS.

7.1 Holography with partially incoherent light

Coherent light is typically essential for the operation of HMSs [3, 69], however, we became interested in expanding the usefulness of HMSs by enabling them to operate with partially incoherent illumination. In particular, we were interested in increasing the tolerance of HMSs to spatial incoherence as temporal coherence can be addressed with optical filters and more complex meta-atom designs [8, 64]. Optical filters can remove the unwanted temporal frequencies. The more-complex meta-atom designs, instead, create unique holograms for different illumination wavelengths, which can effectively solve the temporal coherence problem.

7.1.1 Concept

This work aimed to enable HMSs to operate with spatially incoherent light by splitting the HMS into smaller sub-pixels, as shown in figure 7.1. Each sub-pixel would only address one point in the holographic image, and thus the spatial coherence is only required over the length scale of the sub-pixel.

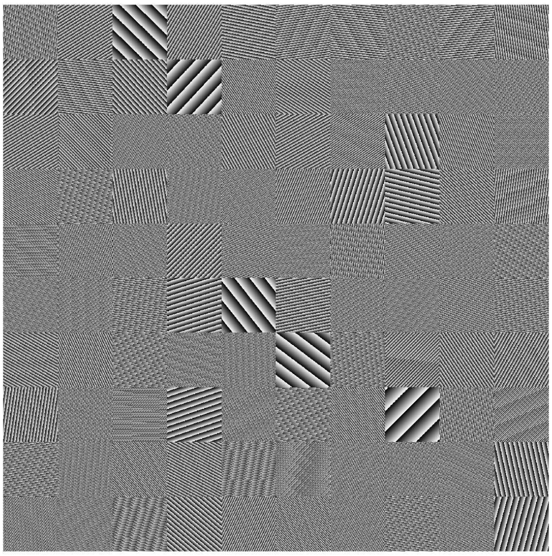

Figure 7.1: Holographic phase distribution, with a resolution of 2000×2000, split into sub-pixels with a resolution of 200 × 200. Each sub-pixel deflects the incident beam to a different point in the holographic image.

7.1.2 Phase reconstruction algorithm

The standard phase reconstruction approach via the GSA, detailed in chapter 2, does not produce a hologram according to the design outlined above. Therefore, a new phase reconstruction algorithm was created.

This algorithm starts with user input for the number of sub-pixels in the hologram and their pitch. A feature of the size of each sub-pixel is that larger sub-pixels produce a more confined spot in the holographic image because they exhibit a larger NA. The coordinate of each sub-pixel is given by its centre and is labelled as x_s, y_s, z_s.

Next, a guess is made for the optimal resolution of the target. If the target resolution is too high, there will be too few sub-pixels to create each pixel in the target image. If the target resolution is too low, there will be too many sub-pixels, and some target pixels will have to be replicated or unused. Replicated holographic image pixels lead to brightness uniformity problems in the resultant holographic image, and unused pixels lower the overall efficiency of the hologram.

To improve the guess for the target resolution, a coarse grid, as shown in figure 7.2(a), is imposed over the target. If there are fewer sub-pixels than intersections between the grid corners and the target image (which are marked with crosses), the pitch of the grid is decreased, as shown in figure 7.2(b). This step is iterated until the correct grid spacing is found.

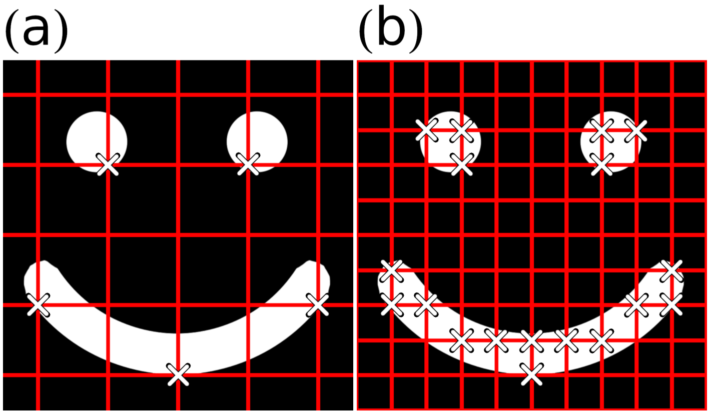

Figure 7.2: Grids with different periods which intersect (a) 5 and (b) 18 times respectively. The intersections are marked with crosses.

The output of this procedure is a list of coordinates for points in the target image that need to be created, labelled x_t, y_t, z_t.

For each sub-pixel, the phase required to deflect light to the target image x_t, y_t, z_t coordinate is found using equation 5.1, and the results combined to build a hologram (e.g. figure 7.1). To better replicate a common feature of holograms, the order that the sub-pixels are chosen is randomised. As a result, removing the left half, for example, does not remove the left half of the holographic image and instead lowers the resolution. The full algorithm is described in algorithm 3.

Algorithm 3 Helicity multiplexing phase reconstruction algorithm

```
Create a list of the coordinates for each sub-pixel.
Randomise the order of sub-pixels in the list.
Calculate the ideal target resolution and create a list of the coordinates of each target pixel.
Calculate the phase gradient required in each sub-pixel to create the target image pixel using equation 5.1.
Return the hologram phase
```

To test the phase reconstruction algorithm, a hologram according to the parameters displayed in table 7.1 was created. The recovered holographic image was then propogated in simulation (shown in figure 7.1) with a FFT, which results in the holographic image displayed in figure 7.3(a). The corresponding experimental image is shown in figure 7.3(b). Both the simulation and the experiment were conducted with coherent light because we did not have the equipment to generate light with variable spatial coherence on the scale of the HMS.

Table 7.1: **Incoherent resistant holographic image parameters**

Parameter	Value
Hologram pixels	2000×2000
Holographic image pixels	150×150
Hologram pixel pitch	300 nm
Holographic image pixel pitch	0.33 mm
Hologram sub-pixel size	100×100
Holographic image offset in x, y, z	0.0, 0.0, 0.5 m
Wavelength	630 nm

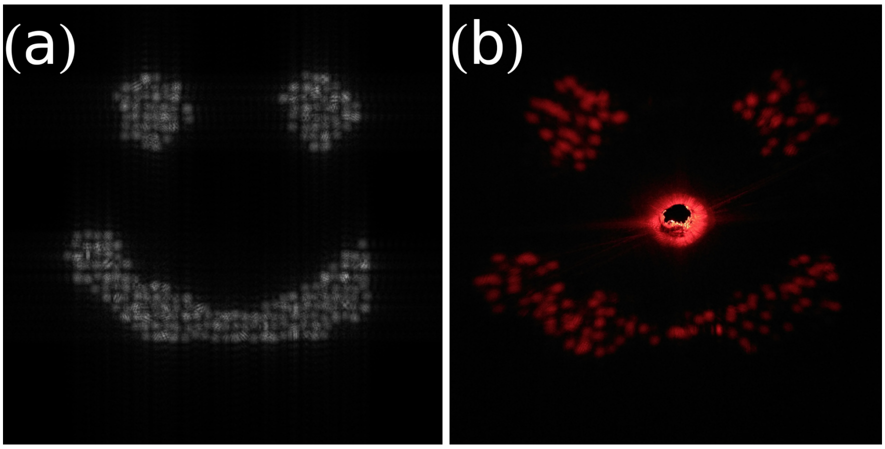

Figure 7.3: Images from (a) simulation and (b) experiment of the hologram shown in figure 7.1(a). Both the simulation and experiment used spatially and temporally coherent illumination. There are slight differences between the two images as the incident beam was smaller than the HMS meaning that not all of the HMS is contributing to the holographic image and (b) was photographed off-normal.

7.1.3 Further research direction

In the future, the response of the HMSs to incoherent light will be tested. This could be done using the cross-correlation coefficient (comparing the resultant image with the target using equation 4.1) as the size of the sub-pixels are varied on a scale comparable with the coherence of the source. We expect that larger sub-pixels will degrade faster than smaller ones in this test, but will produce higher resolution holographic images.

There are also improvements which could be made to the phase recovery algorithm. First, the algorithm can only recover binary holographic images. Because the intensity distribution of many holographic images are greyscale, it would be useful if this could be incorporated. Second, it uses identically sized sub-pixels. Because, in typical images, there are both high and low-resolution features, using sub-pixels of different sizes could allow for creating holograms with both of these features.

In the longer term, this work could be used as a base to expand the applications for holograms by enabling them to use sources other than lasers, e.g. the sun.

7.2 Near-field metasurface multiplexing

Multiplexing holograms allows for post-fabrication tuning of the holographic image, e.g. by stretching the HMS [49, 50], and changing the helicity of the incident light [11, 40, 45]. Consequently, tunable HMSs could enable new optical components, optical switches, and sensors.

During the investigations into non-flat HMSs, a platform to spoil a holographic image by changing the surface topography was created. However, this platform could be extended to tune between two unique, high-quality holographic images if they were created in the near-field.

The near-field removes some of the physical constraints of traditional far-field holography, e.g. holograms can evolve with distance. Because of this, the near-field has been used for multiplexing [49, 50], and encoding three-dimensional holographic images in a two-dimensional HMS [10].

The next section explores multiplexing holographic images with the surface topography in the near-field.

7.2.1 Holographic image multiplexing with the surface topography

To examine this multiplexing, in simulation, a hologram using the GSA and the full RS propagator was designed. The hologram parameters are displayed in table 7.2 for the two substrate shapes, a convex and concave cylindrical HMS with radii of curvature of ±0.5 mm.

These holograms were multiplexed by taking the mean value of every complex pixel in both recovered holograms, as in chapter 5 [50].

Table 7.2: **Curvature multiplexing holographic image parameters**

Parameter	Value
Hologram pixels	2000×2000
Holographic image pixels	250×250
Hologram pixel pitch	300 nm
Holographic image pixel pitch	5 μm
Holographic image offset in x, y, z	0, 0, 2 mm
Hologram radius of curvature along the x direction	±0.5 mm
Wavelength	630 nm

The resultant holographic images are shown in figure 7.4. Here, it can be seen that two different holographic images have been multiplexed with minimal overlap and a dependence on the surface topography. Furthermore, this effect is present far enough from the hologram to be verified in an experiment and potentially realised in real-world applications.

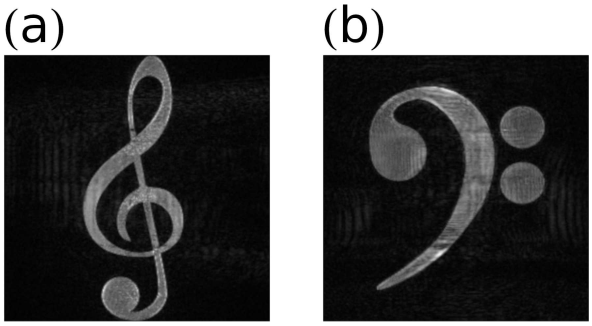

Figure 7.4: A holographic image produced from two different cylinders where the radius of curvature is (a) -0.5 mm and (b) 0.5 mm respectively.

7.2.2 Further research direction

The status of this project is that although the simulations are complete, the optical characterisation setup to investigate holographic images close to the HMS needs to be constructed. The setup is relatively simple and will follow the design of the characterisation setup from chapter 5. The realisation for these holograms would be the standard nanorod HMS. Were one to characterise these holograms in an experiment, and they to follow the simulations, they could be mounted to a piezo bender. This could allow for dynamic tuning between two holographic images. Furthermore, this platform could potentially be expanded to produce three distinct holographic images. In the longer term, this work could be applied to couple optical and mechanical effects, e.g. to create an optical microphone.

7.3 Multi-layer tunable holographic metasurfaces

During the effort to create a HMS with a tunable response, two designs for multi-layer HMSs were designed, fabricated, and characterised.

The first application was for refractive index sensing, where a liquid (e.g. a high refractive index oil) would be added to the HMS. This oil would alter the plasmonic resonances supported by the HMS, thus, changing the scattering properties and leading to a visible change in the holographic image. Ideally, the HMS could be designed only to produce the holographic image when wet, which would make the HMS a useful refractive index sensor [137].

The second application was to create a tunable PB element, where an electric field is used to reorient a single nanorod antenna. This would have immediate applications for SLMs, which suffer from spurious diffraction orders as a result of their greater-than-the-wavelength pitch [33].

7.3.1 Multi-layer fabrication

These multi-layer HMSs were fabricated according to the following procedure.

1. Cleaned the glass substrate by submerging it in acetone and then IPA under sonication. Each cleaning step was performed at room temperature and for 5 minutes.
2. Evaporated 100 nm of gold onto the SU-8 to act as the HMS reflective backplane.
3. Spin-coated a thin layer of SU-8 2000.5 (Microchem) to act as the EBL resist at 5000 rpm for 1 minute. The thickness of this layer was 500 nm. This thickness was chosen to create structures with a 400 nm suspended overhang and a 500 nm overall height.
4. Baked for 1 minute at 60 °C, then 4 minutes at 90 °C.
5. Changed the EHT to 30 keV and waited for 2 hours to stabilise.
6. EBL step using a RAITH eLine Plus and the parameters in table 7.3 for the lower level

Table 7.3: **Typical electron beam parameters for the lower layer**

Parameter	Value
EHT	30 keV
Base Dose	5 μC cm^{-2}
Dose factor	15
Working distance	10 mm
Write field size	100 × 100 μm^2
Aperture size	7 μm
Basic step size	2 nm
Area step size	20 nm

7. Performed another write-field alignment, as detailed in the appendix B, to precisely align the lower and upper layers of the write.
8. EBL step using a RAITH eLine Plus and the parameters in table 7.4 for the higher level.

Table 7.4: **Typical electron beam parameters for the upper layer**

Parameter	Value
EHT	2 keV
Base Dose	5 μC cm^{-2}
Dose factor	5
Working distance	10 mm
Write field size	100 × 100 μm^2
Aperture size	7 μm
Basic step size	2 nm
Area step size	20 nm

9. Baked for 2 minutes at 90 °C as a post-exposure bake to cross-link the exposed nanorods.
10. Developed the SU-8 resist with EC solvent (Microchem) for 1 minute at room temperature.
11. Evaporated 40 nm of gold onto the SU-8 to functionalise the HMS.

Writing the top layer of the resist at a low EHT of 2 keV means that the electrons are confined to the upper ≈ 100 nm of the resist. Writing the bottom layer of the resist at a high EHT of 30 keV means that the electrons penetrate from the top of the resist down to the bottom and the gold backplane. As such, by writing two separate layers with different EHT values, multi-layer structures could be written in one EBL step. This is further outlined in the appendix B. Writing two layers in this way requires waiting for a few hours to obtain a maximally stable system after turning on, or altering, the EHT.

It is worth noting that evaporating the gold in the last step creates shadowed regions on the bottom plane of the HMS device, as a result of occlusion from the top. Depending on the intended structure, the exact designs for the top and bottom layers change, which are detailed in their subsections.

7.3.2 Refractive index sensing

Metasurface design

These structures are a multi-layer with rectangular nanorod tops placed on circular pillars. This design had the potential to operate as a tunable holographic element. The top layer was designed as a regular array of rectangles with sides of 800×300 nm^2 and a pitch of 1.2 μm. These two layers are shown in figure 7.5.

The bottom layer was designed as a regular array of circles with a diameter of 200 nm and the same pitch as the nanorods. The bottom layer was designed to be aligned to the centre of each nanorod. The patterned HMS area was designed as 100×100 μm^2 so that it could fit within one

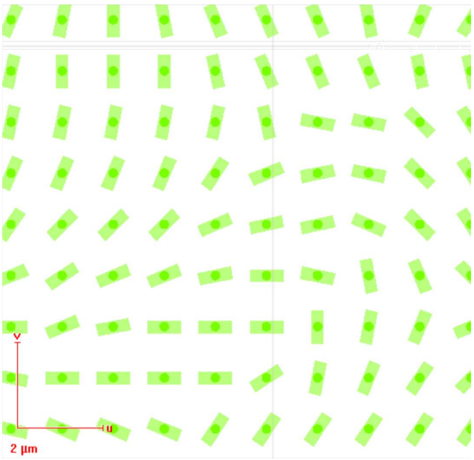

Figure 7.5: A section of the design used to create a suspended nanorod array. The lighter structures are the nanorods and are written on the higher level. The darker structures are the posts and are written on the lower level.

write-field. This small area meant that the stage did not have to be moved between writing the two layers, which negated inaccurate stage movement.

SEM images of the fabricated samples are displayed in figure 7.6.

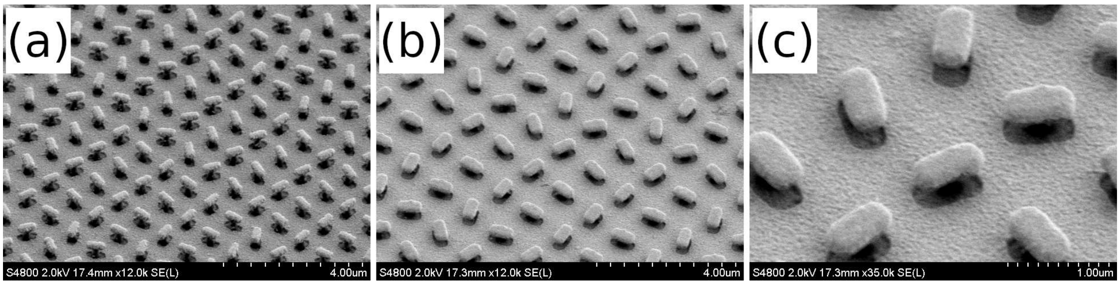

Figure 7.6: SEM images of the nanorod tops suspended over the reflective backplane by a post. (a) Shows a HMS with a pitch of 0.6 μm. (b) Shows a HMS where the pitch is 1.2 μm and (c) shows a close-up of (b).

Characterisation as a refractive index sensor

To characterise the resultant holographic images, the optical setup described in figure 7.7(a) was used. To test the refractive index sensing capabilities of the HMSs at a range of wavelengths, small amounts of a high refractive index oil ($n = 1.517$) were added.

The resulting images are displayed in figure 7.8, which show that in all cases the high refractive

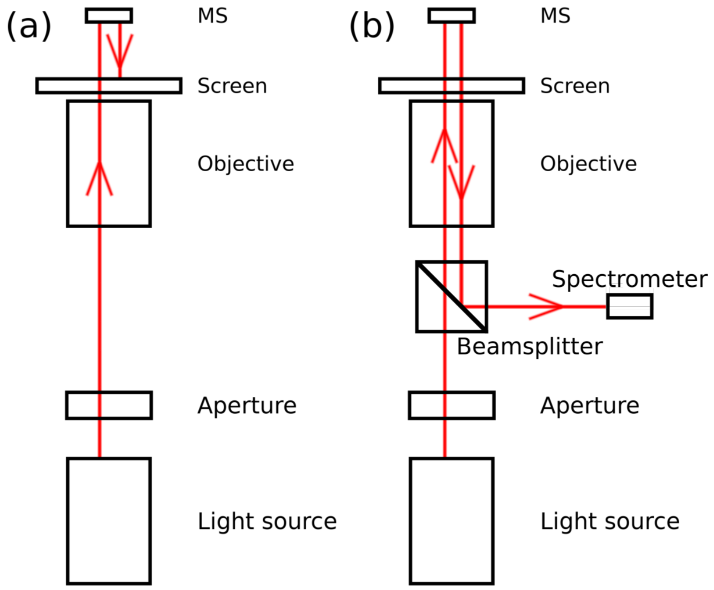

Figure 7.7: The optical setups used to (a) take the experimental photographs (b) collect spectrometer information.

index oil reduces the total intensity of the holographic image. The shorter wavelengths, however, exhibit a slightly more significant effect on the holographic image intensity than the longer ones.

To test if the intensity changes are the result of absorption in the oil, spectra reflected from an unpatterned area of the sample with and without the oil were captured. To capture this spectral information, a modified version of the optical setup with a 50:50 beam splitter, as shown in figure 7.7(b), was used. This beam splitter directed light reflected from the HMS to the collection lens/fibre on an Ocean Optics Spectrometer. The ambient light was removed from the spectrometer readings by first taking a reference without the white light illumination.

The reflected spectra with and without the high refractive index oil are shown in figure 7.9. Figure 7.9 displays that the addition of oil hardly changes the reflected intensity from the simple planar reflective surface. As such, the intensity variation with the addition of the oil is likely related to the interaction with the HMS.

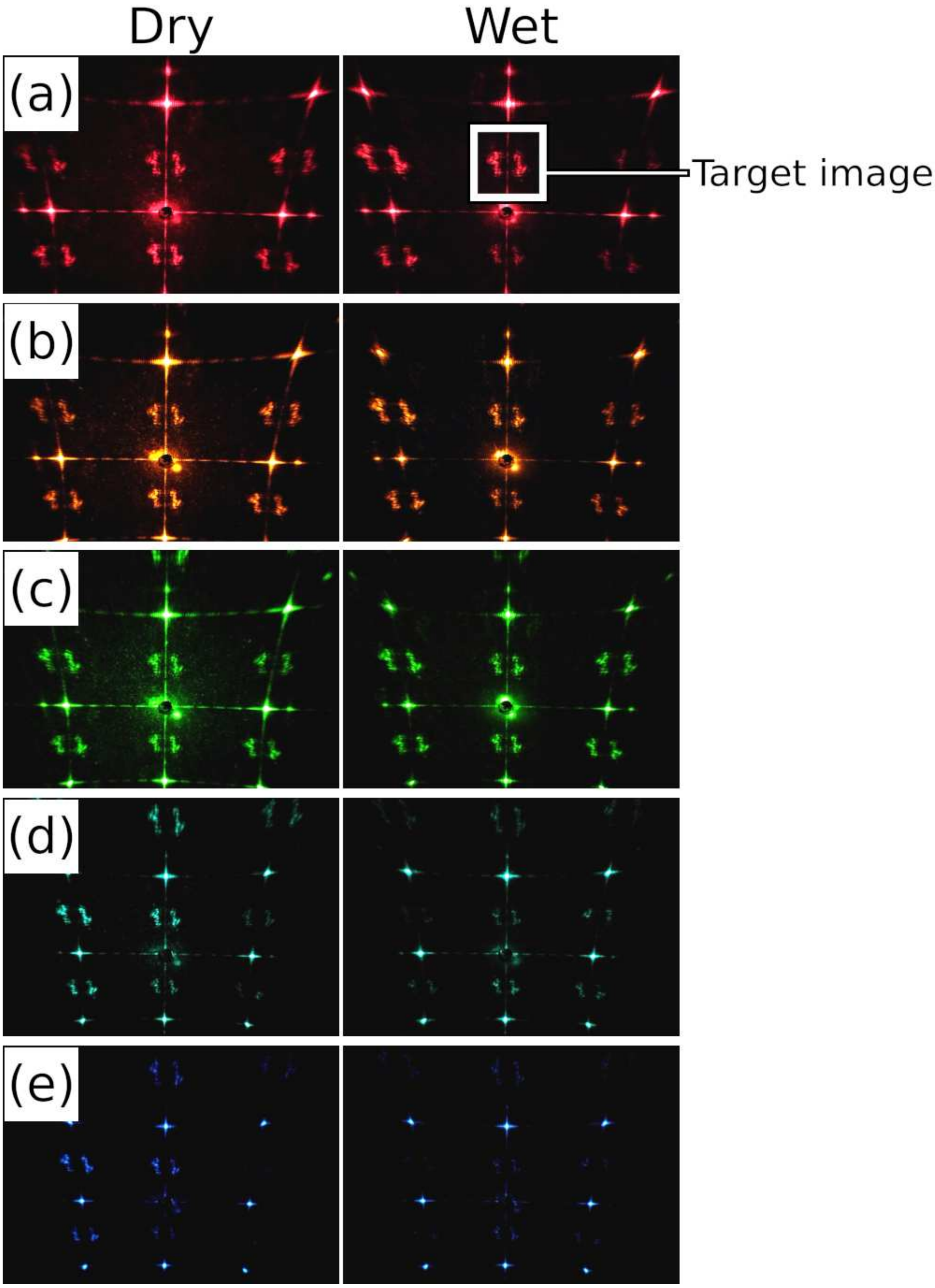

Figure 7.8: Experimental images captured before and after the addition of a high refractive index oil ($n = 1.517$), where the incident wavelength was $\lambda =$ (a) 650 (b) 600 (c) 570 (d) 500 (e) 480 respectively. The target image is highlighted in white in (a). The holographic image is noticeably lower quality than that of others in this thesis because of the small HMS area. The bright spots are diffraction orders and are seen because the pitch of the meta-atoms is greater than the wavelength and the holographic image is seen in multiple orders for the same reason. The images were photographed off-normal.

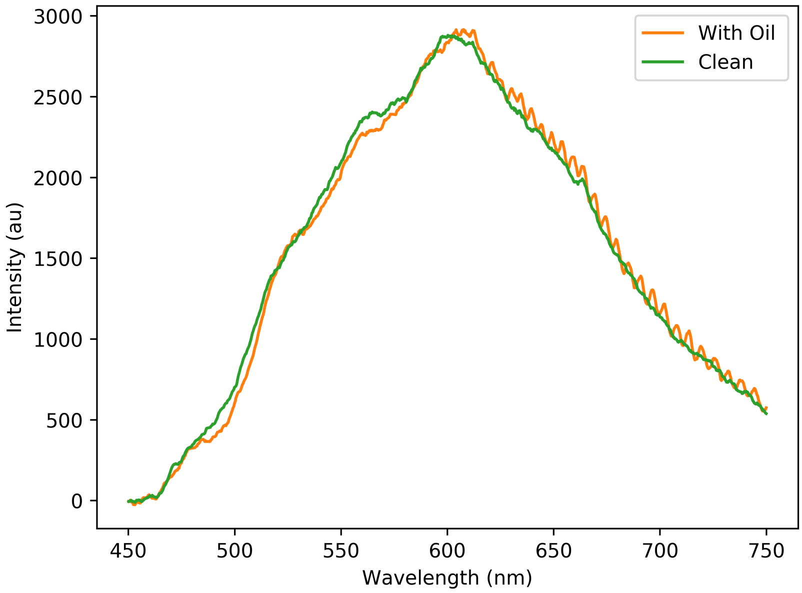

Figure 7.9: Reflection spectra from a 100 nm thick gold layer with and without a high refractive index oil ($n = 1.517$).

7.3.3 Tunable Pancharatnam Berry phase using DC voltage

The aim for these structures was to reorient a nanorod antenna using a direct current (DC) voltage. This would allow the tuning of a HMS after fabrication by reorienting select nanorods. The angle sets, through the PB phase, the phase-shift from the nanorod. Therefore, with circularly polarised light, an array of re-orientable nanorods would function as an improved SLM with a much smaller pixel pitch (a typical SLM pitch is 10 μm). Consequently, the array of re-orientable nanorods would be greatly more efficient than current spatial light modulators as it would avoid the spurious diffraction orders that result from the greater-than-the-wavelength pitch [33]. The proof-of-concept for this design would be to rotate a single nanorod with DC voltage, which is described below.

Mertasuface design

The top layer was designed as a rectangle with dimensions scaling between 2.00×0.22 μm^2 and 0.30×0.22 μm^2. Aligned with the ends of the longest sides of the rectangles, and spaced 0.5 μm away, pointed triangular tips were designed. These triangular tips were connected to large contact pads with dimensions of 17 × 17 μm.

The bottom layer was designed as circles with a diameter 0.14 μm and aligned with the centre of the rectangle top layer so that each rectangle top was centred on a circle bottom. This layer also contained triangular tips aligned with the top layer, but 500 nm smaller on every side (to create an overhang). The bottom layer contact pads were also 500 nm smaller on every side.

This configuration is displayed in figure 7.10. The patterned HMS area was designed as 100 × 100 μm^2 so that it could fit within one write-field. This small area meant that the stage could remain stationary between writing the two-layers to negate inaccurate stage movement.

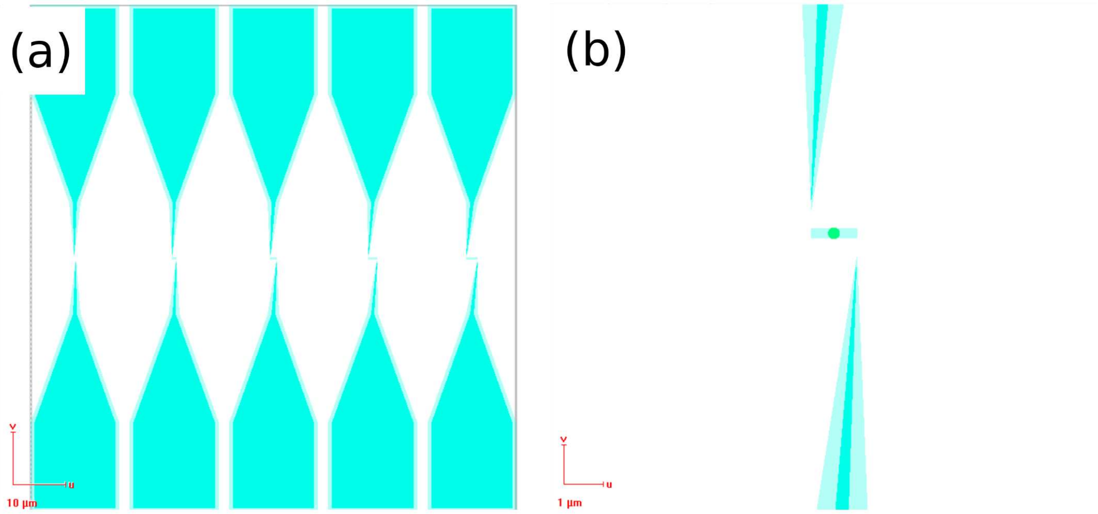

Figure 7.10: Design of the (a) pads and suspended nanorods and (b) close-up view of one of the nanorods suspended on a post.

The rectangles on the top layer were designed as different lengths because the longer rectangles would be easier to turn but would be more likely to droop due to their longer unsupported length. The circles on the bottom layer were designed to have the smallest diameter possible to make rotation easier while providing the strength needed to suspend the rectangle. The triangular tips were designed to increase the electric field strength at the point to maximise the rotation force. The pads were designed to be as large as possible to improve their electrical conductivity and the ease to connect a power supply, while remaining within one write-field. All surfaces were designed

]

overhung to electrically isolate the top and bottom gold layers. SEM images of this HMS are shown in figure 7.11.

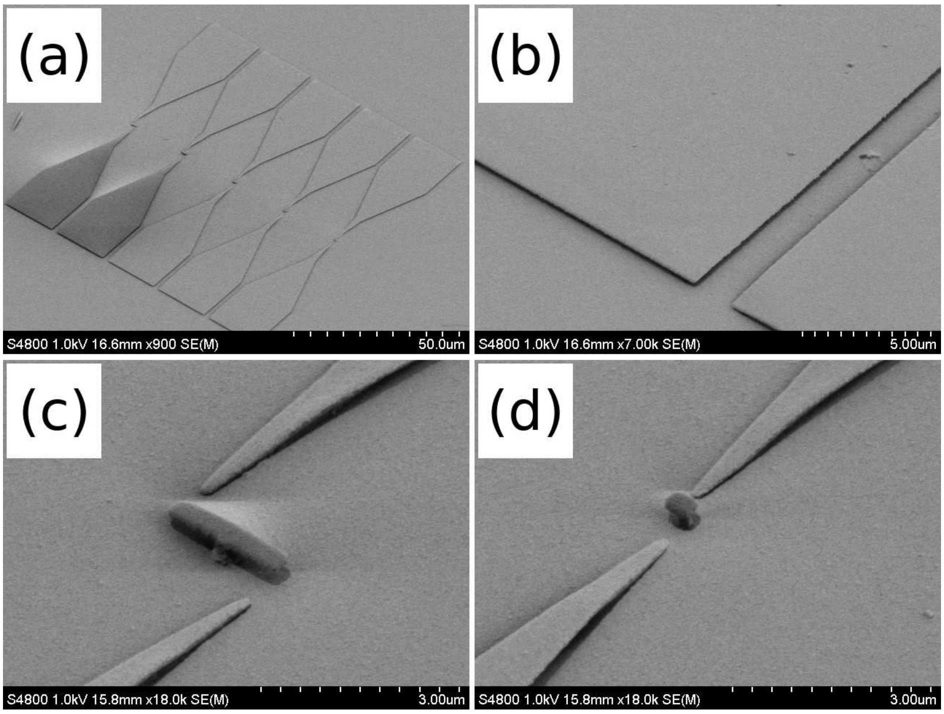

Figure 7.11: SEM images of the fabricated devices where (a) displays the whole write-field (b) is a close-up view of the pads to show an overhang and electrical isolation of the top and bottom layers (c) displays a close-up of the longer rectangle design, and (d) displays a close-up of the shorter rectangle design. The bright white lines are the result of SEM charging and are not physically present on the sample.

7.3.4 Further research direction

The status of this project is that although the fabrication platform has been created and the holograms designed, time, and stability problems with our EBL equipment have halted the progress on this topic. Below are detailed two future applications for this project.

Refractive index sensing

This work has demonstrated that adding a high refractive index oil to the HMS changes the intensity of the holographic image, however, the effect is small. Future work could focus on simulating the meta-atoms with and without the oil, e.g. in COMSOL, to design the plasmonic resonances so that the effect on the holographic image can be increased. Ideally, this could be tailored so that the holographic image is only revealed with the addition of the oil. Such a device could operate as a reusable wetness/refractive index sensor.

Tunable Pancharatnam Berry phase using DC voltage

This work has demonstrated the fabrication of these structures and so the next step is testing if individual nanorods can be reoriented in an experiment. This experiment would involve using the nanomanipulator mode of our RAITH eLine Plus EBL system to contact opposite sets of pads with the nanomanipulator needles. A power supply would then be used to pass a voltage through the needles, which would generate a strong electric field between the triangular tips and the nanorod. The voltage would be increased until the nanorods start to reorient, which we hope could be observed directly using the SEM capabilities of the RAITH eLine Plus system. Alternatively, an ammeter could be used to measure the decrease in the resistance that should happen as the nanorod reorients and charges flow more easily across the HMS.

7.4 Contribution

I designed the holograms, ran the simulations, fabricated all of the samples, and performed all of the experiments.

CHAPTER 8

Conclusion

8.1 Thesis Summary

This thesis has presented a tool to create holograms with total control over the relevant parameters (e.g. the surface topography of the hologram, wavelength, and distance between the hologram and holographic image). This tool uses the GSA to recover the hologram and the RS equation to propagate light between the hologram and the holographic planes using a numerical integral, which is fully described in chapters 1 and 2.

Chapter 3 details the fabrication of the HMSs used in this thesis, in particular, two implementations, one for the visible and another for the millimetre wavelength range.

Some of these fabrication techniques are used in chapter 4 to create FHMSs, before characterising them in an experiment. The latter part of chapter 4 details the use of a hologram recovery algorithm for non-flat holography. Furthermore, chapter 4 explores the unique phenomena resulting from non-flat holograms, e.g. a symmetry property relating the helicity of the incident polarisation with the surface topography of the hologram.

Next, chapter 5 explains how a hologram recovery tool and visible light holograms can be used to create light sheets for LSFM. The performance of multiple methods to create these light sheets are evaluated in a simulation and then verified in an experiment.

Chapter 6 describes how our holography platform can also be used in the millimetre wavelength range, the design of the individual meta-atoms, and the characterisation of millimetre wavelength range holograms.

Finally, chapter 7 details the additional work, first to create a platform for holograms that would operate with partially incoherent light. Second, it shows a method to multiplex two different holographic images in the surface topography of the hologram, provided that the holographic images are created in the near-field. Finally, it introduces a multi-layer lithography technique that operates using two EBL passes with different EHT values, and how this could be used to create tunable HMSs. In particular, these tunable HMSs could be used for refractive index sensing or as a SLM.

8.2 Outlook

The primary goal of this thesis, to create FHMSs, has been achieved and introduces novel phenomena and applications. The following sections, describe the most promising avenues for future work based on this thesis.

8.2.1 Flexible visible wavelength holographic metasurfaces

The ability to conform FHMSs to a non-flat surface topography has immediate utility for anti-counterfeiting and sensing purposes. To this end, we have filed a patent on this technology and are looking for companies to license our idea to while we build up the capabilities to manufacture these devices in-house.

8.2.2 Flexible millimetre wavelength holographic metasurfaces

The underlying concept has been verified, and so we are now exploring applications in EM shielding and antennas. In particular, we are improving our large-scale fabrication abilities so that we can manufacture large-area roll-to-roll FHMSs in the future. This work will likely be the subject of multiple future projects, with the intention being to partner with industry and commercialise the technology. The most promising applications are to retrofit vehicles to alter their radar response, and for antennas which could be unfurled, e.g. to allow larger antennas for CubeSats.

8.2.3 Holograms for light sheet fluorescent microscopy

The holographic platform and the fabrication tools for LSFM are in place. As such, work is needed to verify the principle of this technology in an experiment. Once completed, this holographic platform will likely be explored in a larger project and a patent filed on the operating principle. The HMSs are relatively simple to fabricate, and thus could be commercialised by selling them pre-embedded in microfluidic cells.

APPENDIX A

Simple Gerchberg-Saxton implementation in Python

```
import numpy as np



# Gerchberg-Saxton algorithm using numpy fft
def gsa_npfft(source, target, it_no):
    # (source image, target image,
    # iteration number)

    # fftshift important to compensate for fft and ifft
    target = np.fft.fftshift(target)

    # random initial phase for the far field
    ff = np.random.random(target.shape)
    f_to_n = np.zeros(target.shape)
    nf = np.zeros(target.shape)
```

```
n_to_f = np.zeros(target.shape)


for counter in range(0, it_no):
    n_to_f = np.fft.ifft2(ff)
    nf = source * np.exp(1j * np.angle(n_to_f))
    f_to_n = np.fft.fft2(nf)
    ff = target * np.exp(1j * np.angle(f_to_n))


return ff, f_to_n, nf, n_to_f  # (far field with target intensity,
# far field with approximate target intensity,
# near field with source intensity,
# near field with approximate source intensity)
```

Appendix B

Additional fabrication details

B.1 Fabrication environment

All the fabrication was carried out in one of two class 10,000 cleanrooms, which refers to the number of particles with a diameter greater than 0.5 μm per foot^3. Highly sensitive processes, e.g. spin-coating, were carried out in a class 1000 wet-deck. As a reference, a standard room contains tens of millions of particles with a diameter greater than 0.5 μm in the same volume. Furthermore, the temperature and humidity in the cleanrooms were tightly controlled to provide greater consistency in fabrication processes such as spin-coating.

B.2 Materials

A variety of materials to create HMS devices were used. The most limiting variable is the chemical stability of the materials, which means that the materials used should be resistant to all subsequent steps in the fabrication process. An example of a material exhibiting poor chemical stability would be if subsequent developing or baking steps degraded the material or removed it entirely. As such, materials have to be chosen carefully depending on the structures to be fabricated. The materials used in this thesis can be separated into categories which are detailed below.

B.2.1 Carriers

The first carrier that used was silicon, which exhibits several excellent properties for fabrication. First, it is essentially planar with few defects. Subsequent materials layered onto the carrier are affected by any defects that the initial carrier possesses, and so this flatness is essential. Second, silicon is relatively inert and thus compatible with a wide range of the subsequent chemical processes. Third, silicon has a crystalline structure which promotes easy cleaving, which is an essential step for membrane release. Finally, the silicon that used had a sufficient electrical conductivity to nullify charging effects under EBL processes, and in the SEM. This allowed for EBL processes without needing an additional conductive layer.

The second carrier that used was glass slides. Glass slides are inexpensive and so larger areas can be used compared to silicon. Second, they are optically transparent which allows for transmissive devices, although this avenue was not explored. Third, they are chemically inert, and thus compatible with the rest of the fabrication processes. Glass, however, does not dissipate charge well during EBL or SEM and so often requires an additional conductive layer.

The third carrier that used was a PMMA. Like glass, PMMA is inexpensive and transparent. PMMA is less chemically inert, however, and dissolves in common solvents including acetone and MF-319. Because PMMA was used as a carrier in this thesis, it is not included it in the polymer resist section.

B.2.2 Polymer resists

The polymers used throughout this thesis are detailed in this section, and the typical spinning parameters are shown in table B.1

Table B.1: **Typical resist spinning parameters**

Material	Spin speed (rpm)	Thickness (nm)
Omnicoat	1000	23
SU-8 2000.5	3000	500
SU-8 2000.5 : Cyclopentanone 1:3	6000	90
SU-8 2000.5 : Cyclopentanone 1:2	5000	100
SU-8 2050 : SU-8 2000.5 1:1	5000	2600
SU-8 2050 : SU-8 2000.5 1:1	1000	6700

Omnicoat

Omnicoat is a polymer available from Microchem. Although it was initially designed as an adhesion promotion layer for SU-8, to improve the quality of spinning SU-8, in this thesis it was used as a sacrificial layer.

The point of this sacrificial layer is to allow us to remove SU-8 membranes from a rigid carrier at the end of a fabrication process. Omnicoat is chemically stable to the developer for SU-8 and all of the baking, exposure, and developing steps. Omnicoat is, however, dissolved in MF319 and 1165, which are two chemical solvents also available from Microchem. This step allows the Omnicoat to be removed.

SU-8

SU-8 is a polymer resist available from Microchem in a variety of molecular weights. The name SU-8 originates from the epoxy groups present on the SU-8 monomers. When exposed to UV radiation, or an electron beam (EB), these epoxy groups polymerise into a highly stable compound with excellent chemical stability. SU-8 is a negative-type photo and EB resist, which means that exposed areas remain after development. This is in contrast to a positive type resist, where the exposed areas are washed away after development. It is essential that SU-8 is chemically stable after exposure, as it allows for stable polymer layers that cannot be accidentally removed.

For this thesis, two different types of SU-8 resist with different molecular weights and viscosities, SU-8 2050 and SU-8 2000.5 were used. The viscosity of the resist controls, amongst other things, the thickness of resist layers once spun with a spin coater. The viscosity of these resists was further tailored by mixing different ratios of 2050 and 2000.5 with the solvent Cyclopentanone. Adding more Cyclopentanone would allow for a thinner layer when using the same spin speed, whereas adding more 2050 would increase this thickness. The typical spinning parameters are shown in table B.1

B.2.3 Metals

For the meta-atoms, gold was used throughout most of this thesis because it supports high-efficiency plasmonic resonances across most of the visible range, and is compatible with all of the fabrication processes. In particular, gold has suitable adhesion to SU-8 films and does not melt or dissolve during the baking or development processes. Gold adhesion can be promoted by using a 2 nm layer of titanium, but this was deemed unnecessary for most of my fabrication procedures. Finally, gold is physically soft and inert which makes it ideally suited to RIE.

B.3 Metal evaporation

The evaporations detailed in this thesis were executed using an Edwards AUTO 306 Electron Beam evaporator. This evaporator uses an electron gun, with the beam incident on the underside of a tungsten crucible. A simple diagram of this instrument can be seen in figure B.1.

The energy from these electrons is transferred to the crucible which heats the metal inside it. With a high enough beam intensity, the metal is evaporated towards the sample at the top of the chamber in a highly directional fashion. To get the total thickness deposited, a quartz crystal monitor was used. When the material is deposited on the crystal, the electrical resonance is altered which, combined with the density of the material, can be used to accurately find the thickness of an evaporated layer. All evaporations were performed in a high vacuum environment ($\approx 10^{-5}$ Pa) to reduce collisions between metal molecules and air molecules. Evaporations were carried out using sweeping of the EB, which ensures that the EB heats the crucible evenly (as opposed to in one location) leading to better evaporations of some materials. In addition, the evaporator rotates the sample around the centre to improve the evaporation uniformity by removing angular dependence as a factor. Finally,

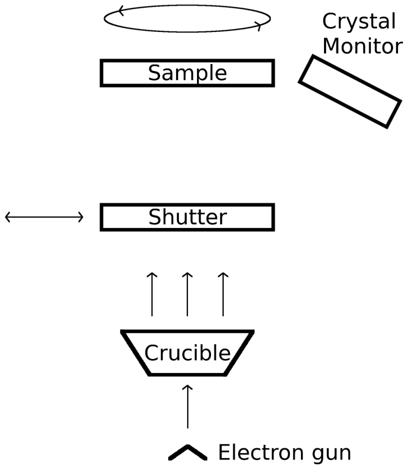

Figure B.1: A basic diagram of the Edwards AUTO 306 Electron Beam evaporator system used throughout this thesis. Electrons are accelerated from the electron gun to heat the crucible. The evaporated material moves towards the sample where it can be blocked by the shutter if required. The stage is rotated to improve the uniformity of evaporation. A crystal monitor measures the evaporated thickness.

the evaporator employs a shutter, which can be used to block the evaporated material from adhering to the sample. The evaporation rate of the initial material from the crucible can be too high, which could impart too much heat into the sample and damage it. Alternatively, it could be too low, which could impair the forming of high-quality films. As such, the shutter allows us only to evaporate material onto the sample once the rate is within the correct range.

B.4 Electron beam lithography

To pattern most of the samples in this thesis EBL was used. This process uses a tightly focused beam of electrons to define patterns in the resist. As stated above, the bond structure inside the resist is altered on the incidence of electrons or UV radiation. The weakly bonded areas can then be removed with a developing step after electron exposure. In general, a negative-type resist should be used when the area of the pattern is much smaller than the writing area. A positive resist should be used when the opposite is true to reduce the exposure time.

The EBL system used was a RAITH eLine Plus. A schematic of this device is shown in figure B.2.

These electrons are accelerated from the tip at variable electron energies, up to 30keV. An EM

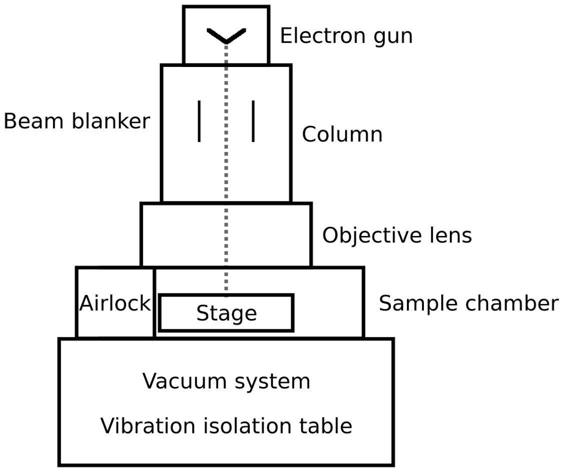

Figure B.2: A basic diagram of the Raith eLine Plus EBL system used throughout this thesis. The EB originates at the tip and is accelerated through the column past a collection of lenses, a blanker, and an aperture. This beam then exits through an EM objective lens to focus a spot onto the sample, which is placed on the top surface of the mobile stage. The system sits on a bed which reduces vibrations and creates the high vacuum needed.

beam blanker is present for fast switching of the beam for higher quality writing. A multitude of lenses is used to collimate the beam and adjust the spot position, focal distance, aperture alignment, and stigmation. Different apertures are also present to control the current, spot size, and to further collimate the beam. In addition to the EM lenses, the position of the spot on the sample can be changed in three dimensions by adjusting the position of the stage.

The beam spot can only be deflected within a specific range while maintaining its circular shape. This range is set by the write-field and depends on the working distance from the column to the sample. In this thesis, the write-field size was set at 100 μm. To expose an area larger than 100 μm $\times$ 100 μm, the stage is moved. Deflecting the beam spot with the EM lenses is extremely accurate and repeatable. Stage movements, however, are less accurate and repeatable. Therefore, without careful write-field alignment, individual write-fields can be written on top of each other or separated by gaps. Write-field alignment is the procedure of calibrating the real world XYZ coordinates with the sample UVW coordinates used in the eLine. When performed correctly, stage movements are accurate within a few nm. Using a smaller write-field means that the beam deflection is smaller and so the beam spot more circular and uniform. It does, however, mean that the stage has to be moved more frequently which is less accurate and repeatable than beam deflection. Fortunately, most of the patterns written during this thesis were reasonably resistant to write-field alignment errors.

The write-field alignment procedure was conducted before every sample exposure. For longer writes, or when additional stage accuracy is needed, multiple alignments were made throughout the exposure. The beam spot was optimised each time before writing. Before loading a sample, a scalpel blade was used to make a shallow scratch in an unused area of the sample. The scratch, and the resulting dust in the surrounding area, could then be used to make rough focus, aperture alignment, and stigmation adjustments. The focus was adjusted to give the sharpest SEM image. For aperture alignment, the focus was wobbled by changing the working distance up and down. When the aperture alignment is proper, the SEM image is relatively stationary during focus wobbling. For stigmation adjustment, a circular object is found on the sample, and the stigmation is changed until the sharpest SEM image is seen. Once this initial beam optimisation has been made, a contamination spot can be burned into the resist, ideally near the exposure area to be representative. The contamination spot is formed from small amounts of impurities which attach themselves to the charged surface formed by the beam. SEM images of representative contamination spots are shown in figure B.3. This method provides a direct way to observe the quality and shape of the beam, and successive spots can be burned to optimise the beam further.

Were a sample to charge, making it difficult to see improvements in the SEM image when varying the beam parameters, a different beam optimisation technique was used. The probe-current reader gives a value for the current read by the stage. By watching this, while changing the working distance of the system, the working distance which gave the most substantial absolute current could be found. At this working distance, the system is in approximate focus. If the charging is relatively minor, then the conventional focusing procedure can be followed once this approximate focus is reached. It should be noted, however, that charging does fundamentally limit the size and quality of features that can be written. Consequently, whenever possible a conductive layer was used to limit

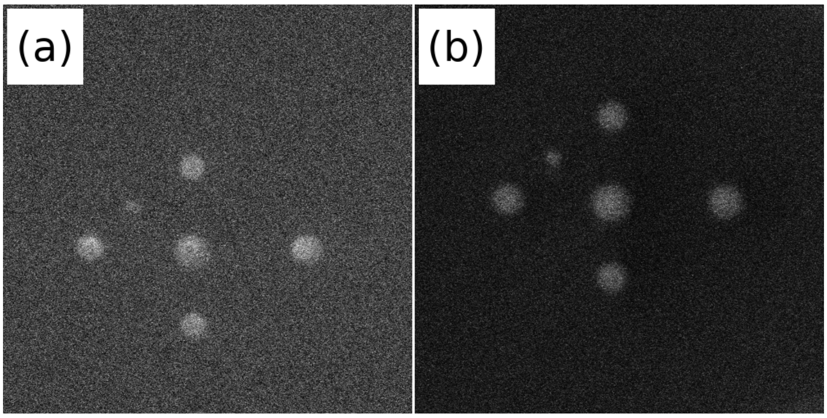

Figure B.3: The same contamination spot arrays viewed at an EHT of (a) 30 keV and (b) 2 keV. An array of spots is used because a single spot could be more easily mistaken for a small spot of dust on the sample. In addition, having an array of spots improves automatic write-field alignment procedures if needed. During the write-field alignment procedure, the stage is moved and the amount of movement and exact position is calibrated from SEM images. The exact position of two different EHT images can be aligned by performing this procedure calibrating to the same point for both EHTs. The spots can appear somewhat different at different EHTs as the imaging properties of the system change, hence, the brightness, contrast, and detail differences between (a) and (b).

the charging.

The final resolution of an EBL system is always poorer than the diffractive properties of the system. Limits on the resolution can originate in the resist, where forwards and backwards scattering leads to an enlarged exposed area. This effect is shown in figure B.4(a-b) where it can be seen that thinning the resist layer would result in a smaller lateral exposure.

In addition, the effect of the EHT is shown by comparing B.4(a) and B.4(b), where higher EHT values penetrate deeper into the resist.

To reduce the effect of forward scattering the resist can be thinned, which means that although the electrons are still forward scattered they have a more limited propagation distance and so their lateral propagation is also limited. However, thinning the resist means that the resultant protective lithographic mask is less substantial, limiting the thickness of the patterned layer through either etch-back or lift-off. To reduce the effect of backward scattering carriers, the resist needs to be chosen carefully. An additional limit on the final resolution can originate from charging in the resist. If enough electrons are incident in one area it becomes negatively charged. Electrons that are then

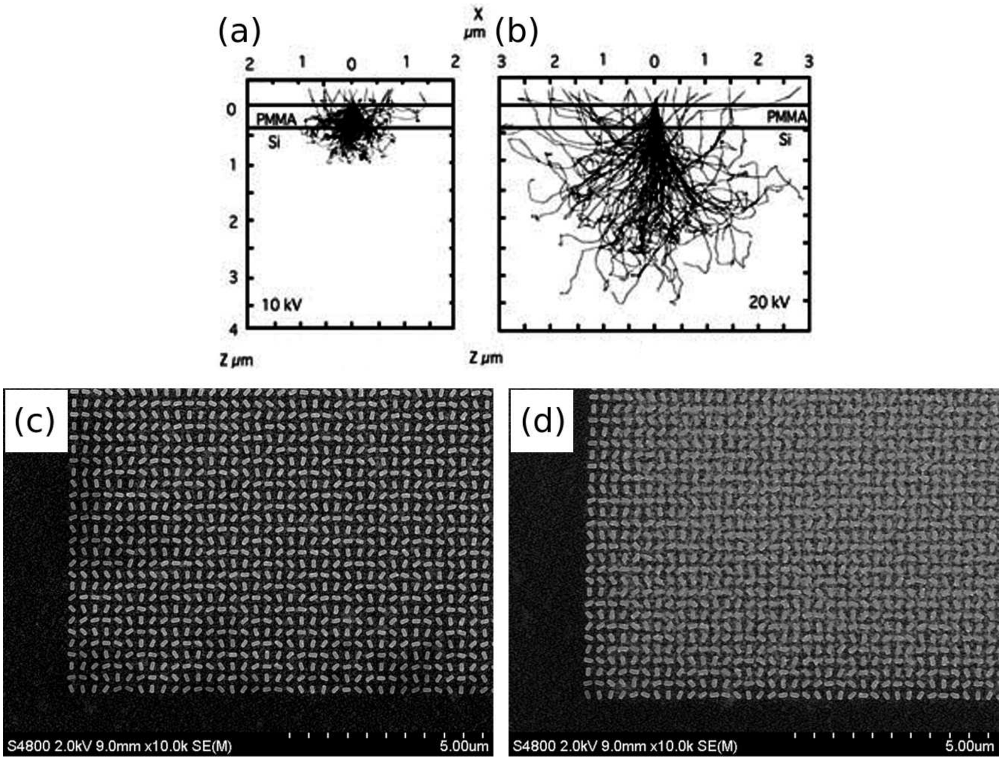

Figure B.4: The scattering properties of electrons in a PMMA resist at (a) 10 keV and (b) 20 keV [138]. Here, it is shown that the deeper within the resist, the more significant the lateral spread of electrons and thus, the larger the size of the exposed structures. In addition, the higher the EHT, the deeper the electrons penetrate into the resist. Nanorod structures defined in SU-8 resist at (c) approximately the correct dose (d) a dose that was too high. Here, it can be seen that increasing the dose fills in the gaps between the nanorods.

accelerated towards the sample are repelled from these areas, which limits the resolution. Some resists exhibit better-charging properties than others; however, the main improvement can be made by depositing a conductive layer underneath the resist. In the case of this thesis, gold was used as the conductive layer, but other materials such as aluminium, silver, or indium tin oxide (ITO) could also be used.

The number of electrons incident on a given area of resist, called the dose, is a key parameter in EBL and is defined as

$$D = \frac{IT}{A}, \tag{B.1}$$

where I, t, and A are the beam current, time exposed, and area exposed respectively. A particular dose effect occurs when adjacent areas are written, as stray electrons can expose resist in the adjacent area. The solution for this is a proximity correction, which modulates the dose across the patterned area.

If the dose is too low, then the resist is insufficiently exposed and the pattern is unwritten. If the dose is too high, then small areas of the pattern can link together into a continuous area. Furthermore, higher doses take longer to write and EBL time is valuable. The dose also controls, to an extent, the size of the final features, where a higher dose leads to more extensive features. This effect is shown through experimental SEM images in figure B.4(c-d). Here, B.4(c) is exposed correctly, whereas B.4(d) is overexposed leading to the gaps between the nanorods being absent.

The final beam parameter of note was the beam writing speed. This is the time taken for the beam to sweep across a given length or area. For the work in this thesis, the beam speed was kept in the 10-13 mm s^{-1} range. The beam speed is a major bottleneck of the EBL writing process, so, using a higher value speeds up the writing. A higher beam speed does, however, also reduce the accuracy of the beam movements and can lead to poor-quality writing.

B.5 Reactive ion etching

To create patterns in gold, a custom-built RIE machine was used. During operation, heavy argon ions are accelerated by a DC bias into the sample at high speeds. This physically, and uniformly mills the sample. By masking particular areas using a EBL procedure, arbitrary patterns can be transferred into the gold. The critical parameter in the RIE procedure is the DC bias as this dictates the kinetic energy imparted by the argon-sample collisions. A basic diagram of the RIE can be seen in figure B.5.

Argon was chosen for the RIE steps because its high mass allows it to mill the gold effectively. Furthermore, argon etching is a simple physical process, and etchant gasses with a chemical component are not required for such thin gold layers. Other materials at different thickness could require a more complex etching procedure to ensure parallel side walls of the etched material.

To perform a RIE procedure, the sample was first loaded into a high vacuum chamber and the chamber was pumped down to ≈10^{-5} Pa. The high vacuum removes impurities which could alter the properties of the etching. An O_2 etching can be conducted to further clean the chamber; however, this is less critical for the physical etching used in this thesis. Argon is then deposited into the chamber at a controlled rate using a mass flow controller to achieve a set pressure. A radio frequency (RF) signal is then used to ionise the gas at 13.56 MHz. Upon excitation by this signal, the heavy ions remain relatively stationary while the electrons are accelerated into the top plate and walls where they are conducted to the ground. This sets up a static DC field within the chamber and creates a plasma. The pressure of this plasma must be kept within limits for it to be sustained.

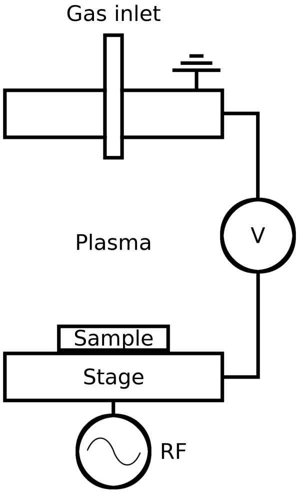

Figure B.5: A basic diagram of the RIE system used throughout this thesis. The gas is injected into a low-pressure chamber. A RF is then used to accelerate Argon ions into the sample to mill it.

The typical RIE parameters are displayed in table B.2

Table B.2: **Typical RIE parameters**

Parameter	Value
Base Pressure	1e-5 mPa
Etching Pressure	5e-2 mPa
Argon flow rate	500 sccm
RF Power	19 W
DC Bias	-330 V

The etching time was altered depending on the thickness of the Gold layer to be milled and on the exact value of the etching pressure. For 40 nm of gold, the typical etching time was for 9 minutes and for 200 nm of gold the typical etching time was 45 minutes. Accordingly, the etching rate was approximately 4.4 nm minute^{-1}. In general, the side of too little etching time was erred on as the etching can always be continued after an examination of the sample under the optical microscope or a SEM. The mask is also removed by the physical etching process, which for SU-8 2000.5:Cyclopentanone 1:2 was at a rate of $\approx$10 nm minute^{-1}. There would often be a thin layer of residual SU-8 left after the etch. However, this layer was not found to affect the properties of the written structures. For SU-8, there is no remover for the mask but with other resists, e.g. ZEP or PMMA, the residual resist can be removed at the end of the fabrication process.

B.6 Membrane release and manipulation

The fabrication procedure for the FHMSs required creating a transferable nanopatterned membrane and then manipulating it from the initial onto the final carrier. To release flexible membranes from the initial rigid silicon carrier, the following procedure was used. First, all edges of the sample were cleaved to allow the lift-off solvent to dissolve all parts of the sacrificial layer. To perform the cleave, a custom-built cleaving system consisting of two mobile platforms and a blade is used. The blade imparted a defect into the regular crystal structure of the silicon. By carefully imparting a force on the silicon with the defect above an edge, this crack was propagated along a crystal direction in the silicon.

MF-319 solvent was used at room temperature in a glass Petri dish for approximately 2 hours to fully dissolve the Omnicoat sacrificial layer to leave a free-floating membrane. Tweezers were then used to extract the membrane from the MF-319 into DI water. The membrane is hydrophobic and so can curl up into a cylinder. When this occurred, tweezers were used in conjunction with dropping DI water droplets onto the membrane to gently unfurl it. Once the membrane was unfurled, the surface tension of the DI kept it taut.

To mount the flexible membrane onto the new carrier, one of two approaches are used. The first approach was to apply a droplet of DI water onto the new carrier. Tweezers were then used to pick the membrane up by one corner and gently pull it across the DI water droplet until it lay conformed to the new carrier in the desired position.

The second approach involved submerging the new carrier underneath the membrane in the DI water. The DI water was then carefully removed using a pipette to apply the membrane to the new carrier.

In both of the above methods, if there was too much DI water, a cleanroom wipe was used to absorb the excess. Additionally, to precisely position the membrane, it was pulled taut across the object using tweezers.

Also, a nitrogen gun was often used to flatten the FHMS onto the new carrier. To do this, nitrogen was gently blown in one direction starting from one side, typically in a corner, and worked across to the opposite side. This procedure reduced the unwanted folding of the FHMSs.

Bibliography

[1] J. Brooker, “The polytechnic ghost: Pepper’s ghost, metempsychosis and the magic lantern at the royal polytechnic institution,” *Early Popular Visual Culture*, vol. 5, no. 2, pp. 189–206, 2007.

[2] T. B. Greenslade Jr, “Pepper’s ghost,” *The Physics Teacher*, vol. 49, no. 6, pp. 338–339, 2011.

[3] R. Collier, *Optical holography*. Elsevier, 2013.

[4] J. Goodman, *Introduction to Fourier optics*. McGraw-hill, 2008.

[5] G. Saxby, *Practical holography*. CRC Press, 2003.

[6] U. Schnars, C. Falldorf, J. Watson, and W. Jüptner, “Digital holography,” in *Digital Holography and Wavefront Sensing*, pp. 39–68, Springer, 2015.

[7] W. Jueptner and U. Schnars, *Digital Holography: Digital Hologram Recording, Numerical Reconstruction, and Related Techniques*. Springer, 2005.

[8] W. T. Chen, A. Y. Zhu, V. Sanjeev, M. Khorasaninejad, Z. Shi, E. Lee, and F. Capasso, “A broadband achromatic metalens for focusing and imaging in the visible,” *Nature nanotechnology*, vol. 13, no. 3, p. 220, 2018.

[9] J. Cheng, S. Jafar-Zanjani, and H. Mosallaei, “All-dielectric ultrathin conformal metasurfaces: lensing and cloaking applications at 532 nm wavelength,” *Scientific Reports*, vol. 6, p. 38440, 2016.

[10] L. Huang, X. Chen, H. Mühlenbernd, H. Zhang, S. Chen, B. Bai, Q. Tan, G. Jin, K.-W. Cheah, C.-W. Qiu, J. Li, T. Zentgraf, and S. Zhang, “Three-dimensional optical holography using a plasmonic metasurface,” *Nature Communications*, vol. 4, p. 2808, 2013.

[11] D. Wen, F. Yue, G. Li, G. Zheng, K. Chan, S. Chen, M. Chen, K. F. Li, P. W. H. Wong, K. W. Cheah, E. Y. B. Pun, S. Zhang, and X. Chen, “Helicity multiplexed broadband metasurface holograms,” *Nature Communications*, vol. 6, p. 8241, 2015.

[12] T. Nobukawa and T. Nomura, “Multilayer recording holographic data storage using a varifocal lens generated with a kinoform,” *Optics Letters*, vol. 40, no. 23, pp. 5419–5422, 2015.

[13] K.-i. Shimada, T. Ide, T. Shimano, K. Anderson, and K. Curtis, “New optical architecture for holographic data storage system compatible with blu-ray disc™ system,” *Optical Engineering*, vol. 53, no. 2, pp. 025102–025102, 2014.

[14] M. Heydt, “Theory of holography,” in *How Do Spores Select Where to Settle?*, pp. 5–11, Springer, 2011.

[15] E. N. Leith and J. Upatnieks, “Reconstructed wavefronts and communication theory,” *JOSA*, vol. 52, no. 10, pp. 1123–1130, 1962.

[16] E. N. Leith and J. Upatnieks, “Wavefront reconstruction with continuous-tone objects,” *JOSA*, vol. 53, no. 12, pp. 1377–1381, 1963.

[17] R. S. Kshetrimayum, “A brief intro to metamaterials,” *IEEE Potentials*, vol. 23, no. 5, pp. 44–46, 2004.

[18] S. Zouhdi, A. Sihvola, and A. P. Vinogradov, *Metamaterials and plasmonics: fundamentals, modelling, applications*. Springer Science & Business Media, 2008.

[19] H.-T. Chen, A. J. Taylor, and N. Yu, “A review of metasurfaces: physics and applications,” *Reports on progress in physics*, vol. 79, no. 7, p. 076401, 2016.

[20] N. Meinzer, W. L. Barnes, and I. R. Hooper, “Plasmonic meta-atoms and metasurfaces,” *Nature Photonics*, vol. 8, no. 12, p. 889, 2014.

[21] S. A. Mousavi, E. Plum, J. Shi, and N. I. Zheludev, “Coherent control of birefringence and optical activity,” *Applied Physics Letters*, vol. 105, no. 1, p. 011906, 2014.

[22] M. M. Masud, B. Ijaz, I. Ullah, and B. Braaten, “A compact dual-band emi metasurface shield with an actively tunable polarized lower band,” *IEEE Transactions on Electromagnetic Compatibility*, vol. 54, no. 5, pp. 1182–1185, 2012.

[23] J. Lee, S. Jung, P.-Y. Chen, F. Lu, F. Demmerle, G. Boehm, M.-C. Amann, A. Alù, and M. A. Belkin, “Ultrafast electrically tunable polaritonic metasurfaces,” *Advanced Optical Materials*, vol. 2, no. 11, pp. 1057–1063, 2014.

[24] Z. Wei, Y. Cao, X. Su, Z. Gong, Y. Long, and H. Li, “Highly efficient beam steering with a transparent metasurface,” *Optics Express*, vol. 21, no. 9, pp. 10739–10745, 2013.

[25] M. Lorente-Crespo and C. Mateo-Segura, “Analysis of 2-d periodic leaky-wave nano-antennas in the nir,” in *Antennas and Propagation Society International Symposium (APSURSI), 2014 IEEE*, pp. 83–84, IEEE, 2014.

[26] J. Shi, X. Fang, E. T. Rogers, E. Plum, K. F. MacDonald, and N. I. Zheludev, “Coherent control of snell’s law at metasurfaces,” *Optics Express*, vol. 22, no. 17, pp. 21051–21060, 2014.

[27] P. Reader-Harris and A. Di Falco, “Nanoplasmonic filters for hollow core photonic crystal fibers,” *ACS Photonics*, vol. 1, no. 10, pp. 985–989, 2014.

[28] P. Reader-Harris, A. Ricciardi, T. Krauss, and A. Di Falco, “Optical guided mode resonance filter on a flexible substrate,” *Optics Express*, vol. 21, no. 1, pp. 1002–1007, 2013.

[29] A. Di Falco, M. Ploschner, and T. Krauss, "Flexible metamaterials at visible wavelengths," *New Journal of Physics*, vol. 12, no. 11, p. 113006, 2010.

[30] S. Yang, P. Liu, M. Yang, Q. Wang, J. Song, and L. Dong, "From flexible and stretchable meta-atom to metamaterial: A wearable microwave meta-skin with tunable frequency selective and cloaking effects," *Scientific Reports*, vol. 6, p. 21921, 2016.

[31] S. Walia, C. Shah, P. Gutruf, H. Nili, D. R. Chowdhury, W. Withayachumnankul, M. Bhaskaran, and S. Sriram, "Flexible metasurfaces and metamaterials: A review of materials and fabrication processes at micro-and nano-scales," *Applied Physics Reviews*, vol. 2, no. 1, p. 011303, 2015.

[32] A. Di Falco, Y. Zhao, and A. Alú, "Optical metasurfaces with robust angular response on flexible substrates," *Applied Physics Letters*, vol. 99, no. 16, p. 163110, 2011.

[33] G. Zheng, H. Mühlenbernd, M. Kenney, G. Li, T. Zentgraf, and S. Zhang, "Metasurface holograms reaching 80% efficiency," *Nature Nanotechnology*, vol. 10, no. 4, pp. 308–312, 2015.

[34] A. Arbabi, Y. Horie, A. Ball, M. Bagheri, and A. Faraon, "Subwavelength-thick lenses with high numerical apertures and large efficiency based on high-contrast transmitarrays," *Nature Communications*, vol. 6, p. 7069, 2015.

[35] A. Arbabi, Y. Horie, M. Bagheri, and A. Faraon, "Dielectric metasurfaces for complete control of phase and polarization with subwavelength spatial resolution and high transmission," *Nature Nanotechnology*, vol. 10, no. 11, pp. 937–943, 2015.

[36] L. Wang, S. Kruk, H. Tang, T. Li, I. Kravchenko, D. N. Neshev, and Y. S. Kivshar, "Grayscale transparent metasurface holograms," *Optica*, vol. 3, no. 12, pp. 1504–1505, 2016.

[37] N. Yu and F. Capasso, "Flat optics with designer metasurfaces," *Nature Materials*, vol. 13, no. 2, pp. 139–150, 2014.

[38] H.-C. Liu, B. Yang, Q. Guo, J. Shi, C. Guan, G. Zheng, H. Mühlenbernd, G. Li, T. Zentgraf, and S. Zhang, “Single-pixel computational ghost imaging with helicity-dependent metasurface hologram,” *Science Advances*, vol. 3, no. 9, p. e1701477, 2017.

[39] Y. Montelongo, J. Tenorio-Pearl, W. Milne, and T. Wilkinson, “Polarization switchable diffraction based on subwavelength plasmonic nanoantennas,” *Nano Letters*, vol. 14, no. 1, pp. 294–298, 2013.

[40] W. Ye, F. Zeuner, X. Li, B. Reineke, S. He, C.-W. Qiu, J. Liu, Y. Wang, S. Zhang, and T. Zentgraf, “Spin and wavelength multiplexed nonlinear metasurface holography,” *Nature Communications*, vol. 7, p. 11930, 2016.

[41] M. Khorasaninejad, A. Ambrosio, P. Kanhaiya, and F. Capasso, “Broadband and chiral binary dielectric meta-holograms,” *Science Advances*, vol. 2, no. 5, p. e1501258, 2016.

[42] Y. Montelongo, J. O. Tenorio-Pearl, C. Williams, S. Zhang, W. I. Milne, and T. D. Wilkinson, “Plasmonic nanoparticle scattering for color holograms,” *Proceedings of the National Academy of Sciences*, vol. 111, no. 35, pp. 12679–12683, 2014.

[43] X. Li, L. Chen, Y. Li, X. Zhang, M. Pu, Z. Zhao, X. Ma, Y. Wang, M. Hong, and X. Luo, “Multicolor 3d meta-holography by broadband plasmonic modulation,” *Science Advances*, vol. 2, no. 11, p. e1601102, 2016.

[44] S. M. Kamali, E. Arbabi, A. Arbabi, Y. Horie, M. Faraji-Dana, and A. Faraon, “Angle-multiplexed metasurfaces: encoding independent wavefronts in a single metasurface under different illumination angles,” *Phys Rev X*, vol. 7, p. 041056, 2017.

[45] L. Huang, H. Mühlenbernd, X. Li, X. Song, B. Bai, Y. Wang, and T. Zentgraf, “Broadband hybrid holographic multiplexing with geometric metasurfaces,” *Advanced Materials*, vol. 27, no. 41, pp. 6444–6449, 2015.

[46] S. M. Kamali, A. Arbabi, E. Arbabi, Y. Horie, and A. Faraon, "Decoupling optical function and geometrical form using conformal flexible dielectric metasurfaces," *Nature communications*, vol. 7, p. 11618, 2016.

[47] S. Schwaiger, A. Rottler, and S. Mendach, "Rolled-up metamaterials," *Advances in OptoElectronics*, vol. 2012, 2012.

[48] N. Kooy, K. Mohamed, L. T. Pin, and O. S. Guan, "A review of roll-to-roll nanoimprint lithography," *Nanoscale research letters*, vol. 9, no. 1, p. 320, 2014.

[49] H.-S. Ee and R. Agarwal, "Tunable metasurface and flat optical zoom lens on a stretchable substrate," *Nano Letters*, vol. 16, no. 4, pp. 2818–2823, 2016.

[50] S. C. Malek, H.-S. Ee, and R. Agarwal, "Strain multiplexed metasurface holograms on a stretchable substrate," *Nano Letters*, vol. 17, p. 3641–3645, 2017.

[51] B. B. Baker and E. T. Copson, *The mathematical theory of Huygens' principle*, vol. 329. American Mathematical Soc., 2003.

[52] T. Niemi, P. Alitalo, A. O. Karilainen, and S. A. Tetryakov, "Electrically small huygens source antenna for linear polarization," *IET Microwaves, Antennas & Propagation*, vol. 6, no. 7, pp. 735–739, 2012.

[53] D. A. B. Miller, "Huygens's wave propagation principle corrected," *Opt. Lett.*, vol. 16, pp. 1370–1372, Sep 1991.

[54] U. Schnars and W. Jueptner, *Hologram Recording, Numerical Reconstruction, and Related Techniques*. Springer, Berlin, 2005.

[55] T. Latychevskaia, J.-N. Longchamp, and H.-W. Fink, "When holography meets coherent diffraction imaging," *Optics express*, vol. 20, no. 27, pp. 28871–28892, 2012.

[56] S. A. Maier, *Plasmonics: fundamentals and applications*. Springer Science & Business Media, 2007.

[57] P. Genevet, F. Capasso, F. Aieta, M. Khorasaninejad, and R. Devlin, “Recent advances in planar optics: from plasmonic to dielectric metasurfaces,” *Optica*, vol. 4, no. 1, pp. 139–152, 2017.

[58] J. Zheng, C. Zhou, M. Yu, and J. Liu, “Different sized luminescent gold nanoparticles,” *Nanoscale*, vol. 4, no. 14, pp. 4073–4083, 2012.

[59] A. Kristensen, J. K. Yang, S. I. Bozhevolnyi, S. Link, P. Nordlander, N. J. Halas, and N. A. Mortensen, “Plasmonic colour generation,” *Nature Reviews Materials*, vol. 2, no. 1, p. 16088, 2017.

[60] Y.-K. R. Wu, A. E. Hollowell, C. Zhang, and L. J. Guo, “Angle-insensitive structural colours based on metallic nanocavities and coloured pixels beyond the diffraction limit,” *Scientific reports*, vol. 3, p. 1194, 2013.

[61] P. L. Stiles, J. A. Dieringer, N. C. Shah, and R. P. Van Duyne, “Surface-enhanced raman spectroscopy,” *Annu. Rev. Anal. Chem.*, vol. 1, pp. 601–626, 2008.

[62] S. Nie and S. R. Emory, “Probing single molecules and single nanoparticles by surface-enhanced raman scattering,” *science*, vol. 275, no. 5303, pp. 1102–1106, 1997.

[63] B. Mueller, N. Rubin, R. Devlin, B. Groever, and F. Capasso, “Metasurface polarization optics: Independent phase control of arbitrary orthogonal states of polarization,” *Physical Review Letters*, vol. 118, no. 11, p. 113901, 2017.

[64] M. Khorasaninejad, W. T. Chen, R. C. Devlin, J. Oh, A. Y. Zhu, and F. Capasso, “Metalenses at visible wavelengths: Diffraction-limited focusing and subwavelength resolution imaging,” *Science*, vol. 352, no. 6290, pp. 1190–1194, 2016.

[65] X. Ding, F. Monticone, K. Zhang, L. Zhang, D. Gao, S. N. Burokur, A. de Lustrac, Q. Wu, C.-W. Qiu, and A. Alù, “Ultrathin pancharatnam–berry metasurface with maximal cross-polarization efficiency,” *Advanced Materials*, vol. 27, no. 7, pp. 1195–1200, 2015.

[66] A. Arbabi and A. Faraon, “Fundamental limits of ultrathin metasurfaces,” *Scientific reports*, vol. 7, p. 43722, 2017.

[67] R. C. Devlin, M. Khorasaninejad, W. T. Chen, J. Oh, and F. Capasso, “Broadband high-efficiency dielectric metasurfaces for the visible spectrum,” *Proceedings of the National Academy of Sciences*, vol. 113, no. 38, pp. 10473–10478, 2016.

[68] R. Gerchberg, “A practical algorithm for the determination of phase from image and diffraction plane pictures,” *Optik*, vol. 35, p. 237, 1972.

[69] U. Schnars and W. P. Jüptner, “Digital recording and numerical reconstruction of holograms,” *Measurement science and technology*, vol. 13, no. 9, p. R85, 2002.

[70] R. Di Leonardo, F. Ianni, and G. Ruocco, “Computer generation of optimal holograms for optical trap arrays,” *Optics Express*, vol. 15, no. 4, pp. 1913–1922, 2007.

[71] P. Pozzi, L. Maddalena, N. Ceffa, O. Soloviev, G. Vdovin, E. Carroll, and M. Verhaegen, “Fast calculation of computer generated holograms for 3d photostimulation through compressive-sensing gerchberg–saxton algorithm,” *Methods and Protocols*, vol. 2, no. 1, p. 2, 2019.

[72] J. Burch and A. Di Falco, “Surface topology specific metasurface holograms,” *ACS Photonics*, vol. 5, no. 5, pp. 1762–1766, 2018.

[73] J. A. Veerman, J. J. Rusch, and H. P. Urbach, “Calculation of the rayleigh–sommerfeld diffraction integral by exact integration of the fast oscillating factor,” *JOSA A*, vol. 22, no. 4, pp. 636–646, 2005.

[74] M. Agio and A. Alù, *Optical antennas.* Cambridge University Press, 2013.

[75] A. B. Constantine *et al.*, “Antenna theory: analysis and design,” *Microstrip Antennas, third edition, John wiley & sons*, 2005.

[76] C. Van Loan, *Computational frameworks for the fast Fourier transform*, vol. 10. Siam, 1992.

[77] J. W. Cooley and J. W. Tukey, "An algorithm for the machine calculation of complex fourier series," *Mathematics of computation*, vol. 19, no. 90, pp. 297–301, 1965.

[78] J. Burch, D. Wen, C. Xianzhong, and A. Di Falco, "Conformable holographic metasurfaces," *Scientific Reports*, vol. 7, p. 4520, 2017.

[79] S. C. Chan, M. Mina, S. S. Udpa, L. Udpa, and W. Lord, "Finite element analysis of multilevel acoustic fresnel lenses," *IEEE transactions on ultrasonics, ferroelectrics, and frequency control*, vol. 43, no. 4, pp. 670–677, 1996.

[80] E. Walsby, S. Wang, J. Xu, T. Yuan, R. Blaikie, S. Durbin, X.-C. Zhang, and D. Cumming, "Multilevel silicon diffractive optics for terahertz waves," *Journal of Vacuum Science & Technology B: Microelectronics and Nanometer Structures Processing, Measurement, and Phenomena*, vol. 20, no. 6, pp. 2780–2783, 2002.

[81] M. V. Berry, "The adiabatic phase and pancharatnam's phase for polarized light," *Journal of Modern Optics*, vol. 34, no. 11, pp. 1401–1407, 1987.

[82] Y. Aharonov and D. Bohm, "Significance of electromagnetic potentials in the quantum theory," *Physical Review*, vol. 115, no. 3, p. 485, 1959.

[83] V. V. Tuchin, "Polarized light interaction with tissues," *Journal of Biomedical Optics*, vol. 21, no. 7, pp. 1 – 37 – 37, 2016.

[84] Y.-W. Huang, W. T. Chen, W.-Y. Tsai, P. C. Wu, C.-M. Wang, G. Sun, and D. P. Tsai, "Aluminum plasmonic multicolor meta-hologram," *Nano Letters*, vol. 15, no. 5, pp. 3122–3127, 2015.

[85] S.-Y. Lee, K. Kim, G.-Y. Lee, and B. Lee, "Polarization-multiplexed plasmonic phase generation with distributed nanoslits," *Optics Express*, vol. 23, no. 12, pp. 15598–15607, 2015.

[86] C. Rizza, A. Di Falco, and A. Ciattoni, "Gain assisted nanocomposite multilayers with near zero permittivity modulus at visible frequencies," *Applied Physics Letters*, vol. 99, no. 22, p. 221107, 2011.

[87] E. G. Williams, *Fourier acoustics: sound radiation and nearfield acoustical holography*. Elsevier, 1999.

[88] B. Bernschütz, "A spherical far field hrir/hrtf compilation of the neumann ku 100," in *Proceedings of the 40th Italian (AIA) annual conference on acoustics and the 39th German annual conference on acoustics (DAGA) conference on acoustics*, p. 29, AIA/DAGA, 2013.

[89] R. M. Power and J. Huisken, "A guide to light-sheet fluorescence microscopy for multiscale imaging," *Nature methods*, vol. 14, no. 4, p. 360, 2017.

[90] A.-K. Gustavsson, P. N. Petrov, M. Y. Lee, Y. Shechtman, and W. Moerner, "3d single-molecule super-resolution microscopy with a tilted light sheet," *Nature communications*, vol. 9, no. 1, p. 123, 2018.

[91] E. H. Stelzer, "Light-sheet fluorescence microscopy for quantitative biology," *Nat. Methods*, vol. 12, no. 1, pp. 23–26, 2015.

[92] L. Wei, R. Q. Hu, Y. Qian, and G. Wu, "Key elements to enable millimeter wave communications for 5g wireless systems," *IEEE Wireless Communications*, vol. 21, no. 6, pp. 136–143, 2014.

[93] T. S. Rappaport, S. Sun, R. Mayzus, H. Zhao, Y. Azar, K. Wang, G. N. Wong, J. K. Schulz, M. Samimi, and F. Gutierrez, "Millimeter wave mobile communications for 5g cellular: It will work!," *IEEE access*, vol. 1, pp. 335–349, 2013.

[94] W. Roh, J.-Y. Seol, J. Park, B. Lee, J. Lee, Y. Kim, J. Cho, K. Cheun, and F. Aryanfar, "Millimeter-wave beamforming as an enabling technology for 5g cellular communications: Theoretical feasibility and prototype results," *IEEE communications magazine*, vol. 52, no. 2, pp. 106–113, 2014.

[95] M. Pieraccini, N. Casagli, G. Luzi, D. Tarchi, D. Mecatti, L. Noferini, and C. Atzeni, "Landslide monitoring by ground-based radar interferometry: a field test in valdarno (italy)," *International Journal of Remote Sensing*, vol. 24, no. 6, pp. 1385–1391, 2003.

[96] D. A. Wikner and G. Samples, "Polarimetric passive millimeter-wave sensing," in *Passive Millimeter-Wave Imaging Technology V*, vol. 4373, pp. 86–94, International Society for Optics and Photonics, 2001.

[97] R. T. Austin, A. J. Heymsfield, and G. L. Stephens, "Retrieval of ice cloud microphysical parameters using the cloudsat millimeter-wave radar and temperature," *Journal of Geophysical Research: Atmospheres*, vol. 114, no. D8, 2009.

[98] R. T. Austin and G. L. Stephens, "Retrieval of stratus cloud microphysical parameters using millimeter-wave radar and visible optical depth in preparation for cloudsat: 1. algorithm formulation," *Journal of Geophysical Research: Atmospheres*, vol. 106, no. D22, pp. 28233–28242, 2001.

[99] D. M. Sheen, D. L. McMakin, and T. E. Hall, "Three-dimensional millimeter-wave imaging for concealed weapon detection," *IEEE Transactions on microwave theory and techniques*, vol. 49, no. 9, pp. 1581–1592, 2001.

[100] C. Zheng, X. Yao, A. Hu, and J. Miao, "A passive millimeter-wave imager used for concealed weapon detection," *Progress In Electromagnetics Research B*, vol. 46, pp. 379–397, 2013.

[101] S. X. Z. W. J. Fa and S. M. M. K. D. Bo, "Remote sensing of water quality monitoring using an airborne imaging spectrometer," *Journal of infrared and millimeter waves*, vol. 4, p. 4, 2000.

[102] J. A. Scales and M. Batzle, "Millimeter wave spectroscopy of rocks and fluids," *Applied physics letters*, vol. 88, no. 6, p. 062906, 2006.

[103] S. Hanany, P. Ade, A. Balbi, J. Bock, J. Borrill, A. Boscaleri, P. De Bernardis, P. Ferreira, V. Hristov, A. Jaffe, *et al.*, "Maxima-1: a measurement of the cosmic microwave background anisotropy on angular scales of 10′-5," *The Astrophysical Journal Letters*, vol. 545, no. 1, p. L5, 2000.

[104] M. Fischer, D. Alsop, E. Cheng, A. Clapp, D. Cottingham, J. Gundersen, T. Koch, E. Kreysa, P. Meinhold, A. Lange, *et al.*, "A bolometric millimeter-wave system for observations of anisotropy in the cosmic microwave background radiation on medium angular scales," *The Astrophysical Journal*, vol. 388, pp. 242–252, 1992.

[105] B. Crill, P. A. Ade, D. Artusa, R. Bhatia, J. Bock, A. Boscaleri, P. Cardoni, S. Church, K. Coble, P. De Bernardis, *et al.*, "Boomerang: A balloon-borne millimeter-wave telescope and total power receiver for mapping anisotropy in the cosmic microwave background," *The Astrophysical Journal Supplement Series*, vol. 148, no. 2, p. 527, 2003.

[106] G. Denisov, V. Zapevalov, A. Litvak, and V. Myasnikov, "Megawatt gyrotrons for ecr heating and current-drive systems in controlled-fusion facilities," *Radiophysics and Quantum Electronics*, vol. 46, no. 10, pp. 757–768, 2003.

[107] T. Shimozuma, S. Kubo, Y. Yoshimura, H. Igami, H. Takahashi, Y. Takita, S. Kobayashi, S. Ito, Y. Mizuno, H. Idei, *et al.*, "Handling technology of mega-watt millimeter-waves for optimized heating of fusion plasmas," *Journal of Microwave Power and Electromagnetic Energy*, vol. 43, no. 1, pp. 60–70, 2008.

[108] T. C. Luce, "Applications of high-power millimeter waves in fusion energy research," *IEEE transactions on plasma science*, vol. 30, no. 3, pp. 734–754, 2002.

[109] J. Van Tol, L.-C. Brunel, and R. Wylde, "A quasioptical transient electron spin resonance spectrometer operating at 120 and 240 ghz," *Review of scientific instruments*, vol. 76, no. 7, p. 074101, 2005.

[110] G. Smith, J. Lesurf, R. Mitchell, and P. Riedi, "Quasi-optical cw mm-wave electron spin resonance spectrometer," *Review of scientific instruments*, vol. 69, no. 11, pp. 3924–3937, 1998.

[111] L. R. Becerra, G. J. Gerfen, R. J. Temkin, D. J. Singel, and R. G. Griffin, "Dynamic nuclear polarization with a cyclotron resonance maser at 5 t," *Physical Review Letters*, vol. 71, no. 21, p. 3561, 1993.

[112] S. Dhillon, M. Vitiello, E. Linfield, A. Davies, M. C. Hoffmann, J. Booske, C. Paoloni, M. Gensch, P. Weightman, G. Williams, *et al.*, "The 2017 terahertz science and technology roadmap," *Journal of Physics D: Applied Physics*, vol. 50, no. 4, p. 043001, 2017.

[113] J. Wang, J. Ma, Z. Shu, Z.-D. Hu, and X. Wu, "Terahertz metalens for multifocusing bidirectional arrangement in different dimensions," *IEEE Photonics Journal*, vol. 11, no. 1, pp. 1–11, 2019.

[114] Q. Yang, J. Gu, D. Wang, X. Zhang, Z. Tian, C. Ouyang, R. Singh, J. Han, and W. Zhang, "Efficient flat metasurface lens for terahertz imaging," *Opt. Express*, vol. 22, pp. 25931–25939, Oct 2014.

[115] Q. Wang, X. Zhang, Y. Xu, Z. Tian, J. Gu, W. Yue, S. Zhang, J. Han, and W. Zhang, "A broadband metasurface-based terahertz flat-lens array," *Advanced Optical Materials*, vol. 3, no. 6, pp. 779–785, 2015.

[116] R. Singh, W. Cao, I. Al-Naib, L. Cong, W. Withayachumnankul, and W. Zhang, "Ultrasensitive terahertz sensing with high-q fano resonances in metasurfaces," *Applied Physics Letters*, vol. 105, no. 17, p. 171101, 2014.

[117] L. Cong, S. Tan, R. Yahiaoui, F. Yan, W. Zhang, and R. Singh, "Experimental demonstration of ultrasensitive sensing with terahertz metamaterial absorbers: A comparison with the metasurfaces," *Applied Physics Letters*, vol. 106, no. 3, p. 031107, 2015.

[118] Y. Fan, N.-H. Shen, T. Koschny, and C. M. Soukoulis, "Tunable terahertz meta-surface with graphene cut-wires," *Acs Photonics*, vol. 2, no. 1, pp. 151–156, 2015.

[119] D. Wang, L. Zhang, Y. Gu, M. Mehmood, Y. Gong, A. Srivastava, L. Jian, T. Venkatesan, C.-W. Qiu, and M. Hong, “Switchable ultrathin quarter-wave plate in terahertz using active phase-change metasurface,” *Scientific reports*, vol. 5, p. 15020, 2015.

[120] H. Zhu, S. Cheung, X. Liu, and T. Yuk, “Design of polarization reconfigurable antenna using metasurface,” *IEEE transactions on antennas and propagation*, vol. 62, no. 6, pp. 2891–2898, 2014.

[121] H. Zhu, X. Liu, S. Cheung, and T. Yuk, “Frequency-reconfigurable antenna using metasurface,” *IEEE Transactions on Antennas and Propagation*, vol. 62, no. 1, pp. 80–85, 2014.

[122] H. L. Zhu, S. W. Cheung, and T. I. Yuk, “Mechanically pattern reconfigurable antenna using metasurface,” *IET Microwaves, Antennas & Propagation*, vol. 9, no. 12, pp. 1331–1336, 2015.

[123] P.-Y. Chen, J. Soric, Y. R. Padooru, H. M. Bernety, A. B. Yakovlev, and A. Alù, “Nanostructured graphene metasurface for tunable terahertz cloaking,” *New Journal of Physics*, vol. 15, no. 12, p. 123029, 2013.

[124] Y.-C. Song, J. Ding, C.-J. Guo, Y.-H. Ren, and J.-K. Zhang, “Ultra-broadband backscatter radar cross section reduction based on polarization-insensitive metasurface,” *IEEE Antennas and Wireless Propagation Letters*, vol. 15, pp. 329–331, 2016.

[125] B. Orazbayev, N. Mohammadi Estakhri, A. Alù, and M. Beruete, “Experimental demonstration of metasurface-based ultrathin carpet cloaks for millimeter waves,” *Advanced Optical Materials*, vol. 5, no. 1, p. 1600606, 2017.

[126] L. Liu, X. Zhang, M. Kenney, X. Su, N. Xu, C. Ouyang, Y. Shi, J. Han, W. Zhang, and S. Zhang, “Broadband metasurfaces with simultaneous control of phase and amplitude,” *Advanced Materials*, vol. 26, no. 29, pp. 5031–5036, 2014.

[127] C. Pfeiffer and A. Grbic, “Millimeter-wave transmitarrays for wavefront and polarization control,” *IEEE Transactions on Microwave Theory and Techniques*, vol. 61, no. 12, pp. 4407–4417, 2013.

[128] X. Liu, K. Fan, I. V. Shadrivov, and W. J. Padilla, “Experimental realization of a terahertz all-dielectric metasurface absorber,” *Optics express*, vol. 25, no. 1, pp. 191–201, 2017.

[129] H. Zhu, S. Cheung, K. L. Chung, and T. I. Yuk, “Linear-to-circular polarization conversion using metasurface,” *IEEE Transactions on Antennas and Propagation*, vol. 61, no. 9, pp. 4615–4623, 2013.

[130] N. W. Caira and D. R. Smith, “Multispectral metasurface hologram at millimeter wavelengths,” *Applied optics*, vol. 57, no. 1, pp. A19–A25, 2018.

[131] Z. H. Jiang, L. Kang, W. Hong, and D. H. Werner, “Highly efficient broadband multiplexed millimeter-wave vortices from metasurface-enabled transmit-arrays of subwavelength thickness,” *Physical Review Applied*, vol. 9, no. 6, p. 064009, 2018.

[132] T. Huynh and K.-F. Lee, “Single-layer single-patch wideband microstrip antenna,” *Electronics letters*, vol. 31, no. 16, pp. 1310–1312, 1995.

[133] R. Waterhouse, “Small microstrip patch antenna,” *Electronics letters*, vol. 31, no. 8, pp. 604–605, 1995.

[134] R. Lee, K. Lee, and J. Bobinchak, “Characteristics of a two-layer electromagnetically coupled rectangular patch antenna,” *Electronics letters*, vol. 23, no. 20, pp. 1070–1072, 1987.

[135] J. Burch and A. Di Falco, “Holography using curved metasurfaces,” *Photonics*, vol. 6, no. 1, 2019.

[136] C. Ge, Z. Guo, Y. Sun, F. Shen, Y. Tao, J. Zhang, R. Li, and L. Luo, “Spatial and spectral selective characteristics of the plasmonic sensing using metallic nanoslit arrays,” *Optics Communications*, vol. 359, pp. 393–398, 2016.

[137] Z. Wei, Z.-K. Zhou, Q. Li, J. Xue, A. Di Falco, Z. Yang, J. Zhou, and X. Wang, “Flexible nanowire cluster as a wearable colorimetric humidity sensor,” *small*, vol. 13, no. 27, p. 1700109, 2017.

[138] D. Kyser and N. Viswanathan, “Monte carlo simulation of spatially distributed beams in electron-beam lithography,” *Journal of Vacuum Science and Technology*, vol. 12, no. 6, pp. 1305–1308, 1975.

List of Figures

List of Tables

Acronyms and Initialisms

CCD charge coupled device. 7, 25, 59

CGH computer generated holography. 8, 9

CMOS complementary metal-oxide-semiconductor. 15

CPU central processing unit. 31, 33, 34

DC direct current. 119, 137, 138

DH digital holography. 7, 18, 30, 43

DI de-ionised. 50, 105, 139, 140

EB electron beam. 130, 131, 133, 167

EBL electron beam lithography. 48–50, 52, 54–56, 99, 104, 114, 115, 121, 122, 124, 129, 132, 133, 135–137, 159, 160, 167

EHT extra high tension. 50, 53, 114, 115, 124, 135, 136, 168

EM electromagnetic. 15, 92, 106, 124, 132, 133, 167

FFT fast Fourier transform. 19–21, 27, 30–32, 34, 57, 81, 82, 85, 90, 110, 157, 163, 164

FHMS flexible holographic metasurface. 10, 17, 40, 47, 48, 50, 51, 53–55, 57–70, 72–75, 92, 93, 104, 123, 124, 139, 140, 159–162, 164, 169

FWHM full width half maxima. 39, 40, 80, 83, 86, 88, 100, 158

GPU graphical processing unit. 31, 34

GSA Gerchberg-Saxton algorithm. 18–20, 34, 35, 40, 41, 46, 57, 65, 73, 78, 99, 108, 112, 123, 157

HLP horizontally linearly polarised. 94, 95, 102, 103, 165

HMS holographic metasurface. 9, 10, 12, 15, 17, 18, 23–25, 32, 35, 38, 40, 43, 45–47, 51, 52, 57, 76–78, 84, 87–95, 98–103, 105–107, 110–125, 128, 158, 159, 162–167

IF intermediate frequency. 102

IPA isopropyl alcohol. 48, 52, 54, 104, 114

ITO indium tin oxide. 136

LCD liquid crystal display. 8

LCP left-handed circularly polarised. 43–45, 61, 63, 69, 71, 72, 159, 161, 162

LSFM light sheet fluorescent microscopy. 17, 76–78, 80, 83, 86, 91, 123, 125

MM metamaterial. 8, 9

MS metasurface. 9, 92, 93, 164

NA numerical aperture. 11, 12, 38, 108, 157

PB Pancharatnam-Berry. 43, 45, 46, 69, 71, 74, 113, 119, 162

PML perfectly matched layer. 95

PMMA poly(methyl methacrylate). 54, 55, 95, 96, 99, 102, 104, 105, 129, 136, 165, 168

QOFR quasi-optical Faraday Rotator. 102

RAM radar absorbing material. 102

RCP right-handed circularly polarised. 43–45, 59–61, 63, 65, 69, 71, 72, 158–162

RF radio frequency. 138, 168

RIE reactive ion etch. 48, 50, 52–55, 60, 99, 104, 131, 137, 138, 159, 160, 168, 170

RS Rayleigh-Sommerfeld. 19–21, 23–25, 34, 35, 46, 78, 99, 100, 112, 123, 157, 158

SEM scanning electron microscope. 16, 50, 51, 116, 121, 122, 129, 134, 135, 137, 139, 157, 159, 166–168

SLM spatial light modulator. 8, 113, 119, 124

UV ultraviolet. 13, 15, 48, 49, 55, 56, 104, 105, 130, 132

VLP vertically linearly polarised. 94, 95, 102, 103, 165